Active Magnetic Regenerator Cycles: Impacts of Hysteresis in $MnFeP_{1-x}(As/Si)_x$

by

Premakumara Govindappa
M.Tech., Mangalore University, 2000
B.E., Bangalore University, 1997

A Dissertation Submitted in Partial Fulfillment
of the Requirements for the Degree of

DOCTOR OF PHILOSOPHY

in the Department of Mechanical Engineering

Supervisory Committee

Active Magnetic Regenerator Cycles: Impacts of Hysteresis in $MnFeP_{1-x}(As/Si)_x$

by

Premakumara Govindappa
M.Tech., Mangalore University, 2000
B.E., Bangalore University, 1997

Supervisory Committee

Prof. Andrew Rowe (Department of Mechanical Engineering)
Supervisor

Dr. Rustom Bhiladvala (Department of Mechanical Engineering)
Departmental Member

Prof. Jens Bornemann (Department of Electrical & Computer Engineering)
Outside Member

Abstract

Supervisory Committee

Prof. Andrew Rowe (Department of Mechanical Engineering)
Supervisor

Dr. Rustom Bhiladvala (Department of Mechanical Engineering)
Departmental Member

Prof. Jens Bornemann (Department of Electrical & Computer Engineering)
Outside Member

Magnetocaloric materials with first-order magnetic (FOM) phase transitions are of interest as low-cost working materials in magnetic cycles. Hysteresis is a property associated with first order transitions, and is undesirable as it can reduce performance. Devices using FOMs in active magnetic refrigeration have shown performance comparable to more expensive second-order materials, so some degree of hysteresis appears to be acceptable; however, the amount of hysteresis that may be tolerated is still an unanswered question.

Among the FOM, the family of MnP-based is one of the promising materials for magnetic heat pump applications near room temperature. The present study describes the experimental investigation of a single-layer $MnFeP_{1-x}Si_x$ active magnetic regenerator (AMR), under different test conditions and following a protocol of heating and cooling processes. The results for the FOM are compared with a Gd AMR that is experimentally tested following the same protocol, with the objective to study the irreversibilities associated with FOM. The experimental tests are performed in a PM I test apparatus at a fixed displaced volume of 5.09 cm^3 and a fixed operating frequency of 1 Hz. The results indicated a significant impact of the hysteresis on the heating and cooling temperature span for FOM regenerator. For certain operating conditions, multiple points

of equilibrium (MPE) exist for a fixed hot rejection temperature. It is shown that the existence of MPEs can affect the performance of an AMR significantly for certain operating conditions.

The present work advances our understanding since the combined hysteresis and MPE are two significant features which can impact layered AMR performance using $MnFeP_{1-x}As_x$ FOM by systematic experimental testing. With this objective, three multilayer $MnFeP_{1-x}As_x$ FOM regenerator beds are experimentally characterized under a range of applied loads and rejection temperatures. Thermal performance and the impacts of MPE are evaluated via heating and cooling experiments where the rejection (hot side) temperature is varied in a range from 283 K to 300 K. With fixed operating conditions, we find multiple points of equilibrium for steady-state spans as a function of warm rejection temperature. The results indicate a significant impact of MPE on the heating and cooling temperature span for multilayer $MnFeP_{1-x}As_x$ FOM regenerator. Unlike single material FOM tests where MPEs tend to disappear as load is increased (or span reduced), with the layered AMRs, MPEs can be significantly even with small temperature span conditions.

A third experimental study examines the performance of $MnFeP_{1-x}As_x$ multilayer active magnetic regenerators. Five different matrices are tested: (i) one with three layers; (ii) one with six layers; and (iii) three, eight layer regenerators where the layer thickness is varied. The tests are performed using a dual regenerator bespoke test apparatus based on nested Halbach permanent magnets (PM II test apparatus). Operating variables include displaced volume (3.8 - 12.65 cm^3), operating frequency (0.5 - 0.8 Hz) and hot-side rejection temperature (293-313 K).The results are mainly reported in terms of zero net load temperature span as a function of rejection temperature; a few tests with non-zero applied load are also presented. A maximum

temperature span of 32 K is found for an 8-layer regenerator, which is similar to a previous work performed with gadolinium in the same experimental apparatus.

A 1D active magnetic regenerator model accounting for thermal and magnetic hysteresis is developed and compared to experimental data for both a Gd-based and $MnFeP_{1-x}Si_x$ based AMR. Magnetic and thermal hysteresis are quantified using measured data for magnetization and specific heat under isothermal and isofield warming and cooling processes. Hysteresis effects are then incorporated in the model as irreversible work and reduced adiabatic temperature change. Model results are compared to measured temperature spans for regenerators operating with different thermal loads. Simulated results for temperature span as a function of cooling power and rejection temperature show good agreement with experimental data. The irreversible work due to hysteresis is found to have a small impact on predicted spans, indicating that useful cooling power is well predicted using cyclic measurements of adiabatic temperature change.

Table of Contents

List of Figures

List of Tables

Nomenclature

A_c	Cross-sectional area	m^2
B	Magnetic field ($\mu_o H$)	T
COP	Coefficient of performance	-
C	Specific heat	$Jkg^{-1}K^{-1}$
d_h	Hydraulic diameter	m
d_P	Particle diameter	m
f	Frequency	Hz
f_f	Friction factor	-
H	Magnetic field strength	Am^{-1}
k	Thermal conductivity	$Wm^{-1}K^{-1}$
L	Length	m
m	Magnetization	$Am^2\ kg^{-1}$
m_{irr}	Irreversible magnetization	$Am^2\ kg^{-1}$
$\dot{m}$	Mass flow rate	Kgs^{-1}
n	Number regenerators	-
Nu	Nusselt number	-
P	Pressure	Pa
Pr	Prandtl number	-
Q	Cooling power	W
Re	Reynolds number	-
S	Entropy	JK^{-1}

s	Specific entropy	$Jkg^{-1}K^{-1}$
T	Temperature	K
T_c	Curie temperature	K
t	Time	s
V	Volume	m^3
W	Work	J
x	Regenerator axial position	

Greek

ρ	Density	Kgm^{-3}
ε	Bed porosity	-
μ	Viscosity	Nsm^{-2}
μ_o	Permeability of free space	Hm^{-1}
$\mu_o H$	Magnetic field	T
τ	Period or cycle time	s
ΔTad	Adiabatic temperature change	K

Subscripts

a	Applied	-
ad	Adiabatic	-
B	Field	-
C	Cold	-
$disp$	Displaced	-

eff	Effective	-
f	Fluid or final	-
gen	Generation	-
H	Hot	-
i	Initial	-
irr	Irreversible	-
j	Temporal step index	-
mag	Magnetic	-
neg	Negative	-
pos	Positive	-
r	Regenerator material	-
ref	Refrigeration	-
S	Solid	-
tr	Transition	-

Guruvandana

I consider myself an extremely fortunate student of **Prof. Andrew Rowe.** His unstinted support, motivation & immaculate guidance enabled me to overcome all the impediments during my research work. I would like to place my profound gratitude & respectful salutations to him for introducing me to the fascinating area of magnetic refrigeration technology & imbibing in me a sense of utmost self-confidence & academic discipline. His unrestrained trail of original ideas & sustained encouragement in all research work pursuits was all highly refreshing & stimulating experience, which will be cherished by me throughout my life.

Acknowledgements

First and foremost, I would like to express my profound gratitude to my supervisor **Prof. Andrew Rowe**, Department of Mechanical Engineering for his constant guidance and support for the duration of my doctoral research and for facilitating all the requirements for research problems. His constant push helped me to remain focused. His immense knowledge and aspiration has been of great value which in-turn made me look up to him and aspire me to become an independent researcher.

I am grateful to **Prof. Jens Bornemann**, Department of Electrical & Computer Engineering, and **Dr. Rustom Bhiladvala**, Department of Mechanical Engineering, for contributing their time, and shaping my work leading to this thesis.

I would like to thank with immense pleasure and deep sense of gratification to **Dr.P.V.Trevizoli,** for all his advice and encouragement.

I wish to place in record my sincere gratitude to **Mrs.SusanWalton**, Administrator, IESVic, University of Victoria, for her priceless suggestions, encouragement and timely help in all respects.

My genuine gratitude to **Mr. Manjunatha Prasad,** I.A.S., Government of Karnataka., for his kindness, immense and immeasurable support which he has bestowed upon me. I am highly indebted to him, for being my Teacher and Philosopher.

I would like to thank my colleagues **Prof. K.V. Sharma, Prof. H.N. Vidyasagar** and **Prof. D.K. Ramesh,** Department of Mechanical Engineering, UVCE, Bangalore., for their patience and un-conditional support without which I would never have derived the joy and satisfaction .

I would also express my deep appreciation to **Mr.Oliver Campbell, Dr.Iman Niknia, Mr.Theodor Christiaanse, Dr. Reed Teyber, Dr. Armando Tura,** and **Mr.Yifeng Liu** of Cryofuels Laboratory for their constant and selfless support at every stage of my research work.

I owe my heartfelt special thanks to **Dr. Venkatesh T. Lamani, Mr. Suhas Prahalad, Mr.Kiran Kumar, Dr. Manjunath** and **Mrs. Shilpa B.S** for their support.

I am thankful for my friends **Dr. Nagendrappa. H, Dr. Randhir Singh, Dr. Ilam Parithi, Mr.Ramesh. Mr.Virag, Dr. Sumasushan Thomas, Mr.Yogesh and Mrs.Akshara** for their friendly behavior and constant support; they were alongside me to look into all my needs.

I am grateful for financial assistance from the Government of India for the duration of my Ph.D, particularly **Mr. Lingichetty** and **Mrs. Abha Goshain**, the consulates of Indian Consulate Vancouver, British Columbia, Canada.

I thank my parents **Shri. Govindappa. H, Smt. Savitramma**, my in-laws **Shri. Mahalingam Smt. Mahadevi**, my brother **Mr. K. G. Sathish**, and my brother-in-law **Mr. C. Govindappa** and **Mr. C.M. Shravan** for their un-conditional love and blessings. Your sincere prayers and invaluable trust in me, has been a source of great encouragement.

I am extremely thankful to my beloved wife **Dr. Komal** for all her support and motivation. I can forthrightly say that it was only her emotional and moral support that ultimately pushed me through this journey. I am grateful to God for having you by my side forever. I am blessed with my daughter **Bhaveesha Prem** and I thank her for her love, patience, and understanding and allowed me to spend most of the time on this thesis. I thank God for enlightening my life with your presence.

Dedication

I would like to dedicate this thesis to my parents **Smt.Savithramma, Shri.Govindappa.H,** my in-laws **Smt. Mahadevi, Shri. Mahalingam,** and my family.

Chapter 1 Introduction

1.1 Overview

The rising interest in efficient refrigeration technologies is based on the fact that air conditioning and refrigeration account for at least 15% of the energy consumed in residential and commercial buildings [1]. More importantly, developing countries are increasing demand and, according to recent estimates, an additional 1.6 billion air conditioning units worldwide are expected by 2050 [2].

Of late, environmental impact has become an issue of paramount importance in the design and development of refrigeration systems. Most near room-temperature refrigeration or cooling technologies are based on the conventional vapor compressor technology as seen in Fig. 1 (a). Vapor refrigerant is circulated through the cycle in which it alternately condenses and evaporates, thus undergoing a change of phase from vapor to liquid and again liquid to vapor.

(a) (b)

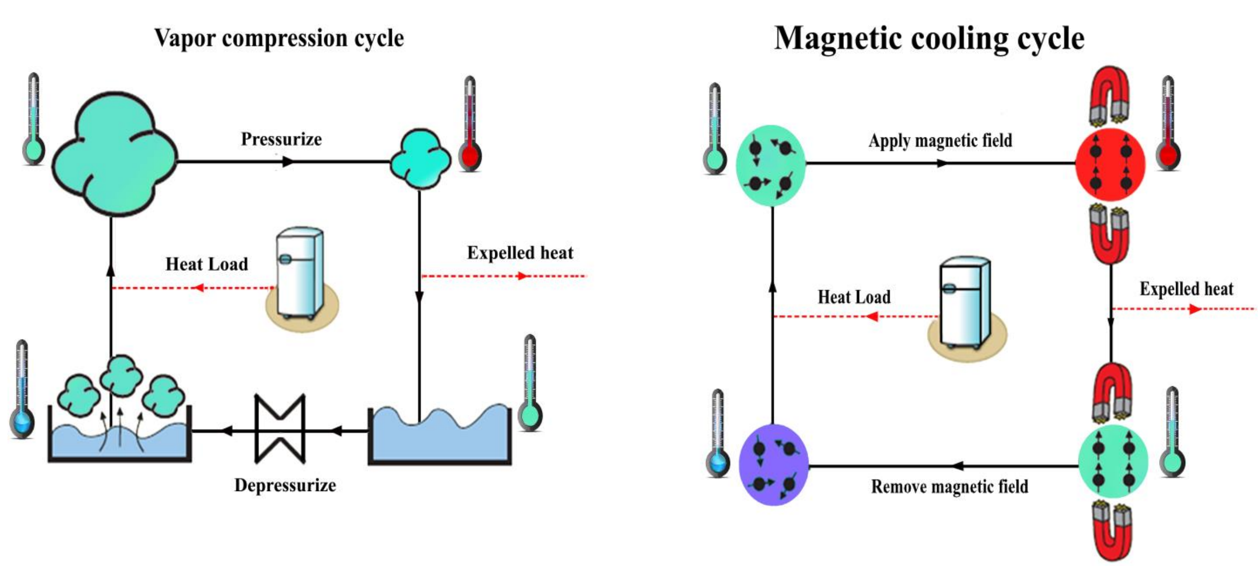

Fig. 1 Cooling cycles. (a) The Conventional vapor compression cycle and (b) Magnetic cooling cycle. Adapted from Ichiro Takeuchi and Karl Sandeman [14].

During evaporation it absorbs the latent heat from the refrigerated space and subsequently rejects heat to surroundings while condensing. Refrigerants such as CFC (chlorofluorocarbons), HCFC (hydro chlorofluorocarbons) and HFC (hydrofluorocarbons) can lead to ozone layer depletion and global warming. Due to the negative impact on the environment, refrigeration systems are subject to prescriptive regulation. The Montreal and Kyoto international regulations have motivated the use of new refrigeration technologies and new products.

In recent years, magnetic refrigeration has shown potential as an energy efficient, environmentally safe cooling solution. Magnetic cycles, as seen in Fig. 1 (b), are based on the *magnetocaloric effect* (MCE) which causes magnetocaloric materials to heat up when exposed to an increased magnetic field and to cool down when the magnetic field is decreased or removed. A simple magnetic cycle is analogous to vapour compression (Fig. 1 (a)) where adiabatic compression and expansion are replaced by magnetization and demagnetization. An *active magnetic regenerator* (AMR) cycle is commonly used to create magnetic refrigerators and heat pumps. An AMR is a porous structure of magnetocaloric material, through which a heat transfer fluid is oscillated while applied magnetic field is cycled. In the AMR cycle, the magnetocaloric materials act as a refrigerant and as a thermal regenerator to establish a temperature gradient along its length.

Magnetic refrigeration has a number of advantages compared to compressor-based refrigeration: there are no harmful gasses involved, they may be built more compactly because the main working material is a solid, and magnetic refrigerators can have low noise and vibration. The cooling efficiency of magnetic refrigeration systems can reach up to 60% of the theoretical limit, in comparison to their best gas compression refrigerators counterparts wherein the best efficiencies are 45% [3-8].

Magnetocaloric cooling for near room-temperature refrigeration and heat pump applications has attracted significant research attentions globally since 1976. The future of magnetic refrigeration technology is promising albeit there are a number of challenges to be solved [9-13]. The research described in this thesis focuses on a problem found in some magnetocaloric materials *hysteresis*. Hysteresis is a desirable property in hard magnets used to generate external magnetic fields; however, hysteresis is a detrimental phenomenon for a magnetic refrigerant which should be "soft". The following sections provide an overview of magnetocaloric materials and systems.

1.2 Background

Magnetic cooling has a long history. In 1926 Debye and in 1927 Giauque predicted the theoretical possibility of adiabatic demagnetization cooling [15-16]. In 1933, Giauque and MacDougall succeeded in magnetic cooling from 4.2 K to the temperature range from 3.5 to 0.5 K. Since then adiabatic demagnetization has played an important role in the field of low temperature physics [16]. In 1976, Brown showed that a continuously operating device working near room-temperature could achieve useful temperature spans. Brown's reciprocating magnetic refrigerator used one mole of 1 mm thick Gadolinium (Gd) plates separated by a wire screen and a 7 T magnetic field supplied by a water-cooled electromagnet and obtained a temperature span of 47 K [9].

Following this early work of Brown, the concept of the AMR was introduced by Barclay and Steyert in the early 1980s [17-18]. In the late 1990s, two major advances occurred. The first one was the discovery of the so-called giant MCE in $Gd_5(Si_2Ge_2)$ [19]. The second advance concerns the development of a prototype demonstrating the feasibility of the magnetic refrigeration near room-temperature [3]. These two advances using magnetic fields in the range of permanent magnets increased interest and activity in magnetic refrigeration near room temperature.

When a magnetic material is subjected to a sufficiently high magnetic field, the magnetic moments of the atoms become reoriented. The temperature of the material increases, as the magnetic field is applied adiabatically and then the temperature decreases when the magnetic field is eventually removed. During the application and removal of external magnetic field, the *heating* and *cooling* that takes place is known as the *magnetocaloric effect* (MCE). In the year 1917, Weiss and Picard first experimentally observed the MCE [3]. MCE depends on the material, temperature and strength of magnetic field. Two thermodynamic parameters used to characterize material performance are magnetic entropy change, ΔS_{mag}, and adiabatic temperature change, ΔT_{ad}. Conventionally, both ΔS_{mag} and ΔT_{ad} changes are determined as the change resulting from zero field to an arbitrary applied field. The entropy change dictates the amount of energy that can be transferred to the material magnetically and therefore the maximum amount of cooling power the material can produce. The ΔT_{ad} provides the temperature difference between the solid and fluid that drives heat transfer and regeneration. The maximum MCE (ΔT_{ad}) is observed near the Curie temperature, the temperature where the transition in magnetic order changes spontaneously. An example of ΔT_{ad} for Gadolinium and a $MnFeP_{1-x}As_x$ alloy for a field variation from 0-1.1 T is given in Fig. 2. The plot on the left shows the magnitude of ΔT_{ad} as a function of temperature where the plot on the right shows a representation of the state change in the entropy–temperature space.

(a) (b)

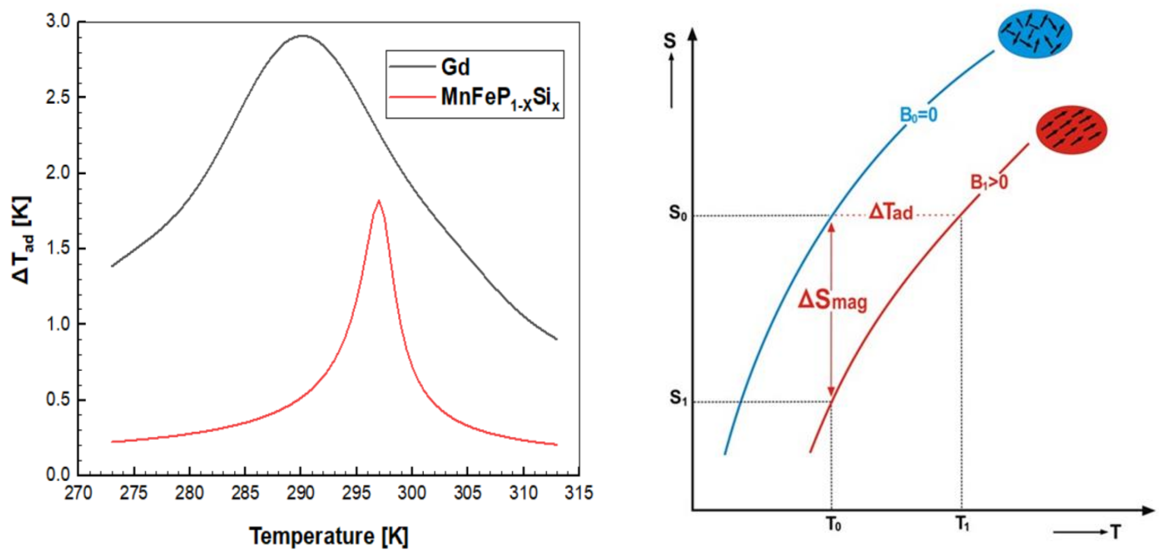

Fig. 2 Gd and $MnFeP_{1-x}Si_x$ properties: (a) Direct measured adiabatic temperature change as a function of the temperature, for a magnetic field variation of 1.1 T; (b) a schematic representation of adiabatic temperature change and magnetic entropy change in the entropy-temperature state space.

Thermodynamics

Magnetocaloric materials are the substances capable of work interactions, which are defined by the formula,

$$\delta w = B_a dm \tag{1}$$

where B_a is the applied magnetic field ($B_a = \mu_o H_a$, in the bore of a solenoid in free space expressed in Tesla and m is the magnetization per unit mass (Am^2kg^{-1}). Magnetic field and magnetization are vectors, and the work δw is determined by the dot product. The assumptions involved here include the net magnetization and the applied field being parallel to each other, and absence of hysteresis. The magnetization is a function of the local magnetic field, *H*, and temperature, *T*. The magnetization is found by solving Maxwell's equation for flux conservation since the local field is determined by the applied field, H_a, state equation for the material m (*T*, *H*), and the macroscopic geometry. Maxwell's equation for flux conservation is given by

$$\nabla \cdot B = 0 \tag{2}$$

where $B = \mu_o(H + M)$. The local field can be described in terms of the applied field and a demagnetizing field H_d,

$$H = H_a + H_d \tag{3}$$

The behaviour of materials that have expansion and magnetic work modes is described by temperature, magnetic field, and pressure. Materials which experience structural and magnetic phase transitions can show significant field induced entropy changes and first-order phase transitions (a discontinuous variation in entropy). The thermodynamics of a simple magnetic system are described here.

The mass specific entropy of a simple magnetic material is written as a function of temperature and local magnetic field, $B = \mu_o H$ and the variation in entropy is given by,

$$ds = \left(\frac{\partial s}{\partial T}\right)_B dT + \left(\frac{\partial s}{\partial B}\right)_T dB \tag{4}$$

The equivalence of partial derivatives and Gibb's potential show,

$$\left(\frac{\partial s}{\partial B}\right)_T = \left(\frac{\partial m}{\partial T}\right)_B \tag{5}$$

Using the definition of specific heat at constant field,

$$c_B = T\left(\frac{\partial s}{\partial T}\right)_B \tag{6}$$

The variation in entropy can be written in terms of intensive properties,

$$ds = \frac{c_B}{T} dT + \left(\frac{\partial m}{\partial T}\right)_B dB \tag{7}$$

From Equation (7), the temperature change induced by change in field for an isentropic process, can be determined by the temperature dependence of magnetization,

$$\Delta T(T_i, B_i, B_f) = -\int_{B_i}^{B_f} \frac{T}{C_B}\left(\frac{\partial m}{\partial T}\right)_B dB \tag{8}$$

The MCE depends upon the initial temperature, initial and final magnetic fields. The magnetic entropy change for an isothermal process is determined by the temperature dependence of magnetization,

$$\Delta s(T, B_i, B_f) = \int_{B_i}^{B_f} \left(\frac{\partial m}{\partial T}\right)_B dB \tag{9}$$

Experimentally, magnetization or specific heat can be measured as a function of field and temperature which may lead to uncertainties arising from experimental error and numerical differentiation as result of sudden variations in magnetization. Specific heat measurements in-field can be used to determine MCE and entropy change via,

$$s(T, B) = \int_0^{\tau} \frac{C_B(T,B)}{T} dT \tag{10}$$

$$\Delta s(T, B_i, B_f) = \int_0^{\tau} \frac{C_B(T,B_f) - C_B(T,B_i)}{T}\, dT \tag{11}$$

1.3 AMR Cycle

AMRs provide an alternative to standard gas and fluid cycles for reversibly transforming work into heat transfer [20, 21]. The AMR is a porous structure, similar to a common thermal regenerator, built using *magnetocaloric material* (MCM). The term ‘active’ in active magnetic regenerator refers to the matrix being comprised of MCM which is undergoing magnetic work transfer. The heat transfer performance and the pressure drop greatly depend on the geometry of the AMR. AMR matrices can be packed particle bed, such as spheres [22-25] parallel plate regenerator [26, 27], or other geometrics such pins as seen in Fig. 3. The packed bed configuration has good heat transfer characteristics due to high surface area per unit volume. The AMR beds are designed to withstand mechanical stresses and cyclic loads due to magnetization and demagnetization, and oscillating flow.

Previously, we have shown in Fig. 2 (a), the ΔT_{ad} for the benchmark material Gd in a magnetic field ranging from 0 – 1.1 T. Because ΔT_{ad} is small, an AMR cycle is needed for the magnetic refrigeration device to produce a larger temperature span.

(a) (b)

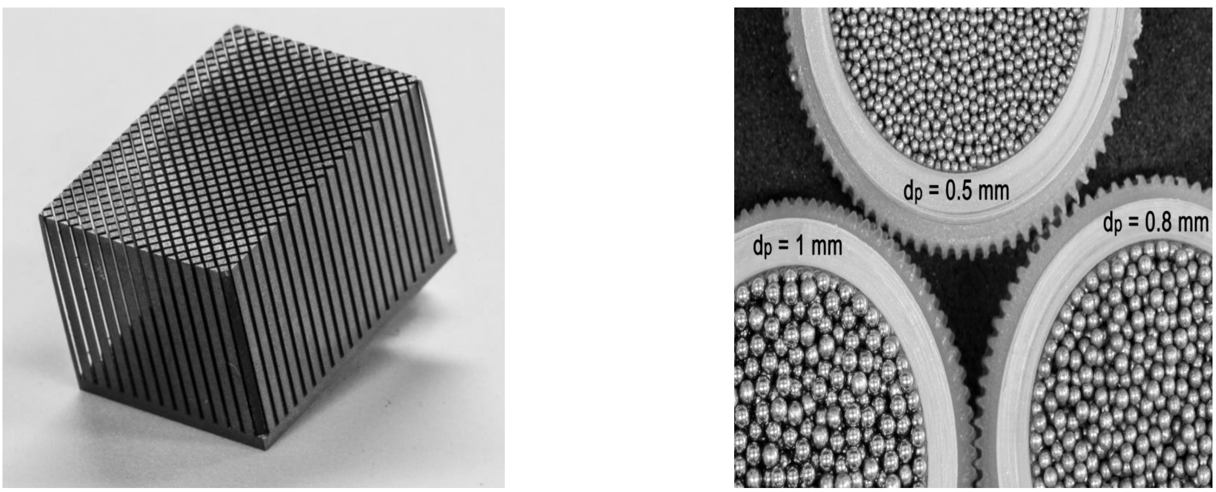

Fig. 3 (a) Pin array and (b) Packed sphere regenerator matrices [27].

In 1982, Barclay and Steyert introduced the concept of AMR cycle, which is basically the thermodynamic cycle used in AMR refrigeration devices [17 –18]. An AMR cycle consists of four approximately independent thermodynamic processes as shown in Fig. 4, and Fig. 5 shows an arbitrary section of the regenerator in a T-S diagram. The idealized processes of the AMR cycle are:

1. Adiabatic magnetization (process *a*-*b*): The increasing magnetic field on the magnetocaloric material increases the temperature of MCM.

2. Cold Blow (process *b-c*): The fluid displaces from the cold side to the hot side and thus absorbs heat along the regenerator bed. The absorbed heat is rejected to the surrounding through a hot heat exchanger.

3. Adiabatic demagnetization (process *c-d*): here the MCM temperature decreases adiabatically as the magnetic field is removed, which is a consequence of MCE.

4. Hot Blow (process *d-a*): The fluid displaces from the hot side to the cold side and thus absorbs heat from the cold heat exchanger.

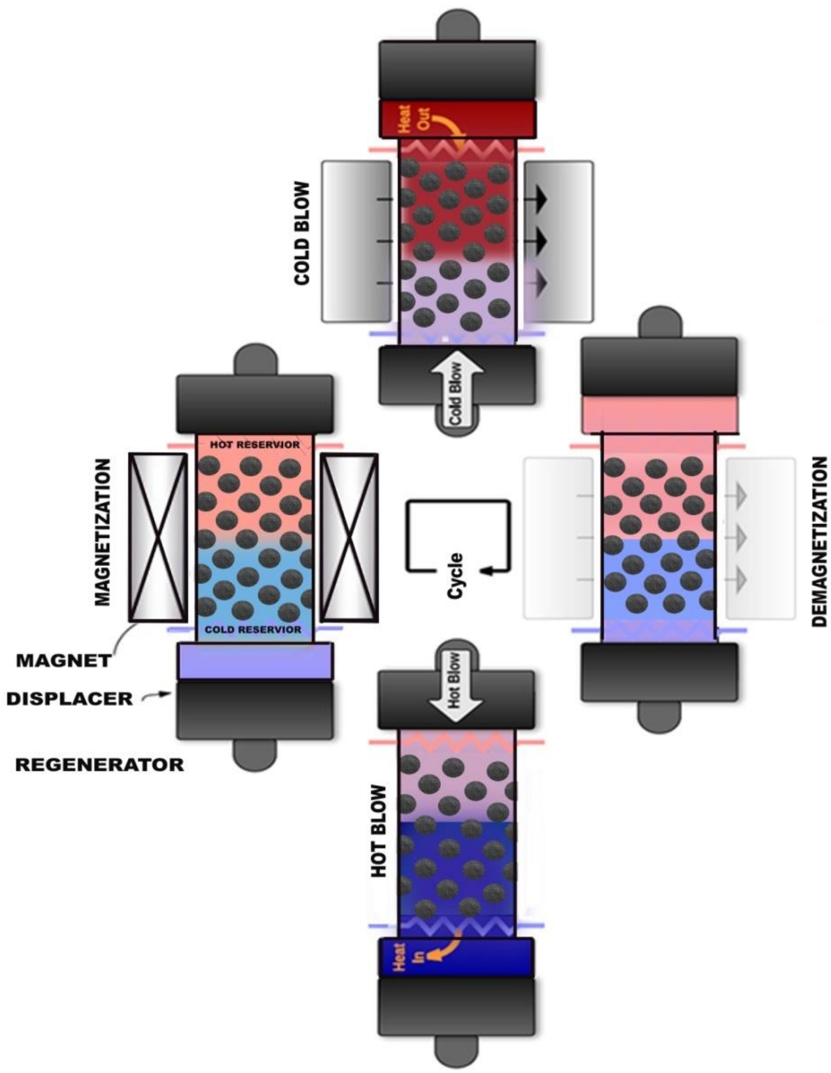

Fig. 4 Schematic representation of AMR cycle consists of four processes. Adapted from P.V.Trevizoli [27].

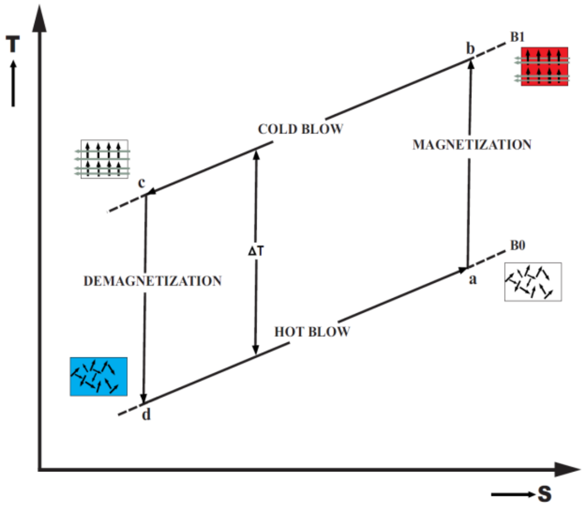

Fig. 5 Schematic T-S diagram of AMR cycle.

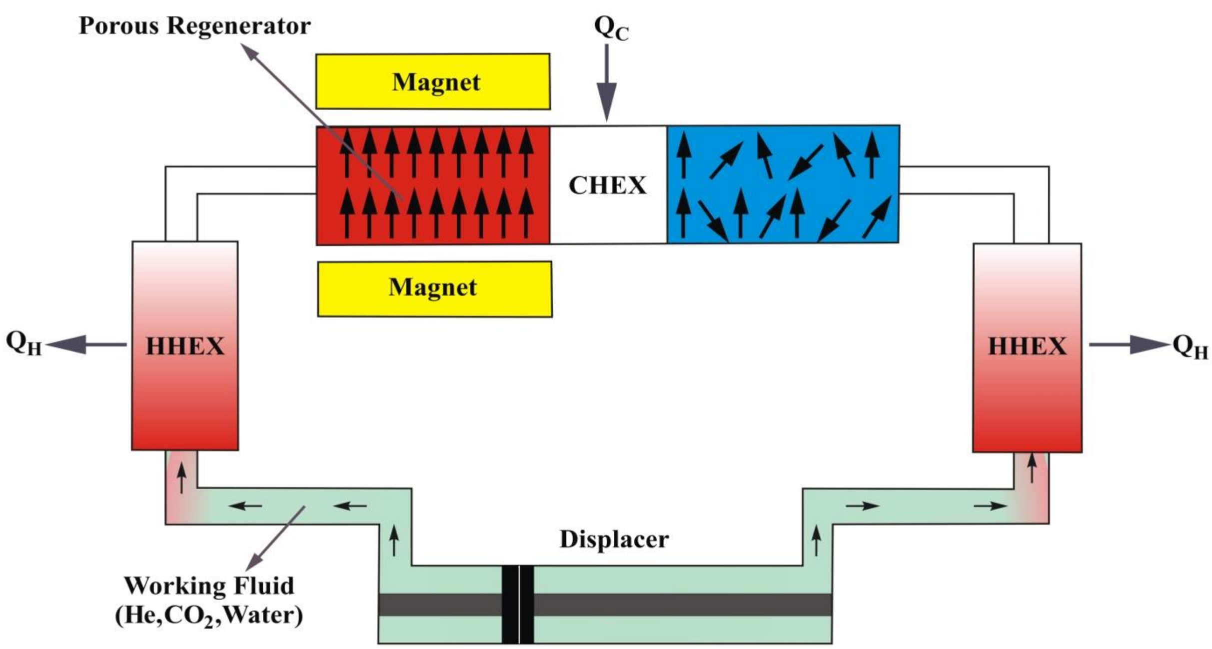

Fig. 6 Systematic representation of an AMR device.

The schematic of an AMR device is shown Fig. 6. In an AMR cycle, the MCM acts as a refrigerant and as a heat regenerator to establish a temperature gradient along its length [10,21]. The movement of heat transfer fluid is controlled by a displacer and exchanges heat with the AMR. The regenerator works between two thermal reservoirs and maintains a temperature span between them by pumping heat from one reservoir to another. This is the basis of the AMR cycle. During the magnetization process, there is an increase in temperature of the magnetocaloric material due to the magnetocaloric effect. The working fluid enters the voids of the porous material after leaving the cold heat exchanger (CHEX), when subjected to a magnetic field. The fluid is heated when it passes through the porous structure of the magnetocaloric material. After leaving the porous matrix the fluid enters a hot heat exchanger (HHEX) where heat is rejected to the ambient. This fluid enters the porous magnetocaloric material in the counter-flow direction and is not subjected to the magnetic field. After cooling, the fluid exits the porous magnetocaloric material structure and enters the CHEX.

1.4 Magnetocaloric Materials

Magnetocaloric materials (MCM) are broadly classified into two groups: *first order* and *second order* materials [28]. First order magnetic (FOM) materials transition from a disordered magnetic state to an ordered state near the transition temperature (or Curie temperature) with a discontinuous variation in entropy due to latent heat. Second order magnetic (SOM) materials change from an ordered magnetic state to a disordered state in a continuous manner. A stylized representation of a FOM is give in Fig. 7, showing entropy as a function of temperature in zero magnetic field and with a local field strength of $B = \mu_0 H$.

In Fig. 7, isothermal entropy change and ΔT_{ad} are shown for two different temperatures, T_1 and T_{tr}. The transition temperature, T_{tr}, may be determined from magnetization or specific heat measurements and corresponds to the point separating the ordered and disordered states. As can be seen, the transition point varies with field strength and for many materials with FOM, this is a linear effect. The entropy change ΔS and ΔT_{ad} for second order materials are similarly defined; however, SOM's tend to show a less abrupt variation in entropy. The thermodynamic description of the FOM ordering process is complicated by the fact that material behavior is determined by composition as well as processing path and, in practice, FOM materials can show a range of behavior between that of an ideal first-order transition and a second order transition.

First order phase transition is characterized by the discontinuous change in magnetization near transition temperature. An example FOM, $MnFeP_{1-x}As_x$ is presented in Fig. 8 (a) by black markers, although difficult to see, the $MnFeP_{1-x}As_x$ material shows a hysteresis which means the *heating* and *cooling* transformation does not occur at the same temperature.

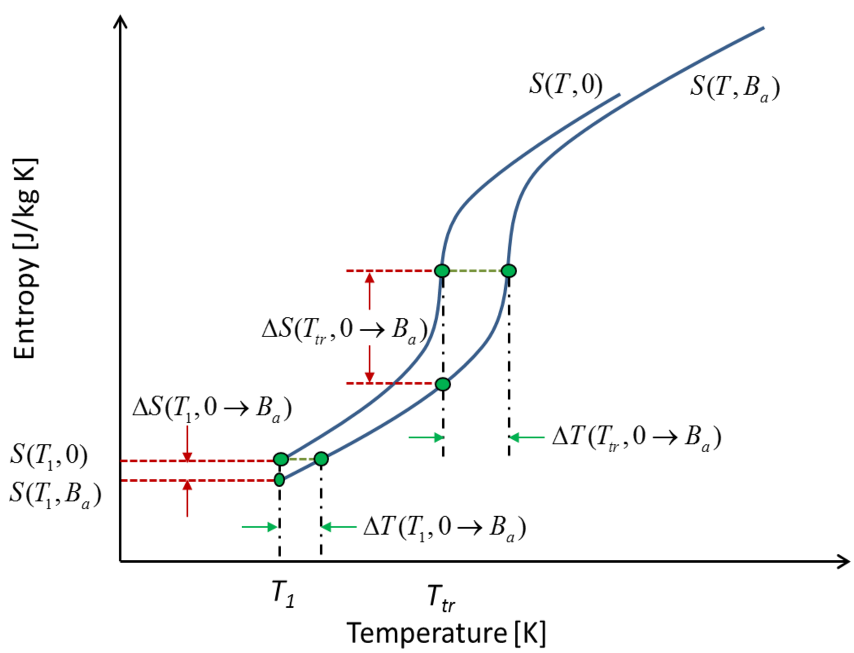

Fig. 7 Entropy variation with field and temperature for a FOM. Isothermal entropy change and adiabatic temperature change depend upon temperature and the magnitude of the change in applied magnetic field, $B_a = \mu_0 H_a$. Maximum values are found near the transition temperature, T_{tr}.

Fig. 8(b) compares the magnetic entropy change for the Gd and two FOM $Gd_5Ge_2Si_2$, $MnFeP_{1-x}As_x$ materials for 2 T and 5 T magnetic fields. With the increase in magnetic field in Gd (SOM) material, the magnetic entropy change increases and presents a broad operating temperature range. In the $Gd_5Ge_2Si_2$ and $MnFeP_{1-x}As_x$ FOM materials the magnetic entropy change only increases to a certain value of magnetic field. However, with a larger field the magnetic entropy change will be significant over a wider temperature range.

(a) (b)

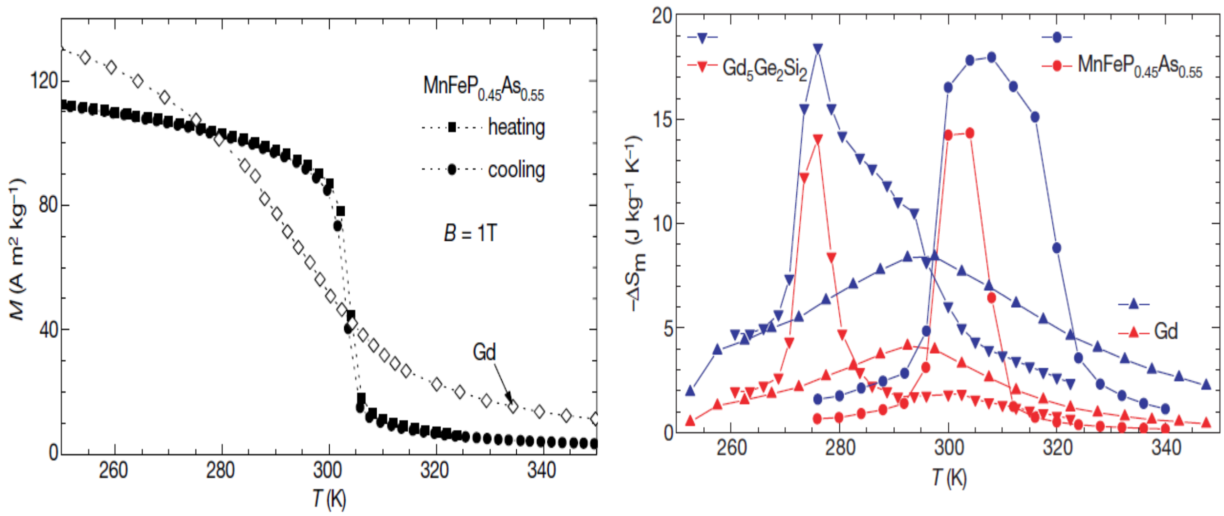

Fig. 8 SOM and FOM properties: (a) Magnetization as a function of the temperature, for a magnetic field variation of 1 T [29]; (b) Magnetic entropy change as a function of the temperature at magnetic field change of 0 to 2 T and 0 to 5 T [29].

For the $MnFeP_{1-x}As_x$ alloy, Gd has a larger ΔT_{ad} over a broader temperature range. Another important difference between FOM and SOM is the specific heat. The FOM material presents a considerably larger specific heat capacity than the Gd [30]. In FOM materials, the temperature where the peak specific heat is found changes with applied magnetic fields [12].

1.4.1 Intensity of the MCE and operating temperature range

One of the most important criteria for the selection of an MCM is its intensity of MCE. As the MCE of a MCM is characterized by the ΔT_{ad} or by the ΔS, it is important to understand the relationship between these two quantities. A detailed analysis of the impact of the ΔT_{ad} and the ΔS on the AMR's performance is presented in [31]. For a MCMs with a high ΔS but a low ΔT_{ad}, the heat transfer from the matrix to the fluid will be slow, limiting the operation frequency [12]. With a smaller ΔS, but greater ΔT_{ad}, the heat-transfer between the material and the medium of heat-transfer is improved, but cooling potential decreases [32].

It is advantageous for the MCM to have a ΔT_{ad} over as wide a temperature range as possible. This is especially important in an AMR where the temperature span is established over the material. Gd (SOM) exhibits a ΔT_{ad} over a wide temperature range and therefore is more tolerant to varying operational conditions as shown in Fig. 9. $MnFeP_{1-x}As_x$ FOMs exhibit a ΔT_{ad} over a narrow temperature range, therefore less flexibility to varying operating conditions. As shown in Fig. 9, the ΔT_{ad} peak of $MnFeP_{1-x}As_x$ FOMs are sharp and narrow, and therefore a single material is not adequate to achieve a large temperature span across the regenerator. To overcome this problem, layering of materials with cascading transition temperature is used to maximize the MCE in the regenerators over a desired operating temperature range. Layering has been demonstrated in SOMs [33-35] and FOMTs [30,36-38].

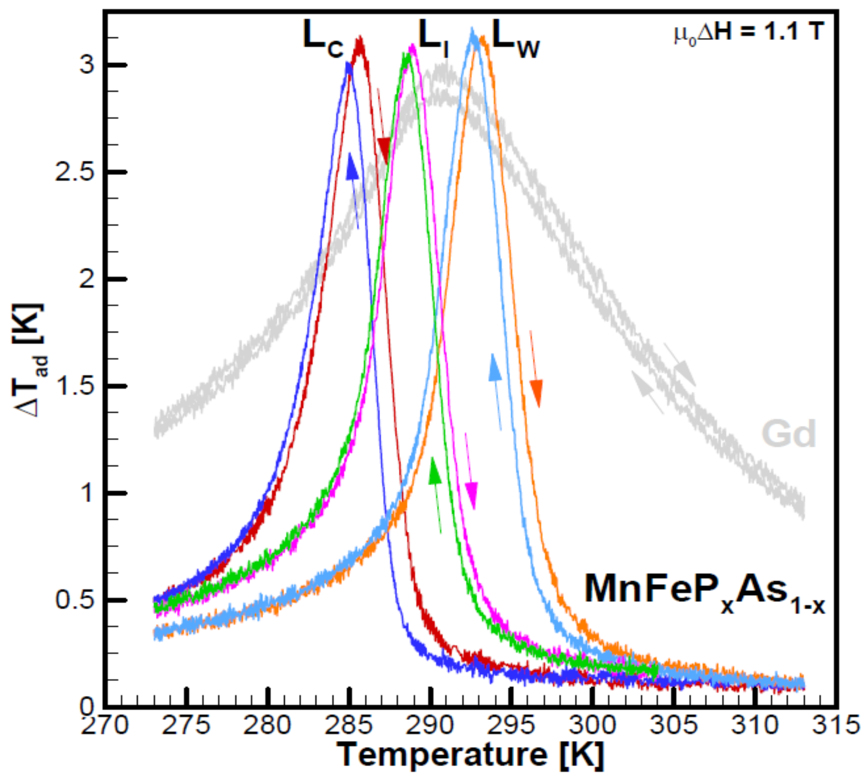

Fig. 9 Adiabatic temperature change as a function of temperature for Gd and $MnFeP_{1-x}As_x$. Directly measured ΔT_{ad} data for the magnetic field changes from 0 to 1.1 T, and warming (red) and cooling (blue) measurements are shown. $MnFeP_{1-x}As_x$ material case where the intermediate layer (L_I), cold layer (L_C), and warm layer (L_W).

1.4.2 Suitable Curie temperature of the material

The maximum ΔT_{ad} is observed near the Curie or transition temperature, and the *Curie temperature* (T_{Curie}) is unique for any given SOM and FOM material. Additional ways of defining T_{Curie} include the peak temperatures of the ΔT_{ad}, ΔS, and specific heat which may also vary as a function of magnetic field [39-41]. Another issue related to FOMs is the difficulty controlling the T_{tr} of each layer so that the desired property distribution is achieved when manufacturing a multilayer AMR. Fig. 9 suggests that the FOM material AMR performance can be improved by layering regenerators with spatially varying T_{Curie} (or T_{tr}). The effects of T_{Curie} spacing between two SOM materials have been studied by Teyber et al [42]. However, if the T_{Curie} are spaced apart too far for the two material regenerator design, it can perform worse than a single material regenerator as demonstrated by Engelbrecht et al [43]. Lei *et al* [44] performed a numerical investigation on the sensitivity of the layer transition temperature, number of layers and how random variations on the transition temperature affect the AMR performance.

1.5 Common MCM with a near room temperature MCE

The room temperature reference for SOM is Gd which has been extensively tested in different AMR devices [23,24,25,45,46,47]. More recently, due to potential cost and performance benefits, several FOM families are of interest as solid state refrigerants [4,12,48,49]. However, only a subset have been processed as a regenerative matrix and experimentally tested.

1.5.1 Gadolinium

The performance of single and multilayer AMR composed of SOMs, especially Gd and Gd-based alloys, have been reported over the past 15 years [10,21,50]. Gd has a phase transition near room-temperature and hence was a prime candidate to be considered for room temperature refrigeration by Brown (1976) [9]. The Curie temperature depends on purity and homogeneity, and in single crystals the T_{Curie} is 294 K [51-53]. The experimental values of ΔT_{ad} for polycrystalline Gd at the T_{Curie} 292 K when magnetized from 0 – 1 T, 0 – 3 T, 0 – 5 T, and 0 – 7 T were approximately 3.6 K, 7.8 K, 11 K and 13.8 K, respectively [54]. Studies show that the maximum values of the ΔT_{ad} will occur at a higher magnetic field change. Dan’kov et al concluded that magnetic hysteresis present by the single Gd crystals is low [52]. Due to its ductility, Gd can be shaped into thin plates and foils [9,55]. Fujieda et al reported that the thermal conductivity of Gd at room temperature is approximately 10 W/m-K [56]; however, the heat capacity of Gd is significantly lower compared to that of FOM materials [30]. There is also a possibility of Gd getting corroded at room-temperature due to the presence of water in heat transfer fluid, which in turn may affect the long-term performance and durability of an AMR device. The corrosion problem can be overcome by adding a corrosion inhibitor in the heat transfer fluid. Despite the favorable characteristics Gd can offer, due to its high cost (Gd belongs to heavy rare-earths that are significantly less abundant compared to e.g. La and MnAs [5]), it is not attractive for applications.

1.5.2 Mn-based MCMs

Among the FOMs, the family of MnP-based materials are considered one of the more promising because of tunable transition temperature [57,58], low costs [5], and large peak magentocaloric properties [29]. Although these characteristics are desirable, the sharp peak of the adiabatic temperature change, the strong dependence of the specific heat on temperature and magnetic field [12], and hysteresis [28,59,60], are characteristics which may restrict their use as solid state refrigerants.

In the past fifteen years a number of other alloys with a first-order phase transition and a pronounced MCE were discovered and described. From the magnetocaloric point of view, currently the most promising are the alloys based on MnAsSb, MnFe(P,As), MnFe(P,Si), La(Fe,Mn,Si)H and LaFeSi(Co,H) [64-70]. Of these, the first three systems are classified as part of the $(Mn,Fe)_2(P,X)$ family. Some of the relevant parameters of the various material systems used in near room-temperature AMR cycles are summarized in Table 1.

This thesis focuses on the family of first order manganese-iron-phosphorous-arsenic $MnFeP_{1-x}As_x$ and $MnFeP_{1-x}Si_x$ FOMs. A favorable point of this family of compounds is the adjustability of its T_{Curie}, which can be achieved by varying the chemical composition (Mn/Fe or P/As ratio)

Table 1 Comparison of different potential magnetocaloric materials for a field change of 2 T. Gd is included as reference material

Material	Operating Range [K]	ΔS (2 T) [$Jkg^{-1}K^{-1}$]	ΔB (2 T) [K]	T_c [K]	Costs [$/kg]	Density 10^3 [kgm^{-3}]	Reference
Gd	270-310	5	5.8^d	293	20	7.9	[61]
$Gd_5Ge_2Si_2$	150-290	27	6.6^d	272	60	7.5	[62,63]
La(Fe,Si) H	180-320	19	7^c	300	8	7.1	[64]
MnAs	220-320	32	4.1^d	287	10	6.8	[65,66]
MnNiGa	310-350	15	2^c	317	10	8.2	[67]
MnFe(P,As)	150-450	32	6^d	292	7	7.3	[68]
MnFe(P,Si)	210-430	12(1.5T)	2.45^d(1.5T)	284		5.3	[69]
MnFe(P,Si,B)	160-360	10(1T)	2.5^d(1T)	281			[70]

d means direct measurement, *c* is calculated from a combination of measurements.

[71,72]. In 2002, the giant-MCE (GMCE) was reported for this class of material [29]. The transition temperature is tunable between 200 K to 350 K by changing the As/P ratio without losing the large MCE. Although thermal hysteresis is present, it is relatively small (less than 2 K). Recently, the related $MnFeP_{1-x}Si_x$ compounds were reported to show large magnetocaloric effects; however, they also have hysteresis [73]. It was later reported that with varying Mn:Fe and P:Si ratios, giant magnetocaloric effects and reduced thermal hysteresis can be achieved [74].

1.6 Hysteresis of the MCE

Magnetocaloric first order materials have a coupled magnetic and structural transition, giving rise to both magnetic and thermal hysteresis in magnetization and heat capacity. Magnetic hysteresis is observed during isothermal magnetization and demagnetization and thermal hysteresis is associated with cycling of temperature at constant applied field. FOMs have varying degrees of magnetic and thermal hysteresis which are dependent on the MCM family and composition. Provenzano et al [75] argued that the hysteresis frequently associated with the FOM can reduce the usefulness of a material in a refrigeration cycle. Recent works demonstrate how hysteresis reduces the useful ΔT_{ad} and how it impacts the AMR performance [28,59,76,77,78,79].

Magnetization and specific heat are measured while holding field or temperature constant and varying the other parameter. For example, a specific heat measurement may start with a sample at a low temperature and constant applied field. The temperature of the sample is then increased using a measured heat input. This is known as a *warming* or *heating* process. The reverse would be a *cooling* process whereby the sample begins at a high temperature and is then cooled using a measured heat removal. This data is then used to determine the isofield specific heat for each process. An adiabatic temperature change experiment may be performed under similar protocols (i.e. *heating* and *cooling* process). Hysteresis is present when the measured data for heating and *cooling* processes are found to be different.

The hysteresis phenomena have been studied experimentally and numerically. Basso et al. [80,81] describe a theoretical thermodynamic model of hysteresis and evaluate the impact on a simple cycle. They show that irreversibility of materials acts as a source of losses. Kitanovski and Egolf [82] examine hysteresis losses as a scalar quantity expressing a degradation of the efficiency of a cycle. Engelbrecht et al. [76] carried out experimental property measurements and showed that hysteresis in $MnFeP_{1-x}As_x$ compounds may significantly reduce their performance in a practical AMR. The authors also argue that a detailed hysteresis model is either overly complex or computationally prohibitive, and then, proposed a simplified method to model $MnFeP_{1-x}As_x$ compounds including some hysteresis effects to build material property functions. Brey et al.

[77] presented a thermodynamic model of AMR systems with magnetic hysteresis. Their approach treats the magnetic hysteresis phenomenon as a form of internal entropy generation. The authors concluded that as regenerator volume increases, hysteretic losses outweigh the capacity gains associated with adding more refrigerant. L.von moss et al. [59] presented experimental results of an AMR operating with MnFe(P,As) FOM alloy with 1.6 K hysteresis. They observed that the operating hot side temperature where peak of the temperature span is observed shifts about 1.1 K when performing heating and cooling tests, but no reduction on the performance was observed.

1.7 Layered AMRs

Magnetic refrigerants based on tuneable, first-order phase transitions offer cost-effective pathways to increasing the temperature span, cooling power, and efficiency of active magnetic regenerators. Unlike many second-order alloys, the magnetocaloric response tends to be over a narrower temperature range requiring the use of more materials so as to operate over a desired temperature range. Some of these limitations may be overcome by layering the AMR [18,33,47]. Engelbrecht et al. [43] compared the performance of a single and two-layer $La(Fe,Co,Si)_{13}$ FOM. The authors found that the two-layer bed with transitions temperatures of 286 K and 289 K outperformed the single layer AMR; however, this result did not hold when the transition temperatures were 276 K and 289 K. Tusek et al. [30] compared two, four and seven layers $La(Fe,Co,Si)_{13}$ FOM and found that the four layer AMR presented the best performance. In addition, in both studies, Engelbrecht et al. [43] and Tusek et al. [30], the authors reported that the multilayer FOM AMR underperformed the Gd single layer regenerator in terms of temperature spans. Jacobs et al. [36] reported maximum cooling capacities for 2.5 kW and temperature spans of 11 K for a five-layer $La(Fe,Co,Si)_{13}$ AMR. These results demonstrate that multilayer AMR performance is sensitive to the layer transition temperatures and number of layers.

As introduced earlier, an issue related to FOMs is difficulty controlling the transition temperature of each layer so that the desired property distribution is achieved. Lei et al. [44] performed a numerical investigation on the sensitivity of the layer transition temperature, number of layers and how random variations on the transition temperature affect the AMR performance. In that work, La $(Fe,Mn,Si)_{13}H_y$ FOM is considered. The authors reported that the nominal cooling capacity increases with the number of layers and that 10 to 15 FOM layers may be suitable to achieve a 30 K temperature span for a 1.2 T magnetic field change. In another work Lei et. al. [83] numerically investigated multi-layer AMRs with first and second-order (SOM) materials. The authors found that the FOM could provide higher specific cooling powers than SOM, but several layers are necessary to achieve a target performance. They also proposed that mixing FOM and SOM could reduce the number of layers in an AMR and reduce the sensitivity of the AMR to temperature fluctuations, which reduce the FOM-based AMR performance.

1.8 Summary

This chapter describes a general overview of vapor compression and magnetic refrigeration technologies. The fundamentals of thermodynamics and the phenomenon of MCE are briefly discussed. The thermodynamic cycle for magnetic refrigeration, the AMR is elaborated on. Classification of the MCMs in terms of the desired characteristics are discussed. Furthermore, the applications of different MCMs at room temperature (Gd and its alloys, and Mn – based MCMs) are discussed. Layered AMR performance is sensitive to the layer transition temperature and number of layers. The nature of these MCMs with respect to their properties, as well as the hysteresis behavior in FOM materials are compared. The following chapter defines some key challenges with FOMs in AMRs and defines the scope of the thesis.

Chapter 2 Objectives and research methodology

2.1 Problem description

Over forty-one magnetic refrigerator prototypes have been reported for near-room temperature operation [13]. The majority of these prototypes use Gd as the MCM in the form of particles. Even though Gd is a good refrigerant, performance of most devices is insufficient, and materials with similar or better MCE properties at lower cost are needed. Although some FOMs have desirable characteristics such as a high MCE, large specific heat and use inexpensive constitutes, they also have some drawbacks such as irreversibility associated with thermal and magnetic hysteresis, and a strong dependency on temperature and magnetic field, resulting in a narrow temperature range where the MCE is useful [76,81]. However, FOM properties suggest that they may be suitable as less expensive replacements for rare-earth alloys.

In contrast to FOMs, Gd does not present significant hysteresis and the ΔT_{ad} is high over a broad range of temperature. The hysteresis frequently associated with the FOMs can reduce the usefulness of a material in a refrigeration cycle [75]; however, the impact of hysteresis in an actual device performance remains largely unexplored. In addition the MCMs available from the $MnFeP_{1-x}(As/Si)_x$ have not been proven to outperform SOMs in layered AMRs. There is a need for detailed experimental validation of $MnFeP_{1-x}(As/Si)_x$ to determine potential as an efficient and inexpensive working material in AMR systems.

The narrow operating range of a single alloy is overcome by using a number of alloys with varying transition temperature in an AMR. However, an issue related to FOMs is difficulty in controlling the transition temperature of each alloy so that the desired property distribution is achieved when manufacturing a multilayer AMR.

There has been significant development towards addressing the challenges of the layering materials in an AMR. Numerical studies have been published on layering of SOM's [84-90], FOM's [44] and a combination of FOM's and SOM's [77,83,91,92]. Experimental studies are published on layering SOM's [8,33,35,42,47,93-98], FOM's [36,99-102] and comparing SOM and FOM layered regenerators [30,34,43,103-106]. Majority of these studies use Lanthanum based alloys as an example of a FOM [30,34,36,43,99-106]. These results demonstrate that multilayer AMR performance is sensitive to the layer transition temperatures and number of layers. Multilayer AMRs made of inexpensive materials from the $MnFeP_{1-x}Si_x$ and $MnFeP_{1-x}As_x$ are relatively unexplored in AMR experiment. The development of efficient layered AMRs capable of operating over temperature spans exceeding 30 K is one of the challenges in creating a practical device.

Numerical models of refrigeration systems are paramount in understanding the interplay between the different elements. Currently there is little validation of numerical models that can accurately predict the effects of hysteresis on the performance of an AMR. Theoretical and experimental studies of the hysteresis effects are needed, not only for device development, but also to understand the physical mechanisms behind the magnetic and thermodynamic properties of the materials. This should be done by systematic performance studies on hysteretic materials in actual devices and, also, by developing and validating active magnetic regenerator models to include hysteresis.

From the presented literature review, it can be concluded that the impact of hysteresis in the performance of AMRs remain largely unexplored. Due to the complexity of such phenomena, this should be carried out by systematic experimental tests and by developing and validating numerical methods to model the magnetic and thermal hysteresis in AMRs.

2.2 Objectives

The objective of the research described in this thesis is to assess the performance of FOM materials from the $MnFeP_{1-x}(As/Si_x)$ family and to determine the impacts of thermal hysteresis in AMR cycles. Some of the key questions addressed are:

- How does hysteresis impact the use of multiple materials in an AMR?
- How are temperature span and cooling power impacted by magnitude of hysteresis?
- Are materials with large entropy change, ΔT_{ad} and hysteresis more effective than materials with low entropy change, ΔT_{ad} and hysteresis?
- How does $MnFeP_{1-x}(As/Si_x)$ multilayer AMR improve the performance?
- What are the effects of varying the thickness of each layer of this multilayer AMR?
- How should material properties be implemented in AMR models?

To address these questions, the performance of alloys from the $MnFeP_{1-x}(As/Si_x)$ system are analyzed using modeling and experimental characterization. Models are developed to provide ΔT_{ad} and specific heat for FOM materials. This information is used in a model of an AMR cycle, and the sensitivity of cooling power, temperature span, and work input are determined. Experiments using Gd and FOM regenerators are performed to validate the model. Layered regenerators made up of materials with different levels of hysteresis are tested and simulated. Together, these results are used to improve our understanding of the potential of first order $(Mn,Fe)_2(P,X)$ for use in AMR cycles. In addition, a better understanding of hysteresis impacts in general is developed.

2.3 Methods

Research objectives are met using experimental and numerical methods.

2.3.1 Experimental

Experimental characterization in AMR cycles is performed using two permanent magnet test devices (PM I and PM II). Both devices are similar in structure as are the waveforms for flow and field. The main difference is that PM II allows for larger amounts of material to be tested than PM I. PM I tends to have better waveform control and lower heat leaks than PM II. Experiments using Gd are also performed to provide reference data in the same devices. Materials with varying hysteresis, transition temperatures, and operating conditions are tested using a range of layered geometries.

- First, tests using regenerators composed of Gd and a single alloy of $MnFeP_{1-x}Si_x$ FOM are performed using similar amounts of material, but at different rejection temperatures. Hysteresis in measured temperature span is examined using two different processes: a *heating* process, where the rejection temperature is increased after steady-state is reached and a *cooling* process using the reverse protocol.
- In a second study, layering of FOM materials in an AMR is studied using three different regenerators of equal volume. Alloys from the $MnFeP_{1-x}As_x$ family are used in a two-layer matrix and two different three-layer configurations where the intermediate layer is varied while the warm and cold layers remain the same. One three-layer composition uses MCE material with a lower ΔT_{ad}; in the second three-layer AMR, the intermediate layer uses MCE material with a higher ΔT_{ad}. The experimental tests are performed in the PM I test apparatus at different operating conditions.
- In a third experimental study, five different multilayer beds using $MnFeP_{1-X}As_X$ are tested: (i) one with 3-layers; (ii) one with 6-layers; and (iii) three, 8-layer regenerators. In the 8-layer cases, the material composition remains the same (i.e., same transition

temperatures) but the layer thickness is altered such that regenerator mass varies for the same targeted operating span. The distribution of layer thickness in all regenerators is constant. The experiments are performed in the PM II test device under several different operating conditions.

2.3.2 Modeling

A 1D mathematical model, in which the energy balance equations for solid and fluid phases are solved, is used to assess impacts of thermal and magnetic hysteresis. The model is validated with experimental data for a Gd-based AMR and later compared with experimental data for $MnFeP_{1-x}Si_x$-based AMR. To better understand hysteresis effects and the implementation of material data in numerical models, different scenarios for properties are simulated.

2.4 Outline of the thesis

The research comprising this thesis is described in seven chapters. The following Chapters 3 and 4 describe the experimental devices and numerical model used in the research. Chapters 5 and 6 discuss the experimental and modeling results, respectively. Chapter 7 summarizes the work, key findings, and provides recommendations for future study.

Chapter 3 Experimental test device and procedures

In this chapter, the devices used in underlying experimental investigations are discussed. Two AMR refrigerator test apparatuses designed and developed at UVic are used to produce extensive experimental data. Data from both machines are used in this study, and hence both their specifications, operational ranges and experimental operational procedures are described.

3.1 PM I device

The experimental tests are performed using the test apparatus known as PM I at the University of Victoria [25]. A photograph of PM I is shown in Fig. 10(a) and i.e schematic representation is shown Fig. 10(b). This device uses two rotary nested permanent magnet Halbach arrays to generate a time-varying magnetic field, changing from 0.13 to 1.4 T.

(a)

(b)

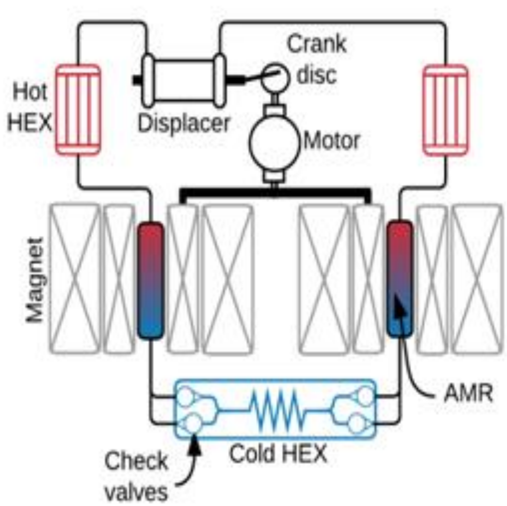

Fig. 10 (a) Photograph of PM I and (b) Schematic diagram of PM I.

The AMR bed is placed in the bore of each magnet, hence, a continuous cycle is verified. An electrical motor rotates the magnets synchronized with a crank disc that moves the displacer back and forth. Then, as the magnets spin, fluid is continuously pumped from the cold to the hot heat exchanger of the magnetized bed, and from hot to the cold heat exchanger of the demagnetized bed. The HHEX has its temperature controlled by a thermal bath, while the CHEX imposes a thermal load via an electrical heater. Check vales are used in the CHEX to guarantee unidirectional flow. Also, the entire cold side of the apparatus is thermally insulated to reduce heat leaks to the ambient. A list of the operarting parameters and test conditions used in PM I are listed in Table 2.

3.1.1 Procedure for thermal hysteresis measurements

The tests conditions (frequency and displaced volume) vary depending on which regenerator is being tested. Pressure drop is the limiting constraint and impacts maximum frequency and displaced volume. The rejection temperature (T_H) is varied in a range from 284 to 312 K. All the beds are tested for different applied-load conditions to characterize the maximum temperature span for a given set of operating conditions.

Pairs of regenerators are characterized by measuring the temperature span generated under various operating conditions. Data points are characterized by three parameters; hot side (rejection) temperature, T_H, displaced volume, V_d, and device frequency f. T_H is varied (283 to 313 K) to characterize the performance sensitivity to the heat rejection temperature.

Characterizing an AMR includes measurements for *heating* and *cooling* experiments with repeatability tests. In AMR testing, *heating* means starting a load test at a rejection temperature below the peak specific heat of the coldest material in the cascade. A temperature span data point is collected, and then the heat rejection temperature is increased. The system is allowed to come to steady-state and the next data-point is collected. A *cooling* protocol is the reverse of the above, i.e. start with the temperatures throughout the regenerator higher than the active region of the warmest layer in the cascade. The procedure for hysteresis testing is summarized below.

Heating Curve Procedure:

1. Set the hot side temperature to approximately 5 degrees below the Curie temperature of the coldest layer.
2. Allow cold side temperature to decrease as low as possible. This may take up to 2-3 hours.
3. Increase the warm side temperature to be the same as the cold side – begin the experiment.
    a. once the system has reached steady state, take a data point,
    b. increase the hot side temperature by 3-5 degrees using the chiller,
    c. once steady state has been reached, take data point
4. Continue step 3 until the hot side temperature is at least 3-5 degrees hotter than the peak temperature for the warmest layer.

Cooling Curve Procedure:

1. Set hot side temperature to approximately 10 degrees hotter than the layer with the warmest Curie temperature.
2. Apply a heat load to bring the cold side up to the same temperature as the hot side
3. Once the hot and cold side are at the same temperature turn off the heat load or reduce the heat load to the testing load.
4. Once at steady state, take a data point.

5. Reduce the hot side temperature by 2-5 degrees using the chiller and take data point once steady state is reached.
6. Repeat step 5 until the hot side temperature is below the coldest Curie temperature.

Note: the device is run continuously for the entire test procedure (8-12 hours)

Cyclic steady-state is assumed to be reached once the maximum temperature difference across each regenerator is constant to within 0.1 K for a specified time. When at steady-state, 800 samples are collected at 20 Hz. These points are used to determine the steady-state, time-averaged fluid temperature at the hot and cold side of each regenerator. The temperature differences across the two regenerators are averaged to attain the temperature span performance metric for the experimental parameters set (T_H, V_d and f). This is done over a range of heat rejection temperatures and net applied heat loads.

3.2 PM II device

Experiments are performed using a custom test apparatus (PM II) built at the University of Victoria [22]. A photograph of PM II is shown in Fig. 11(a) and a schematic representation is shown in Fig. 11(b). This device uses two nested permanent magnet Halbach arrays to generate a time-varying magnetic field. The minimum field is 0.06 and the peak field is 1.45 T; however, due to the waveform, the flow-average low field during a blow period is 0.4 T and the flow-average high field is 1.35 T [107]. A regenerator is located in the bore of each magnet so that a total of two beds are used (Regenerator 1 and 2). A motor rotates the magnets and a synchronized crank disk oscillates a displacer pump. The HHEX temperature is set using an external water-glycol circulator while a thermal load is applied to the CHEX via an electric heater. Check valves are used to guarantee unidirectional flow in the heat exchangers.

(a) (b)

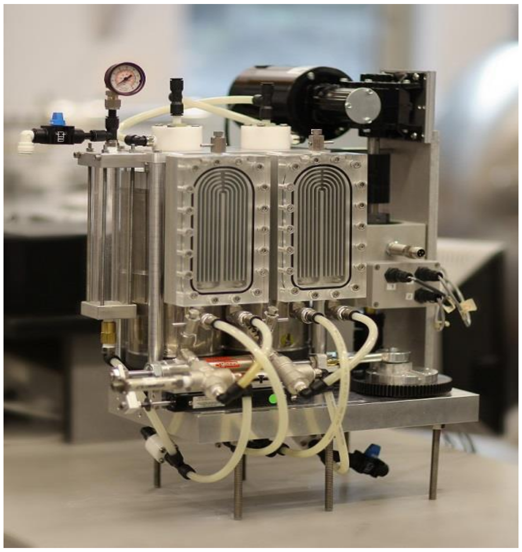

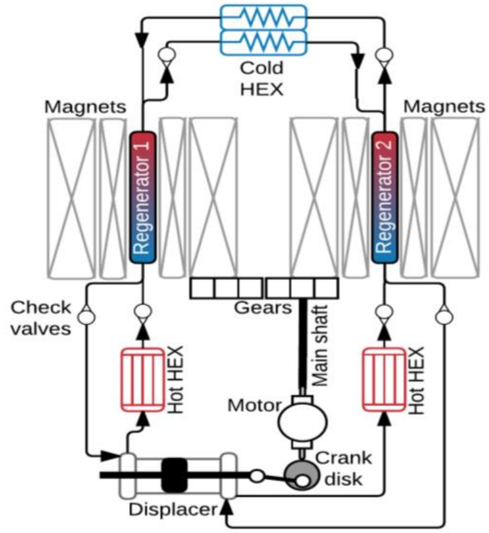

Fig. 11 (a) Photograph of PM II and (b) Schematic diagram of PM II.

The temperature span is the average difference in fluid temperatures measured by thermocouples at the hot and cold end of each regenerator. Pressure transducers are located at the displacer ports. The heat transfer fluid used is a mixture of water and ethylene glycol in a volume fraction of 80/20%. A list of the operarting parameters and test conditions used in PM II are listed in Table 2.

Table 2 Summarizes of the specifications of the PM I and PM II

Properties	PM I	PM II
Heat transfer fluid	Water–glycol (80-20%)	Water–glycol (80-20%)
Displaced fluid volume range, V_d(cm^3)	2.5 – 10.0	2.5 – 10.0
Heat rejection temperature, T_h (°C)	0–45	0–45
Regenerator Volume range, V_r (cm^3)	5.5 – 22.0	14.0 – 57.0
Machine Frequency, f (Hz)	0.5- 4.0	0.5 – 4.0
Peak magnetic field (T)	1.47	1.54

3.2.1 Characterization procedure

Regenerator pairs are characterized by the no-load temperature span that PM II generates under various operating conditions. Data points are characterized by three device parameters; hot side temperature, T_H, displaced volume, V_d, and device frequency, f. The hot side of the device is maintained at a constant temperature using a temperature controlled chiller while the cold side temperature develops over time due to the AMR cycle. The displaced volume is set by adjusting the stroke of a reciprocating fluid displacer. The operating frequency of the device is set by adjusting the voltage supplied to the drive motor. Frequency is limited by the pressure rating of the fluid displacer. The device was run as fast as possible while maintaining a peak pressure below 100 psi. Pressure drop is also taken into consideration because larger pressure drops can lead to faster regenerator degradation and breakdown. Thermocouples are positioned at the hot and cold end of each regenerator. Cyclic steady-state is assumed to be reached once the maximum temperature difference across each regenerator has not been surpassed for 120 seconds. When at steady-state, 800 samples are collected at 20 Hz. These points are used to determine the steady state, time averaged fluid temperature at the hot and cold side of each regenerator. The temperature differences across the two regenerators are averaged to attain the temperature span performance metric for the experimental parameters set (T_H, V_d and f).

3.3 Regenerator

The regenerator beds in the present work are made of SOM and FOMs in a single and multilayer configuration. The AMR matrix is composed by the MCM assembled inside a housing (G10 fiberglass tube).The regenerator matrices are made of irregular particulate with different diameter (μm) ranges. The particulate is coated with a layer of proprietary epoxy creating a monolithic porous structure; the epoxy content is ~ 2 %wt. A sealed cylindrical flow path is created by bonding the monolithic structure inside a G10 tube. The regenerator house in PM I is made of G10 fiberglass tube, with 16 mm inside diameter (ID) and 19 mm outside diameter (OD). All tubes used in PM II have a 22.2 mm inside diameter (ID) and 24.2 mm outside diameter (OD). The regenerator length, mass, layer thickness and porosity of beds tested in PM I and PM II in this work are summarized in Chapter 5. Fig. 12 shows the picture of a sample regenerator ready to be tested.

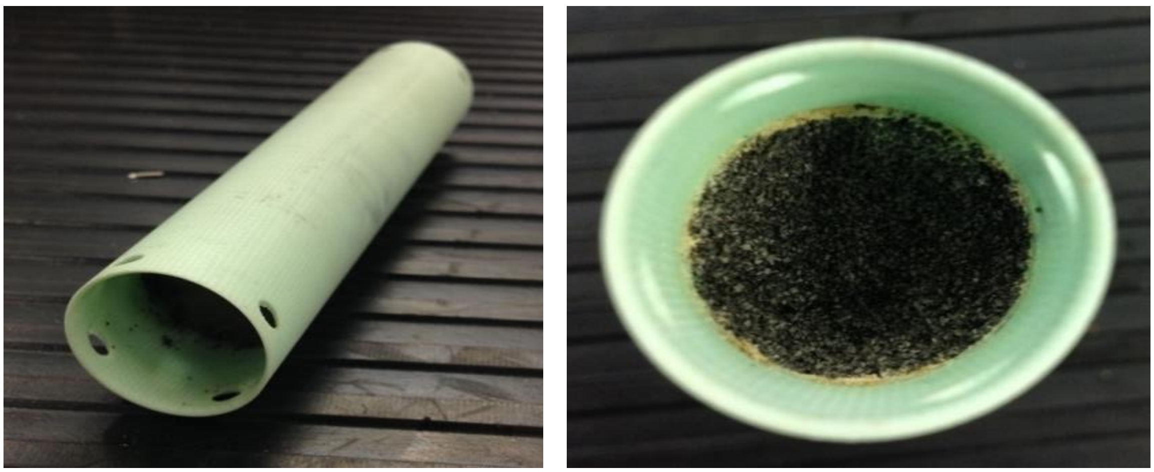

Fig. 12 Picture of a sample regenerator ready to be tested.

3.4 Summary

In this chapter, the PM I and PM II devices used and their respective procedures for the experimental tests were presented. The AMR construction method was discussed. The following chapter describes the numerical model of an AMR.

Chapter 4 Numerical model development

A mathematical model based on the one-dimensional (1D) energy balance equations for porous media [108], which the MCE is implemented using a built-in scheme [109] is developed and implemented. The heat transfer and losses (demagnetization and heat leaks) model follows [107,109-111], while the hysteretic model follows the references [59,79] for thermal and [77] for magnetic hysteresis. The model is validated with no-load and load experimental data for a Gd-based AMR and later compared with experimental data for $MnFeP_{1-x}Si_x$ based AMR. To better understand the hysteresis effects, different scenarios are simulated, and the results indicated a significant impact of the hysteresis on the AMR performance.

4.1 Mathematical model and numeric implementation

The AMR is modeled using a 1D approximation to determine temperature as a function of space and time for the solid matrix and fluid. The energy balance equations for the solid and fluid phases are presented in Eq. 12 and 13 [108]. The solid phase equation includes the MCE [109,110] and the magnetic hysteresis as described in Ref. [77]. Fig. 13 provides a schematic diagram of the 1-D AMR model with input parameters which defines the regenerator geometry, magnetic regenerator material, the heat transfer fluid and the applied magnetic field.

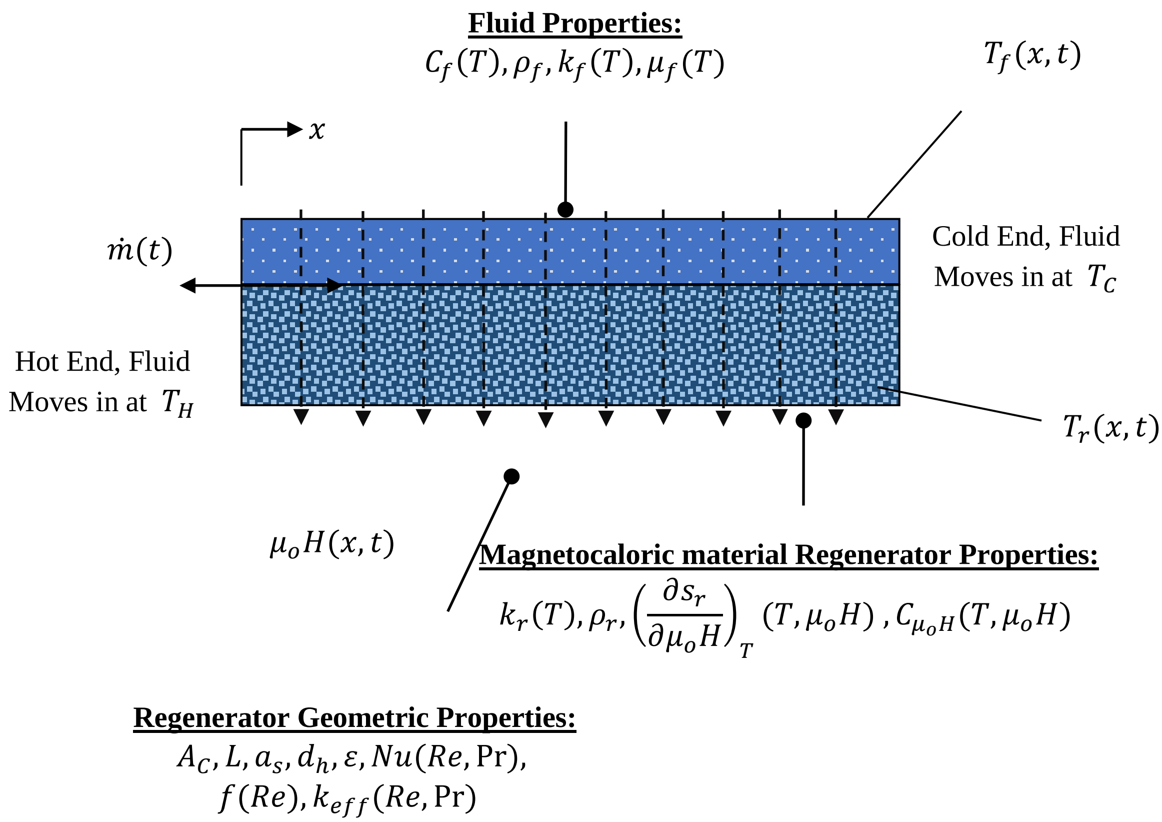

Fig. 13 Schematic diagram of 1-D AMR model with input parameters for both the fluid and the regenerator.

The heat transfer fluid properties considered in the model are fluid specific heat capacity (C_f), density (ρ_f) of the fluid, thermal conductivity of the fluid (k_f), viscosity of the fluid (μ_f), hot fluid reservoir temperature (T_H) and cold fluid reservoir temperature (T_C). Mass flow of the heat transfer fluid as a function of time ($\dot{m}$), which should be based on the profile of applied magnetic field ($\mu_o H$) specified in terms of space (x) and time (t). The regenerator MCM properties used in the model include, the regenerator material thermal conductivity (k_r), partial derivative of entropy with applied field at constant temperature conditions $\left(\frac{\partial s_r}{\partial \mu_o H}\right)_T$, constant field specific heat capacity ($C_{\mu_o H}$), and the density (ρ_r). The packed sphere bed matrix geometry consists of small passages that allow the thermal contact between the fluid and the regenerator material. The geometry is characterized by the cross sectional area (A_C), bed length (L), specific particle surface area (a_s), particle hydraulic diameter (d_h) and bed porosity (ε). For a packed bed geometry the Nusselt number (Nu) depends on the Reynolds number and Prandtl number of the flow, i.e. Nu = f (Re_f, Pr_f). Also, a friction factor (f_f) has to be considered based on the regenerator geometry and the Reynolds number of the flow. The effective thermal conductivity (k_{eff}) of the regenerator matrix depends on the thermal conductivity of the fluid and the magneto caloric material, the regenerator geometry, the Reynolds number of the fluid flow, and the Prandtl number of the fluid flow.

$$\frac{Nu \cdot k_f}{d_h} a_s A_s \left(T_f - T_r\right) + k_{eff} A_c \frac{\partial^2 T_r}{\partial x^2} = \rho_r A_c (1-\varepsilon) \cdot \left[C_{\mu_o H} \frac{\partial T_r}{\partial t} + T_r \left(\left. \frac{\partial s_r}{\partial \mu_o H} \right|_T \cdot \frac{\partial \mu_o H}{\partial t} - \frac{\dot{S}_{gen}}{m} \right) \right] \tag{12}$$

$$k_{disp} A_c \frac{\partial^2 T_f}{\partial x^2} - \dot{m} C_f \frac{\partial T_f}{\partial x} - \frac{Nu \cdot k_f}{d_h} a_s A_c \left(T_f - T_r\right) + \left| \frac{f_f \dot{m}^3}{2 d_h {\rho_f}^2 {A_c}^2} \right| = \rho_f A_c \varepsilon C_f \frac{\partial T_f}{\partial t} \tag{13}$$

In Eq. (12) the terms from left to right represent: interstitial heat transfer between the regenerator material and the fluid, axial conduction, energy storage, reversible entropy variation (MCE) and irreversible entropy production, $\dot{S}_{gen}$, that accounts the magnetic hysteresis [77]. In Eq. (13) the terms are, respectively, axial conduction, enthalpy flux, and interstitial heat transfer between the regenerator material and the fluid, viscous dissipation and the stored energy due to heat capacity of the fluid. Pumping losses are determined by the friction factor (f_f), using the correlation in Ref. [108, 112]. The effective thermal conductivity for the fluid, including thermal dispersion (k_{disp}) uses the closure relations in Ref. [113], while the static thermal conductivity for the solid phases (k_{eff}) uses the correlation in Ref. [114]. The Nusselt number is calculated using the correlation proposed by Wakao and Kaguei [115].

The last term from Eq.12 is the rate of entropy production per unit mass $\frac{\dot{S}_{gen}}{m}$ defined as a function of the irreversible magnetization (m_{irr}) and it is assumed to be related to the area enclosed by the magnetization when applying and removing the magnetic field, at a fixed temperature.

Entropy generation per unit mass is therefore is given by [77]:

$$\dot{S}_{gen} = \frac{m_{irr}(T, \mu_o H)}{T}\left|\frac{d\mu_o H}{dt}\right| \tag{14}$$

Where, $v = {}^{1}/_{\rho}$

Substituting Eq. (14) in Eq. (12) yields,

$$\frac{Nu \cdot k_f}{d_h} a_s A_s (T_f - T_r) + k_{eff} A_c \frac{\partial^2 T_r}{\partial x^2} = \rho_r A_c (1-\varepsilon) \cdot \left[C_{\mu_o H} \frac{\partial T_r}{\partial t} + T_r \left.\frac{\partial s_r}{\partial \mu_o H}\right|_T \cdot \frac{\partial \mu_o H}{\partial t} - m_{irr} \left|\frac{\partial \mu_o H}{\partial t}\right| \right] \tag{15}$$

This is the final regenerator energy balance equation including the hysteresis effects, which are expressed in terms of the irreversible mass specific magnetization (m_{irr}).

As described by Brey et al. [77], m_{irr} can be calculated using:

$$m_{irr}\,(T, \mu_o H) = \frac{\left| m_{neg}\,(T, \mu_o H) - m_{pos}(T, \mu_o H) \right|}{2} \tag{16}$$

Where, at a fixed temperature, m_{neg} is the magnetization measured when the magnetic field variation is decreasing and m_{pos} is when the magnetic field increasing [77]. It is important to note that this method of including magnetic hysteresis will tend to overestimate the effects of irreversible magnetization because it assumes the path is defined by major hysteresis loops.

Fig. 14 presents the vibrating sample magnetometer (VSM) measurements for magnetization as a function of the applied field at different temperatures for $MnFeP_{1-x}Si_x$ FOM. Solid lines represent m_{pos} and dashed lines m_{neg}.

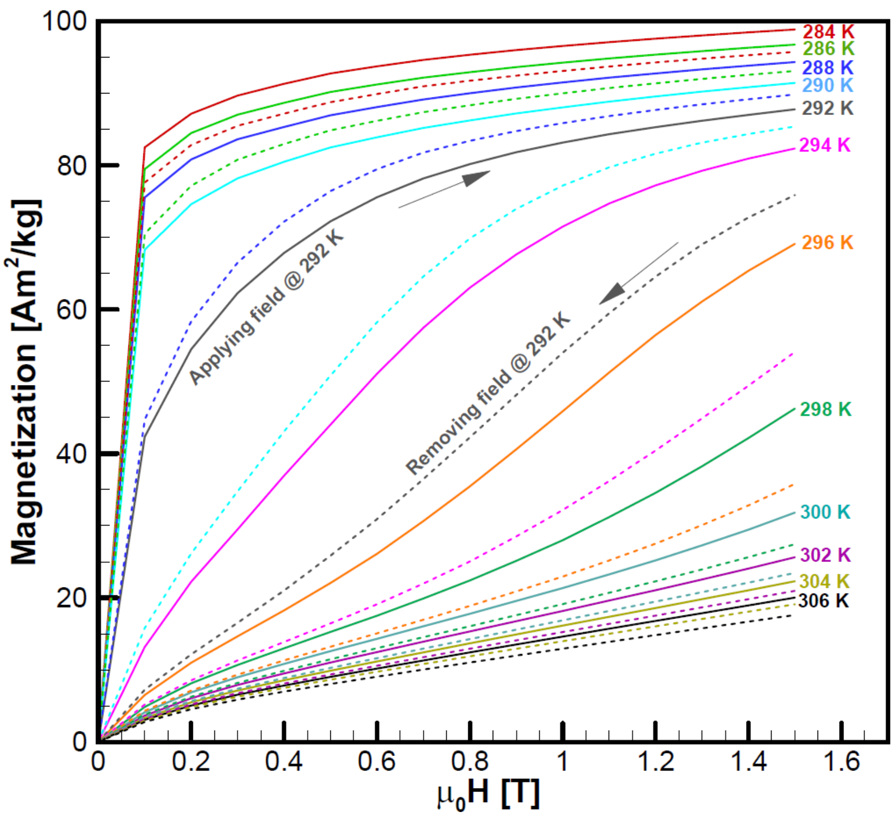

Fig. 14 Magnetization as a function of the magnetic field at different temperatures. The solid lines stands to applying field process and the dashed lines to removing field process.

Fig. 15 shows the irreversible magnetization as a function of the applied field at different temperatures for $MnFeP_{1-x}Si_x$ FOM. Here, a sub-set of isotherms are shown to make the plot easier to read; however, the measurements provide higher resolution over a larger temperature range. As can be seen, near the transition at 292 K, irreversible magnetization,M_{irr}, is on the order of the measured magnetization at fields less than 1 T.

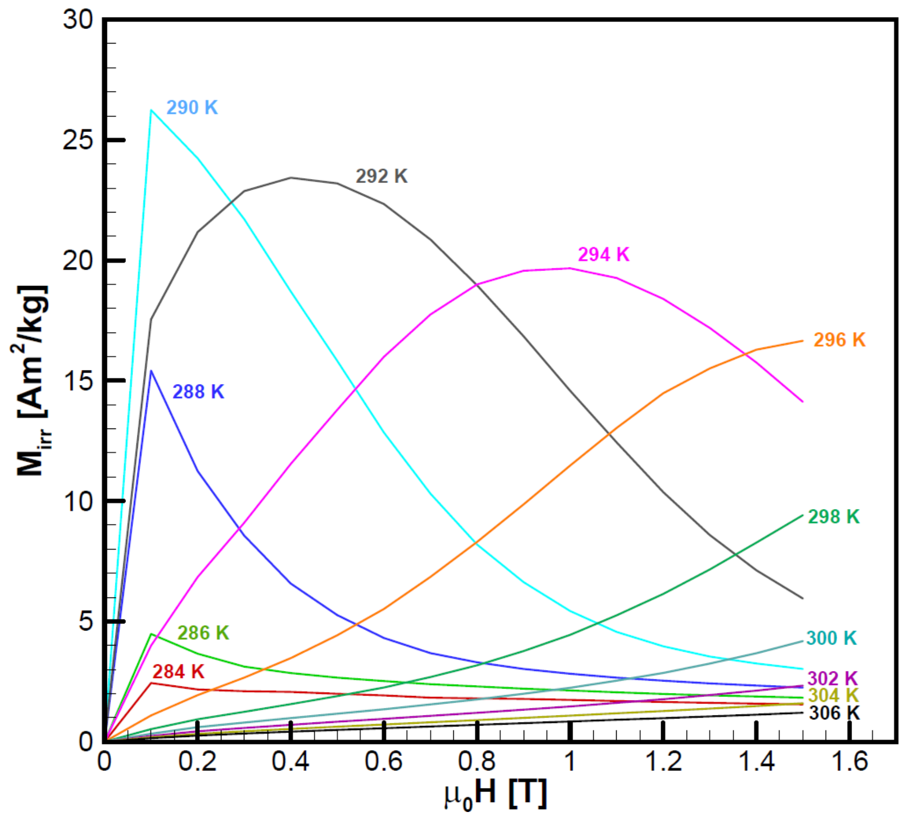

Fig. 15 Irreversible magnetization as a function of the magnetic field at different temperatures.

4.2 MCE implementation

The MCE $\left(\frac{\partial S_r}{\partial \mu_o H}\right)_T$ in Eq. 12 is evaluated for Gd using MFT [116,117], as are the specific magnetization (m), specific heat (C_r), entropy (S_r). For the $MnFeP_{1-x}Si_x$ FOM, these properties are evaluated using an empirical model emulating the specific heat using a Lorentzian fit and integrating to determine isofield entropy curves. A linear response for shift in the temperature for peak specific heat with field is assumed. Resulting entropy curves as a function of temperature and field are then interpolated to determine entropy as a function of temperature.

The effective magnetic field (H) variation with time in the term $\left(\frac{d\mu_o H}{dt}\right)$ corresponds to the waveform characteristic of Nested Halbach cylinders used in the device [25,118,119]. In addition, the effective magnetic field is corrected for demagnetizing effects [120,121], given by:

$$H = H_a - \rho\, N_D\, m(T, H) \tag{17}$$

where H_a is the applied field, N_D is the demagnetization factor, T is the average temperature of the AMR, and $m(T, H)$ is the specific magnetization evaluated using MFT for Gd, while for the FOM the magnetization is experimentally measured via VSM. The density (ρ) for $MnFeP_{1-x}Si_x$ is about 6±0.1 g/cm^3 [69].

Because of hysteresis, the evaluation of $\left(\frac{\partial s_r}{\partial \mu_o H}\right)$ is not straightforward. Fig. 16 presents a representative entropy-temperature diagram for FOM where the thermal hysteresis is the temperature difference between the heating and cooling curves for both, low and high magnetic fields. As discussed elsewhere in Ref. [79], based on data measured using isofield heating and cooling measurements, there are four permutations that one may consider for determining isothermal entropy change. In the present study, two different approaches are used to evaluate the entropy variations: (i) using an average curve (*Av*) between the cooling and heating curves; (ii) using the low field heating and the high field cooling (*HC*) curves, as proposed by [76,79]. These two approaches are shown in Fig. 16 by the *Av* and *HC* labels respectively.

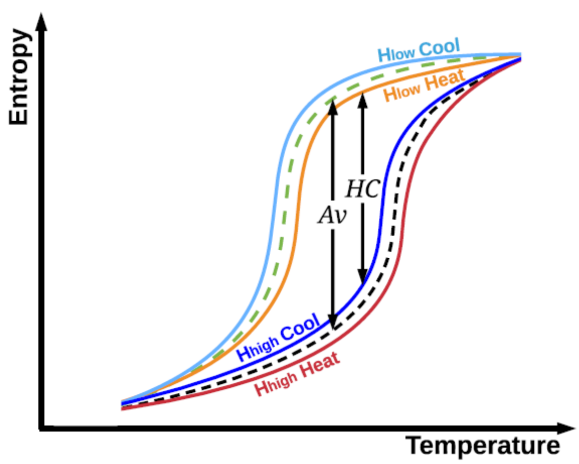

Fig. 16 Schematic drawing showing the two different implementations of the MCE for FOM: using the an average curve (dashed lines) between the cooling and heating curves; using the low field heating and the high field cooling curves.

4.3 Boundary conditions

The fluid flow direction decides the energy balance at the boundaries of the regenerator bed. For the fluid that enters at the edges of the regenerator, the boundary conditions are applied such that in case of dispersive heat transfer, the temperature of the corresponding reservoir and the boundaries does not allow heat loss through the walls.. The boundary conditions are:

Hot to Cold blow $\dot{m}(t_j) \geq 0$, then $T_f(x = 0, t) = T_H$ (18)

Cold to Hot blow $\dot{m}(t_j) < 0$, then $T_f(x = L, t) = T_C$ (19)

4.4 Field waveform

The rectified sinusoidal experimental magnetic field profile was used for the model to estimate the MCE and subsequently the device performance. Fig. 17 shows the PM I experimental field over a complete cycle [25]. The high field portion of the magnetic profile occurs for the first half cycle, corresponding to the warm blow of fluid through the regenerator. The low field portion is the latter half of the cycle and corresponds to the cold blow of the fluid. The mass flow rate is in the positive direction during the high field portion and negative during the low field portion.

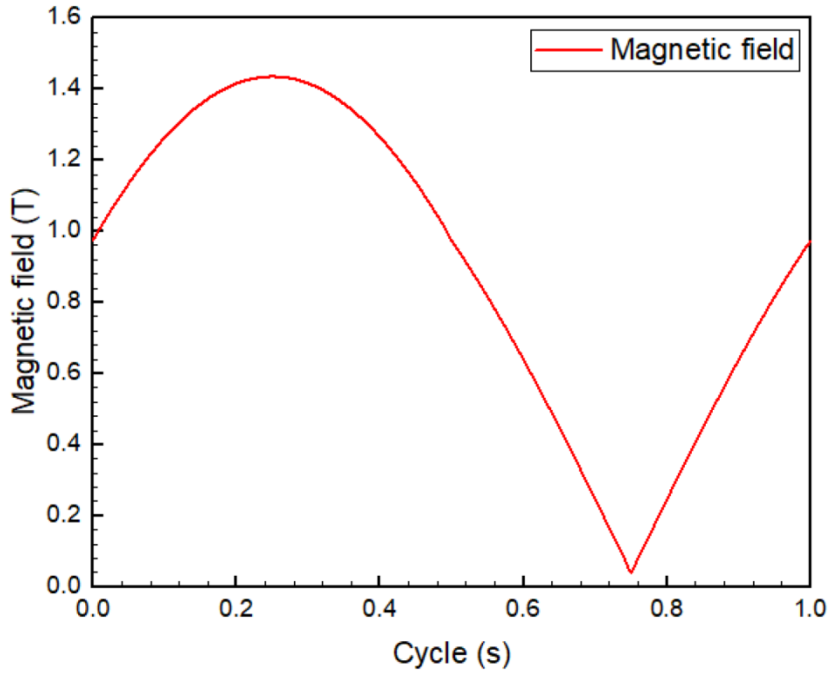

Fig. 17 Sinusoidal experimental field profile with the PM1 device for the high and low field values as a function of time.

4.5 Grid

In the present model, the grid is composed of 120 spatial control volumes and 1000 time steps. Based on the results of runs against different grid sizes, this grid size was proven to be satisfactory taking into account the differences between the converged results and the overall computing time, as seen in Table 3.

Table 3 Summary of results with different grid sizes for T_H =297K, T_C =294, n =1000(time steps) on a PC with 12.0 GB RAM and 2.67 GHz Intel Core i5 processor.

Grid size (volumes)	**Cooling Power ($\dot{Q}_C$) (W)**	**Difference (%)**	**Computing time (s)**
60	12.1809	-	452
120	12.1843	0.027	1165
180	12.1848	4.10e-4	2940

4.6 Solution method

The AMR model input parameters include the regenerator geometry, magnetocaloric and thermal properties, heat transfer fluid properties, operating frequency, temperature span, magnetic field intensity and temporal profile, as well average mass flow rate and flow waveform. The magnetic field profile is selected to represent the PM I device [25]. The mass flow rate follows a sinusoidal waveform characteristic of a double effect pump. The model begins with an initial linear temperature distribution and numerically iterates the partial differential equations forward through time until it reaches a temperature distribution that satisfies the convergence criteria for a periodically developed state. The spatial and numerical mesh are 120 spatial nodes and1000 times steps, which are a result of a mesh study and presented good stability and accuracy combined with a reasonable convergence time. Convergence is reached when the temperature difference between two consecutive profiles is less than the tolerance of 0.0002 K. Fig. 18 indicates the flow chart which describes the numerical simulation procedure. The outputs of the model are the refrigeration capacity (Eq. 20) which is corrected for heat leaks (Eq. 21).

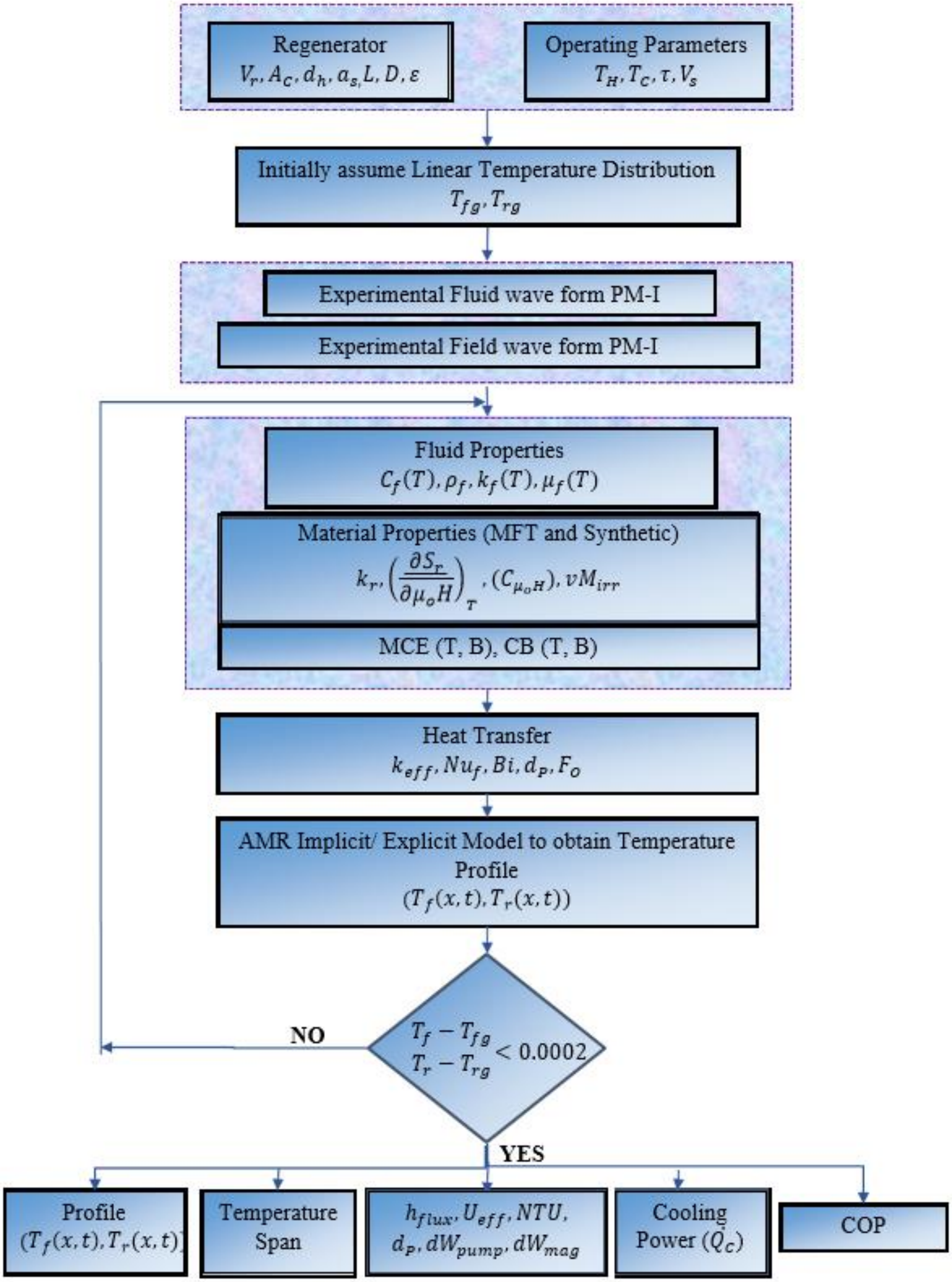

Fig. 18 Model flow chart.

4.7 Performance metrics

The device gross cooling capacity ($\dot{Q}_C$) is calculated based on the enthalpy flux (h_f) at the cold end of the regenerators during a cycle with period τ, and then, multiplied by the number of regenerators (n), as:

$$\dot{Q}_C = \frac{n}{\tau}\int_0^{\tau/2}(h_f(T_c) - h_f\left(T_{f,x=L}\right))\dot{m}dt \tag{20}$$

Where $h_f(T_c)$ is the enthalpy of the fluid at the cold reservoir temperature and $h_f\left(T_{f,x=L}\right)$ is the enthalpy of the fluid at the temperature of the fluid at the cold end of the bed$(x = L)$.

The net cooling power $\dot{Q}_{C,net}$ corrects the gross cooling capacity by the different configuration losses quantified in the PM I test device [107,122], such as: (i) heat leaks from the cold side of PM I to ambient ($\dot{Q}_{amb}$ = 0.28(T_{amb}- T_C) – 0.03); (ii) heat leaks from the cold to the hot side through the PM1 device structure ($\dot{Q}_{HC}$ = 0.1(T_H - T_C)).

$$\dot{Q}_{C,net} = \dot{Q}_C - \dot{Q}_{amb} - \dot{Q}_{HC} \tag{21}$$

The co-efficient of performance (COP), which describes the effective cooling compared to the work input, can be is calculated from the formula

$$COP = \frac{\left|\dot{Q}_c\right|}{\left|W_{pump}\right| + \left|W_{motor}\right|} \tag{22}$$

Where $\dot{Q}_c$ is the cooling capacity, W_{pump} is the pump work and W_{motor} is the motor work per cycle.

The motor work per cycle is defined as

$$W_{motor} = \frac{W_{mag}}{\eta_{motor}} \tag{23}$$

where W_{mag} is the magnetic work per cycle and η_{motor} is the motor efficiency. The pump work per cycle is defined in terms of pressure gradient $\left(\frac{dP}{dx}\right)$ across the bed of the regenerator as:

$$W_{pump} = \frac{1}{\eta_{pump}} \int_0^L \int_0^\tau \left(\left| \frac{\dot{m}(t)}{\rho_f} \frac{dP}{dx} \right| \right) dt\, dx \tag{24}$$

where η_{pump} is the pump efficiency, L is the length of the regenerator bed, and τ is the cycle time.

4.8 Summary

To begin, we start by describing the energy balance equations used in this model for the solid and fluid phases. Then a modified solid equation is used to include the irreversible entropy production term presented. The various components of this 1D model, such as the MCE implementation, boundary conditions, magnetic field profile and grid are presented. The internal and external losses present in an AMR system are then defined for an arbitrary device which leads to an equation defining the total cooling power. The following chapter describes the experimental studies and discusses the main findings.

Chapter 5 Experimental results and discussions

The impacts of thermal hysteresis (Section 5.1 and 5.2) and multi layer beds (Section 5.3) on AMR performance are presented.

5.1 Thermal hysteresis: Single layer Gadolinium and $MnFeP_{1-x}Si_x$

To begin, two different single layer regenerator beds are experimentally characterized: one composed of Gd, which is the benchmark material for AMRs and presents no thermal hysteresis; and a second bed composed of $MnFeP_{1-x}Si_x$ FOM, which has 3 K of thermal hysteresis. The impacts of thermal hysteresis are characterized by heating and cooling experiments, where the rejection (hot side) temperature is varied in a range from 283 to 313 K.

5.1.1 Regenerator beds and material properties

The AMR matrix is composed by the MCM assembled inside a housing. The regenerator house is made of G10 fiberglass tube, with 5/8" diameter. In the present section two different AMRs are prepared, one composed by Gd of spheres (250-600 μm) and a second with $MnFeP_{1-x}Si_x$ FOM are composed of irregular particulate (300-425 μm) coated with a thin layer of epoxy creating a monolithic porous structure so as to bond the particles and constrain them in space. Epoxy content increases the strength between the particles of the material in the regenerators. A sealed cylindrical flow path is created by bonding the magnetic material inside a G10 (Garolite) tube. Photos of a sample regenerator can be seen in Fig. 12, and Table 4 summarizes the main properties of each matrix.

Table 4 Properties for the Gd and the $MnFeP_{1-x}Si_x$ AMRs beds

Properties	**Gd**	**$MnFeP_{1-x}Si_x$**
Transition temperature (K)	293	297
Mass (g/bed)	51.5	50.6
Porosity (-)	0.36	0.42
Geometry	Spheres	Crushed irregular particles
Particle size (μm)	250-600	300-425
Regenerator length (mm)	90	90

Fig. 19 presents characterization data for the Gd and $MnFeP_{1-x}Si_x$ FOM. Fig. 19(a) compares the ΔT_{ad} directly measured, for 1.1 T magnetic field change, for the two materials. In both measurements, *heating* and *cooling* curves are presented. These results show that Gd MCE outperforms the $MnFeP_{1-x}Si_x$ alloy MCE; however,it is expected that the narrower operating temperature range of a single FOM can be overcome by using layered AMR beds [25,47]. The visible shift in the *heating* and *cooling* curves for the $MnFeP_{1-x}Si_x$ alloy is associated with thermal hysteresis, whereas none is observed in the Gd sample.

Fig. 19(b) shows the specific heat capacity as a function of the temperature at 0 T, measured via calorimetry. *Heating* and *cooling* curves are also presented for the $MnFeP_{1-x}Si_x$ alloy. From these data a thermal hysteresis shift of about by 3.5 K is evaluated. Gd presents no thermal hysteresis. As can be seen, the FOM has a much larger specific heat capacity than Gd. It is important to note that even if the material is free of hysteresis, ΔT_{ad} and specific heat are strongly dependent upon temperature and magnetic field, as is well known for Gd.

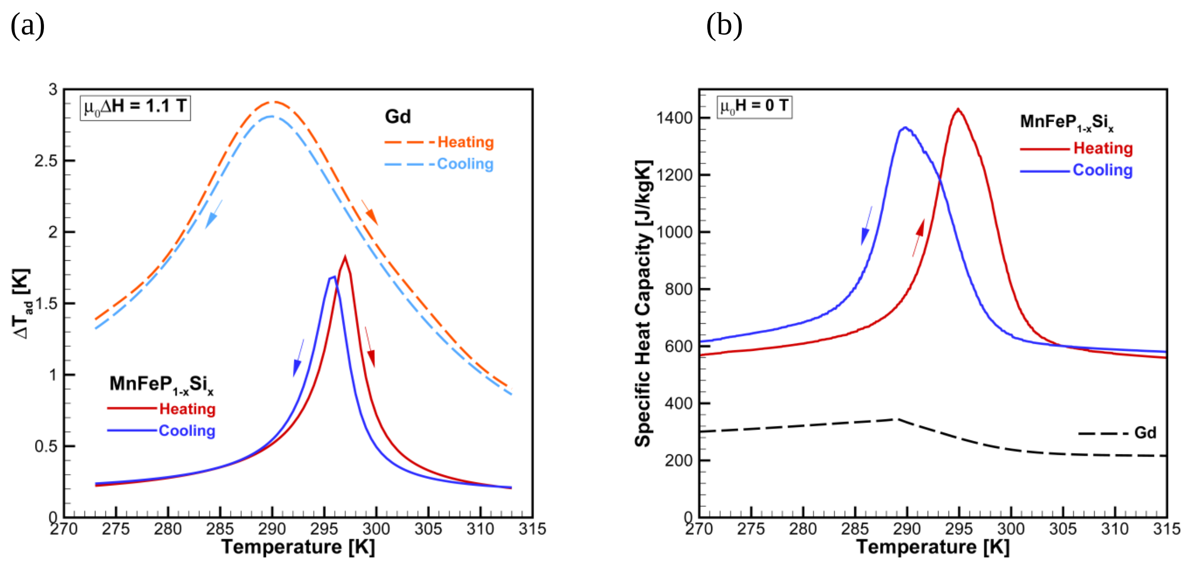

Fig. 19 (a) Direct measured adiabatic temperature change as a function of temperature for Gd and $MnFeP_{1-x}Si_x$, for an applied field change of 1.1 T; (b) Specific heat capacity as a function of the temperature at 0 T, for $MnFeP_{1-x}Si_x$ alloy and Gd. In both cases the thermal hysteresis is characterzed via heating and cooling curves.

5.1.2 Results

The AMR experimental tests are performed in the PM I [25]. Fixed displaced volume of 5.09 cm^3 and frequency of 1.0 Hz are used, while the rejection temperature is varied from 283 K to 313 K, at different heat load conditions. In order to study the irreversibility associated with this FOM material, *heating* (increasing the rejection temperature) and *cooling* (reducing the rejection temperature) measurements are performed. For comparison a Gd AMR with similar geometric parameters is tested using the same experimental protocols. The results are presented in terms of the maximum temperature span as a function of the rejection temperature.

5.1.2.1 Gd and $MnFeP_{1-x}Si_x$

Fig. 20 presents the measured maximum temperature span (T_{span}), at no load conditions, as a function of the rejection temperature for the *heating* and *cooling* processes using the Gd and $MnFeP_{1-x}Si_x$ beds.

The results for Gd show the trends reported elsewhere: as the rejection temperature increases the temperature span increases [22,25] and a maximum temperature span of 26 K at a rejection temperature of 309 K is found. Comparing results for the *heating* and *cooling* processes shows that a single temperature span curve is produced.

The $MnFeP_{1-x}Si_x$ bed, on the other hand, shows a T_{span} peak of about 12 K around T_H = 304 K. Looking at the *heating* and *cooling* curves, we can analyse two different temperature ranges. For temperatures lower than the peak rejection temperature (where maximum span is found), the *cooling* and *heating* curves show little differences. However, at higher temperatures the *cooling* curve underperforms the *heating* curve up to a temperature of ~ 312 K. In both cases, the differences may be associated with varying thermal and magnetocaloric properties due to the thermal hysteresis. This behaviour is discussed in more detail in section 5.1.3.1.

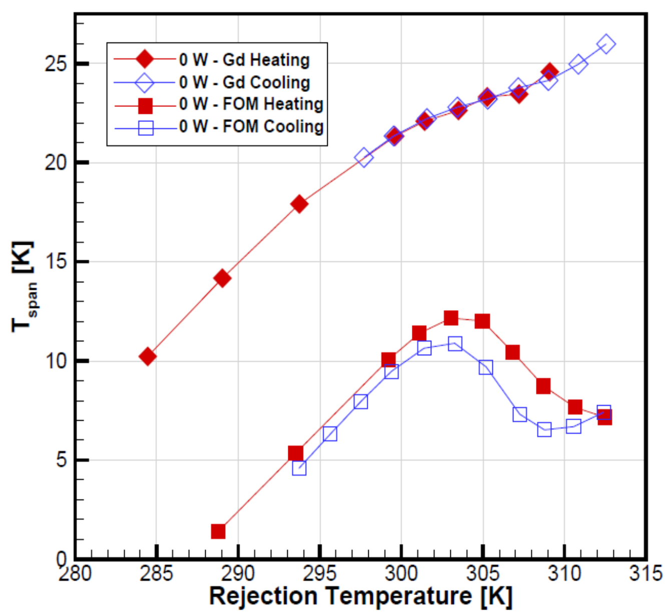

Fig. 20 A comparison of the maximum temperature span as a function of the rejection temperature for the Gd and $MnFeP_{1-x}Si_x$ beds at no heat load conditions.

5.1.2.2 $MnFeP_{1-x}Si_x$

Fig. 21 shows the temperature span at 0 W, 5 W and 10 W conditions as a function of the rejection temperature. This time, only the $MnFeP_{1-x}Si_x$ bed is considered. As the applied load increases, the maximum T_{span} decreases and the rejection temperature where the peak is found shifts to lower T_H: for 0 W the peak is around 304 K; for 5 W around 302 K; and for 10 W around 300 K. Again, the *cooling* curve underperforms the *heating* curve for the 0 and 5 W curves. Nevertheless, the 10 W curve does not present any differences, possibly because the 10 W curve has positive T_{span} at a narrow T_H range (T_H < 302 K), where the hysteresis effects are less important. For T_H < 302 K the 0 W and 5 W curves also present little differences for the *heating* and *cooling* curves.

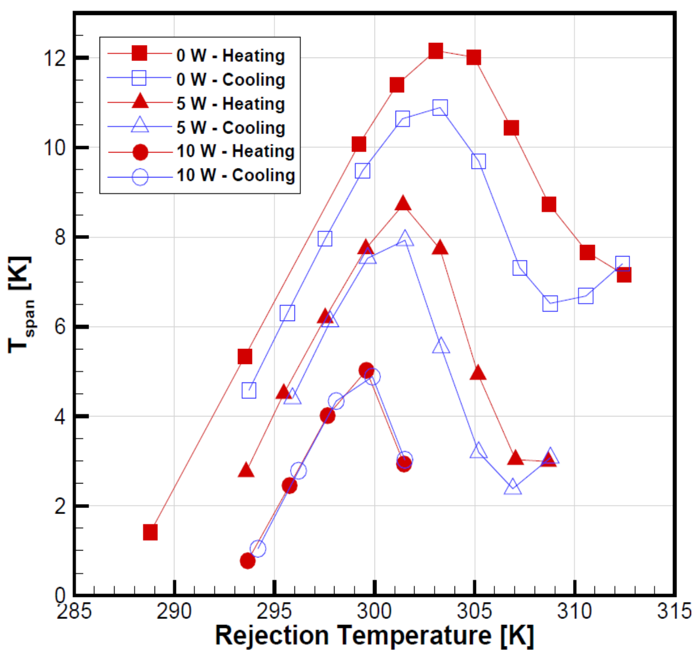

Fig. 21 A comparison of the maximum temperature span as a function of the rejection temperature for the $MnFeP_{1-x}Si_x$ regenerator at 0 W, 5 W and 10 W load conditions.

5.1.3 Discussion

Comparing first the results for Gd and $MnFeP_{1-x}Si_x$ AMR in Fig. 20, one can see that the Gd bed outperforms the FOM bed under zero applied load. This is expected given that the amplitude and width of the ΔT_{ad} is considerably larger for Gd than for the FOM. For the range of temperatures presented in Fig. 19(a), Gd has an average ΔT_{ad} of about 2 K, while for the Mn-based FOM material it is ~0.5 K. However, even with a much lower average MCE, the FOM develops a significant temperature span. One of the main differences between the two regenerators is the thermal mass where the FOM specific heat is much larger than Gd. Hence, for similar NTU, $\left(\frac{h\,A}{\dot{m}\,C_p}\right)$ the thermal effectiveness of an FOM regenerator can be higher than a Gd bed for the same operating conditions.

For the $MnFeP_{1-x}Si_x$ AMRs, depending on the T_H range, deviation between the *heating* and *cooling* curves is seen with the *cooling* curve giving a lower temperature span than the *heating* process. The maximum deviation was at 0 W and T_H ~ 307 K, where the T_{span} for the *heating* curve is about 3.5 K higher than the span for the *cooling* curve. One of the possible causes of such difference are related to the thermal and magnetocaloric properties variations due to thermal hysteresis, characteristic of FOM. The Gd bed did not presented any hysteresis effects when tested following the same *heating* and *cooling* protocols.

Fig. 21 presents the experimental temperature spans as a function of the rejection temperature for applied heat loads of 0, 5, and 10 W and for *cooling* and *heating* protocols for the $MnFeP_{1-x}Si_x$ AMR. For a given hot side temperature, the temperature span increases as load is reduced. However, the iso-load curves are not monotonic, showing that equivalent spans can be achieved at more than one rejection temperature. In addition, the *cooling* and *heating* curves can show significantly different spans for a given hot side temperature, i.e. thermal hysteresis in measured span is observed. It appears that the thermal hysteresis between the *heating* and *cooling* curves is proportional to the temperature span, i.e. with an applied load of 10 W, no measureable difference in span is observed between the two measurement protocols. Hysteresis is also less pronounced when the rejection temperature is less than the point where maximum span is measured.

5.1.3.1 Multiple points of equilibrium

Recently, Niknia et al (2018) [123] presented the first observations and explanation of multiple points of equilibrium (MPE) in active magnetic regenerators using an FOM. The analysis suggests that MPEs can arise without material hysteresis and can reduce the AMR dynamic performance. The work also suggests that MPEs may be avoided by constraining operating conditions to a certain range. Until now, the phenomena of MPEs have not been discussed in the literature. Niknia et al reported that a detailed numerical analysis with fine resolution is utilized to study the behavior of cooling power curves. *Heating* and *cooling* curves of temperature span are simulated and compared to experimental measurements. It is numerically observed that for certain operating conditions, MPE can be identified. As a result, two or more temperature spans can be obtained for the same hot side temperature which is consistent with our Fig. 21 experimental findings. L.von moos et al [59] performed similar experiments where they studied MnFe(P,As) in an AMR. They reported that the curve of temperature span as a function of hot side temperature for the heating procedure shifts to the right of the cooling curve by 1.1 K. This behaviour was attributed to thermal hysteresis of the material which was also ~1.1 K. Based on the MPE phenomenon predicted for FOMs, the experimental results for hysteresis in Fig. 21 can be interpreted as MPEs. The experimental results show that the MPEs tend to approach each other as the losses and loads increase. Another important characteristic of the PEs seen in Ref. [123] is that a larger temperature span corresponds to heating mode while a smaller temperature span is associated with cooling mode. Similar behaviors are observed in Fig. 21 where *heating* curves correspond to a larger temperature span than the *cooling* curves at rejection temperatures greater than the peak, and, hysteresis decreases with load. Such similarities in behavior suggest that MPE phenomena are impacting FOM behaviour seen in AMR cycles; however, MPE results alone do not fully explain the measured data.

5.1.4 Summary

Two different single layer AMR beds composed by Gd and $MnFeP_{1-x}Si_x$ FOM were prepared and tested using PM I device. The results indicate a hysteresis for the *heating* and *cooling* temperature span for FOM regenerator. The results are explained by multiple points of equilibrium (MPE) phenomena related to both material and device characteristics.

5.2 Thermal Hystersis : Three multilayer $MnFeP_{1-x}As_x$ FOM regenerators

Significant hysteresis and MPE are observed in single layer AMR using FOM $MnFeP_{1-x}Si_x$ in Section 5.1. However, no information about the presence of hysteresis and MPEs have been reported for multilayer regenerators. With this objective, the present work advances our understanding of layered AMR performance using $MnFeP_{1-x}As_x$ FOM by systematic experimental testing. Regenerators comprised of two and three layers are characterized with experiments using the PM I [25]. The impacts of thermal hysteresis have been characterized by *heating* and *cooling* experiments, and therefore, the rejection temperature (hot side) temperature is varied in a range from 283 to 300 K. The existence and magnitude of MPEs are found using *heating* and *cooling* experiments. The results are presented on the basis of measured temperature span as a function of rejection temperature for no-load and applied load conditions.

5.2.1 Regenerator beds and material properties

The AMR matrix consists of particles of MCM assembled inside a housing. The regenerator housing is made of G10 fiberglass tube with a 16 mm ID. In the present work three different beds made of $MnFeP_{1-x}As_x$ FOM are tested: a two-layer regenerator and two different three-layer configurations where the intermediate layer is varied while the warm and cold layers remain the same. One three-layer composition uses MCE material with a lower ΔT_{ad}; in the second three-layer AMR, the intermediate layer uses MCE material with a higher ΔT_{ad}.

Table 5 presents the regenerator properties. The data for the peak ΔT_{ad} and the temperature where the peak is found, T_{peak} are based on the synthetic model results for a magnetic field variation from 0.5 T to 1.1 T. The transition temperature, T_{Curie}, values are those for the *heating* maximum specific heat at 0 T [79].

Table 5 Multi-layer $MnFeP_{1-x}AS_x$ FOM regenerator properties (0.5-1.1 T field change).

Properties	**2-layers**		**3-layers, Lower-MCE**			**3-layers, Higher-MCE**		
	$\mathbf{L_C}$	$\mathbf{L_W}$	$\mathbf{L_C}$	$\mathbf{L_I}$	$\mathbf{L_W}$	$\mathbf{L_C}$	$\mathbf{L_I}$	$\mathbf{L_W}$
T_{Curie} [K]	283.2	291	283.2	285	291	283.2	287	291
T_{Peak} [K]	287.3	295.1	287.3	289.4	295.1	287.3	291.1	295.1
PeakΔT_{ad} [K]	1.72	1.72	1.72	1.27	1.72	1.72	1.72	1.72
Hysteresis [K]	2.5	2.0	2.5	2.3	2.0	2.5	1.5	2.0
Mass [g/layer]	29.00	28.3	19.2	16.9	18.7	19.5	19.2	18.9
Total mass [g/bed]	28.3			28.0			28.7	
Layer Length [mm]	22.5	22.5	15	15	15	15	15	15

All the $MnFeP_{1-x}As_X$ layers are made of crushed irregular particles sieved in a range of 300-425 µm. The porosity is approximately 0.5 and each regenerator has the same total length of 45 mm. In the case of the two material regenerator, each layer is 22.5 mm long while in the three material cases, each layer is 15 mm long. The intermediate layer (L_I) of the three layer beds are composed of two different materials with similar T_{Curie} but different ΔT_{ad} and hysteresis.

Fig. 22 presents the ΔT_{ad} as a function of temperature for $MnFeP_{1-x}As_X$. Fig. 22(a) shows the directly measured ΔT_{ad} data for the three material case where the intermediate layer, L_I, has a lower ΔT_{ad}. Fig. 22(b) shows the three material case where the intermediate layer has a higher ΔT_{ad}. The cold layer, L_C, and warm layer, L_W, are the same materials for the two cases (only the intermediate composition changes.) The (experimental) direct measurements use a magnetic field variation from 0 T to 1.1 T and are measured using the device described in Ref. [79]. *Heating* (red lines and arrows) and *cooling* curves (blue lines and arrows) are shown indicating a small thermal hysteresis.

Three additional sets of points overlay the measured data (light blue, green, and orange) in Fig. 22(a) and (b). These points represent predicted ΔT_{ad} data using a synthetic model for material properties [124]. The synthetic model approximates isofield specific heat curves as a function of temperature using Lorentzian functions. An asymmetric curve is created by fitting the specific heat using two Lorentzian functions, one for temperatures less than that for the peak specific heat and another for temperatures greater than the peak (i.e. one for the left and another for the right.) The specific heat for any field is then determined assuming the transition shift is linear with field. Integration of specific heat provides entropy curves which are interpolated for ΔT_{ad} and ΔS_m.

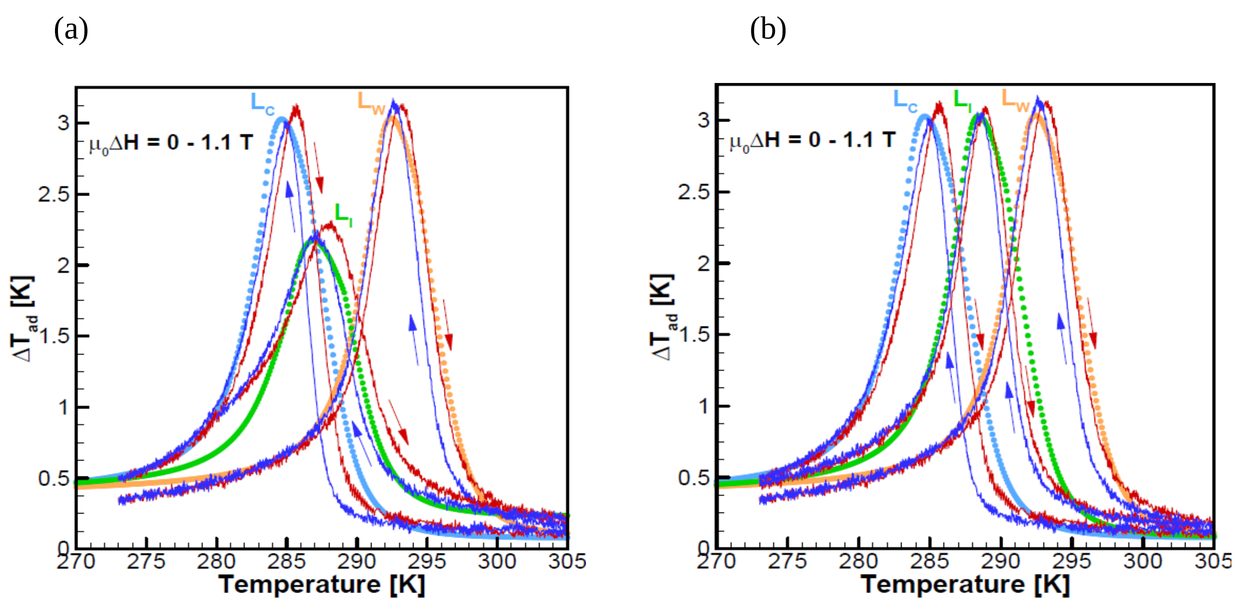

Fig. 22 Adiabatic temperature change as a function of temperature for MnFeP1-xAsx (a) directly measured ΔT_{ad} data for the case where the intermediate layer has a lower ΔT_{ad}; (b) directly measured ΔT_{ad} data for the case where the intermediate layer has a higher ΔT_{ad}. The magnetic field changes from 0 to 1.1 T, and heating (red) and cooling (blue) measurements are shown. Solid lines are model data.

One of the benefits of using two Lorentzian functions to fit the data is that the asymmetry in measured ΔT_{ad} is captured. As seen in Fig. 22(a) and (b) for 0 - 1.1 T field change, the synthetic model closely matches the $MnFeP_{1-x}As_x$ samples with larger $\Delta T_{ad.}$ The model fit shows some deviations for the low ΔT_{ad} material at temperature 5 - 10 K below the peak temperature. The parametric fits to specific heat are used to estimate the layer properties when the average field changes for PM I are applied (i.e. 0.5 – 1.1 T).

5.2.2 Results

Fig. 23-Fig.25 show the temperature span as a function of the rejection temperature for the 2-layers, 3-layers with lower ΔT_{ad} intermediate layer and 3-layers with higher ΔT_{ad} intermediate layer, respectively. The tests are performed in the PM I test apparatus with a fixed displaced volume of 3.9 cm^3 and a fixed operating frequency of 1 Hz. Applied loads, Q_c, vary between 0 W to 12.5 W, depending on the beds. The red filled symbols show results for the *heating* procedure, while the blue open symbols show the *cooling* procedure. The uncertainties for T_{span} and applied load are 0.7 K and 2% of the reading, respectively.

The results for T_{span} as a function of T_H show similar trends for all the AMR beds, i.e., T_{span} shows a peak at a certain T_H. Also, as the applied load increases, the maximum T_{span} decreases and the rejection temperature where the peak is found shifts to lower T_H. The dashed line is a guide to the eye showing the relationship of peak span and rejection temperature as a function of load.

5.2.2.1 Two layer

For the 2-layer bed, Fig. 23, a maximum T_{span} (0 W) of about 11.5 K is found for the heating curve at T_H around 293.6 K. For the applied load cases, the peaks of T_{span} are: ≈9 K around 292.5 K for 2.5 W; ≈6.3 K around 291.5 K for 5 W; ≈3.7 K around 290 K for 7.5 W. For a given applied load, the peak spans are found with the *heating* experiments.

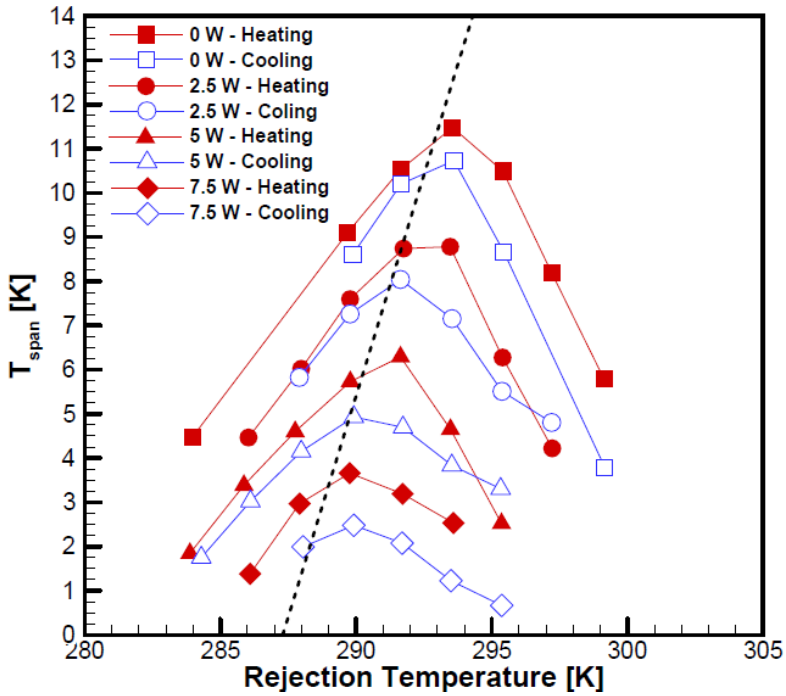

Fig. 23 T_{span} as a function of the rejection and applied load for 2-layers regenerator.

5.2.2.2 Three layer regenerator with lower ΔT_{ad} intermediate layer

For the 3-layers bed with the lower ΔT_{ad} intermediate layer, Fig. 24, the no-load curves (*heating* and *cooling*) are almost identical to those for the 2-layers bed, where a maximum span of about 11.5 K is found for the *heating* curve at T_H around 293.7 K. Thus, for the zero applied load condition, the intermediate layer makes no significant contribution towards achieving larger temperature spans. However, as the applied load is increased, the regenerator is found to sustain larger spans than the 2-layer structure showing peaks for T_{span} of: ≈7.9 K around 292 K for 5 W; ≈5.6 K around 290.5 K for 7.5 W.

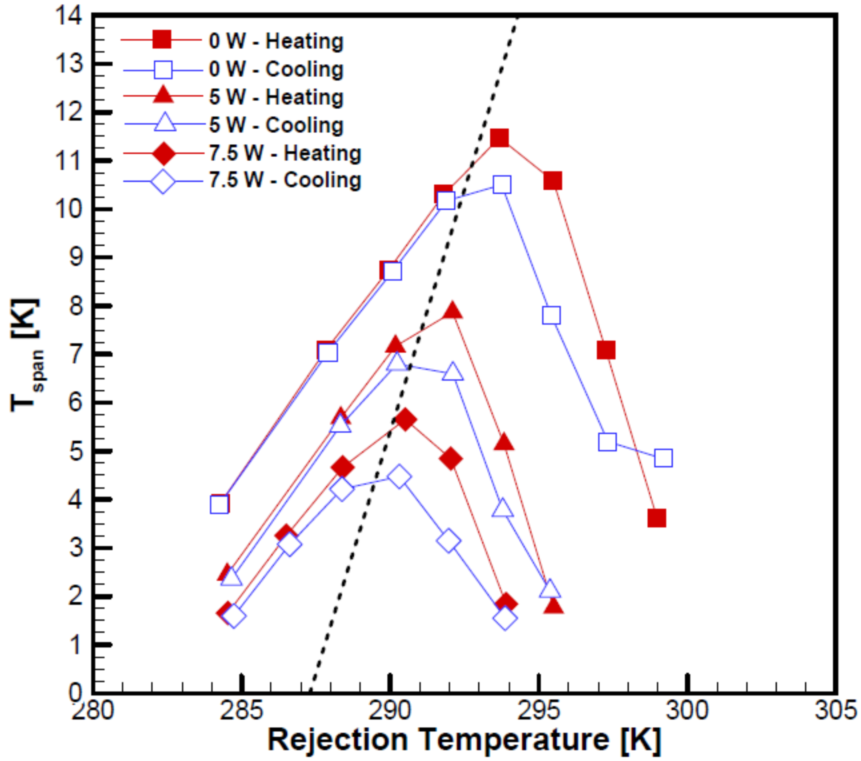

Fig. 24 T_{span} as a function of the rejection temperature and applied load for 3-layer regenerator with lower ΔT_{ad} intermediate layer.

5.2.2.3 Three layer regenerator with higher ΔT_{ad} intermediate layer

The 3-layers bed with higher ΔT_{ad} intermediate layer, Fig.25, outperforms the others with a maximum span of about 13.2 K found near T_H around 294.5 K. For this case, the intermediate layer increases the entropy pumping ability of the beds. Applied loads up to 12.5 W maintain positive spans, where the peaks of T_{span} are: ≈9.3 K around 292 K for 5 W; ≈7.0 K around 290.5 K for 7.5 W; ≈5.7 K around 290.5 K for 10 W; ≈3.0 K around 288.8 K for 12.5 W.

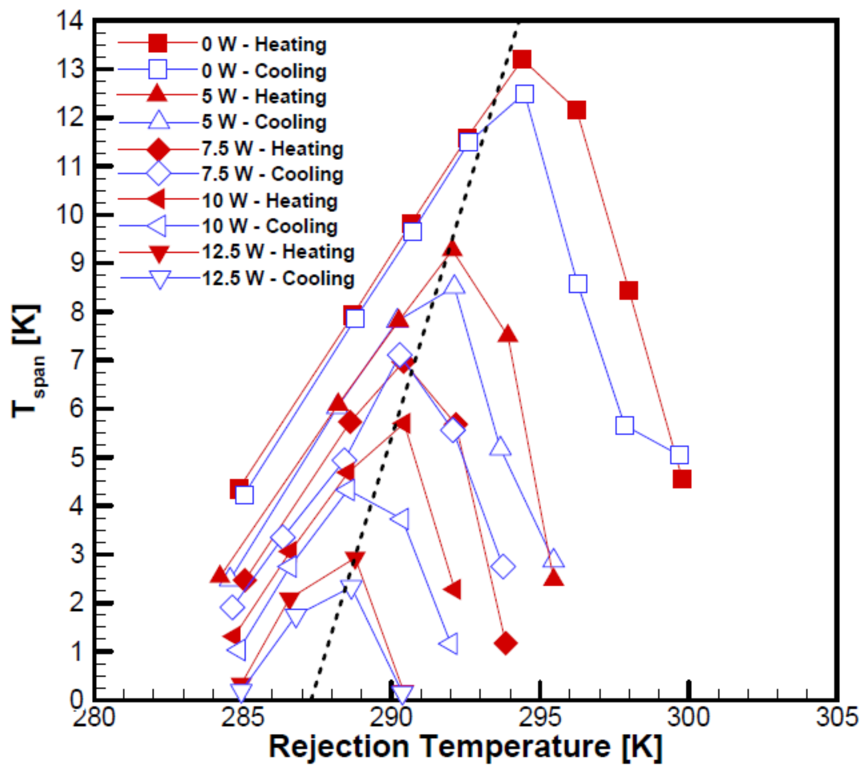

Fig.25 T_{span} as a function of the rejection temperature and applied load for 3-layer regenerator with higher ΔT_{ad} intermediate layer.

5.2.3 Discussion

5.2.3.1 Exergetic cooling power

Useful cooling power can be quantified by the exergetic equivalent cooling power, $\dot{E}x_Q$, defined as [47],

$$\dot{E}x_Q = \frac{\dot{Q}_C}{T_C} T_{span} \tag{25}$$

This quantity reflects the thermodynamic value of the refrigeration effect and is equivalent to the ideal (minimum) work input. Exergetic power can be increased by using larger field strengths, B_O, and more MCM, V; however, both of these parameters tend to adversely impact the cost of a device. An alternative metric which captures the effects of these parameters is the specific exergetic cooling power, μ.

$$\mu = \frac{\dot{E}x_Q}{B_O V} \tag{26}$$

The specific exergetic power may be determined using field volume, regenerator volume, or volume of the material. The choice depends upon what is being compared – the material, the regenerator, or the device itself. Here, we are only varying regenerator composition within the same device; in this case regenerator or material volume is an appropriate reference. Because we keep field, regenerator and material volumes constant, the relative change in exergetic power corresponds to change in specific exergetic power.

Fig. 26 - Fig. 28 show the experimental data in terms of $\dot{E}x_Q$ versus rejection temperature for *heating* and *cooling*. These plots show that although maximum temperature spans vary by less than 20% between all regenerators, the useful cooling power for a 5 W applied load increases from a peak of ≈0.04 W for the 2-layer case to ≈0.16 W for the 3 layer case: an improvement of ≈200%. Thus, a clear benefit of layering is seen where performance is increased significantly while the regenerator volume is unchanged.

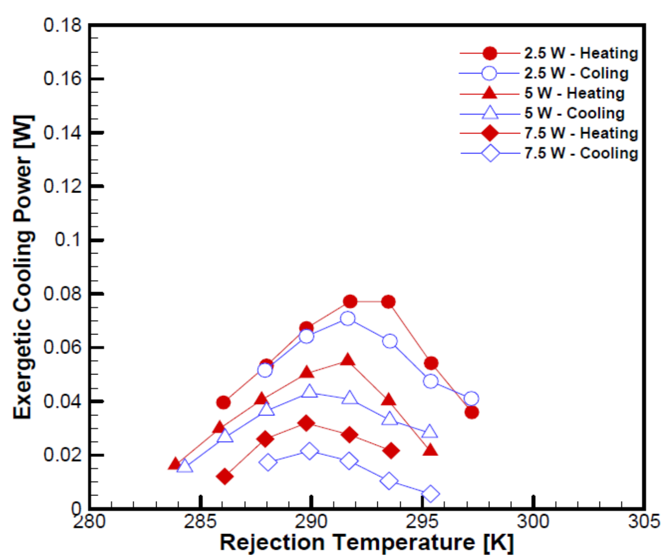

Fig. 26 $\dot{E}x_Q$ as a function of the rejection temperature and applied load for the 2-layer regenerator.

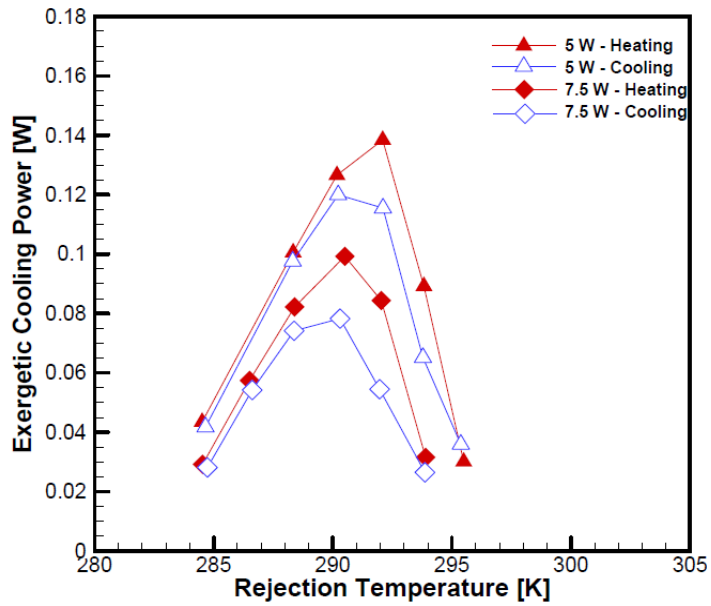

Fig. 27 $\dot{Ex}_Q$ as a function of the rejection temperature and applied load for the 3-layer regenerator with lower ΔT_{ad} intermediate layer.

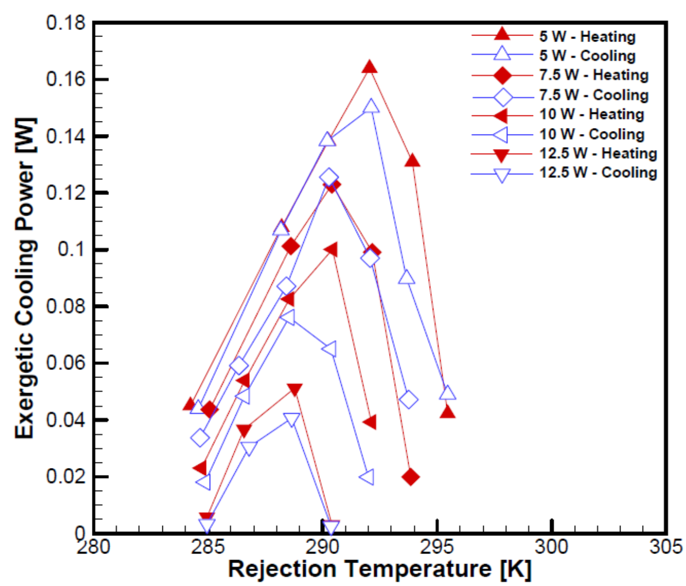

Fig. 28 $\dot{Ex}_Q$ as a function of the rejection temperature and applied load for the 3-layer regenerator with higher ΔT_{ad} intermediate layer.

5.2.3.2 Active layers

The addition of an intermediate layer with activity in a temperature range between the hot and cold layers increases AMR performance. Furthermore, the increase in exergetic power is larger when an intermediate material with larger ΔT_{ad} is used. The benefit of the warm layer for each configuration is not obvious as this layer is unchanged for all tests. We can infer the efficacy of the warm layer based on the material ΔT_{ad} model. Fig. 29 (a) and (b) show model data for ΔT_{ad} where the field change is from 0.5 T to 1.1 T. These are the average fields of the PM I magnetic field waveform over each fluid flow period including a correction that approximates demagnetization effects [122].

Compared to Fig. 22 where the field change is 0 - 1.1 T, the impact of 0.5 - 1.1 T is to reduce the amplitude and shift the peak ΔT_{ad} to a higher temperature. For the L_c material, the maximum ΔT_{ad} is at 287.3 K whereas for the L_w material, the peak is at 295.1 K. The dashed lines in Fig. 23 -Fig.25 intercept T_H at 287.3 K which corresponds to the temperature where the peak ΔT_{ad} is found for L_c. The slopes of the dashed lines in Fig. 23-Fig.25 are equal to 2. Because of this, any point on the dashed line represents an operating condition that straddles the peak temperature for L_c, i.e the average of T_H and T_C is 287.3 K.

For all three regenerator configurations, we see that differences between the *heating* and *cooling* curves are greatest when the mean of T_H and T_C is greater than the peak temperature for L_c. We also see that maximum spans and maximum exergetic powers are found when the mean of T_H and T_C is near 287.3 K. These results suggest that the warm layer mostly operates below its peak temperature for ΔT_{ad}.

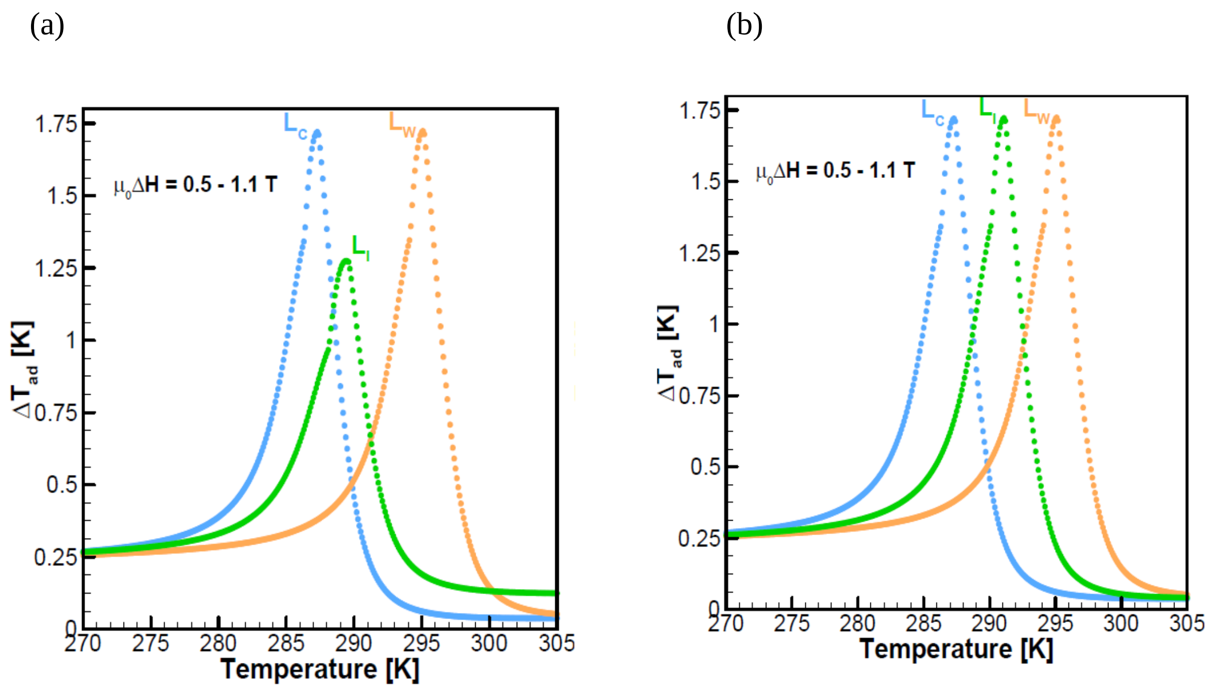

Fig. 29 Adiabatic temperature change as a function of temperature for $MnFeP_{1-x}As_x$ for a magnetic field change from 0.5 T to 1.1 T. (a) low ΔT_{ad} middle layer (b) high ΔT_{ad} middle layer.

5.2.3.3 Multiple points of equilibrium

As seen in Fig. 23-Fig. 28 the *cooling* curves tend to under-perform the *heating* process. For example, in Fig. 24 at 0 W and a fixed T_H of ≈295.5 K, two different T_{span} are possible: ≈10.5 K for the *heating* curve, and ≈8 K for the *cooling* curve. The differences between the *cooling* and *heating* curves are more pronounced for T_H higher than the peak and tend to decrease as T_H is reduced to lower than the peak T_{span}. The ability to sustain two different spans for a given rejection temperature is a phenomenon called MPE.

As described elsewhere [123], AMRs composed of MCMs where specific heat and ΔT_{ad} show a strong sensitivity with temperature can result in MPEs. MPEs can be stable and unstable, reflecting the ability to maintain the operating condition when subjected to a perturbation. When the AMR is operating near an unstable point, the cold end temperature will migrate to the nearest stable equilibrium point. The stable operating condition reached depends on the system and the dynamic history for T_H, i.e. is the change in rejection temperature following a *cooling* or *heating* path. System factors include field waveform and heat leaks. Ref. [123] also found that MPEs arise for $T_H > T_{max,span}$ which is similar to the results presented here for multilayer FOM beds.

An interesting difference between the single layer results in [123] and results shown here with more than one layer, is that for a single layer, the hysteresis tends to decrease as thermal load is increased. In the present results for multilayer AMRs, the differences between the *cooling* and *heating* curves are more noticeable for the no-load conditions; however, as the applied load increases, there is no longer a systematic reduction in hysteresis. For example, in the case of the 3-layer bed with higher ΔT_{ad} intermediate layer (Fig.25), the differences in *cooling* and *heating* tend to reduce as the load increases. For the remaining beds, differences between points of equilibrium remain as load increases and span decreases. The only difference between the three-layer beds is the intermediate layer. Hence, the difference in performance for these two may be explained by variations in specific heat and ΔT_{ad} of the intermediate layers that occur due to changes in rejection temperature. If one looks at L_I in Fig. 29(a) and (b), ΔT_{ad} has large variations in the temperature range from 286 K to 295 K, where the intermediate layer is active.

5.2.4 Summary

The 2-layers, 3-layers with lower ΔT_{ad} intermediate layer and 3-layers with higher ΔT_{ad} intermediate layer AMRs are tested in the PM I test apparatus under different operating conditions. Each regenerator is tested via *heating* and *cooling* experiments. The existence of MPEs are found using *heating* and *cooling* experiments for all the beds. Unlike the single material results, hysteresis in temperature span does not monotonically decrease as applied load is increased. The following section examines layered AMRs designed for large temperature spans using many layers of $MnFeP_{1-x}As_x$ material.

5.3 $MnFeP_{1-x}As_x$ multilayer active magnetic regenerators

This section describes experimental investigations of $MnFeP_{1-x}As_x$-based multilayer AMRs. Five different multilayer beds are tested: (i) one with 3-layers; (ii) one with 6-layers; and (iii) three, 8-layer regenerators. In the 8-layer cases, the material composition remains the same (i.e., same transition temperature,) but the layer thickness is altered such that regenerator mass varies for the same targeted operating span. The distribution of layer thickness in all regenerators is constant. The experiments are performed in the PM II [22] test device under several different operating conditions. Two different operating frequencies (0.5 and 0.8 Hz) are used. The displaced fluid volume ranges from 3.8 to 12.7 cm^3 while the rejection temperature varies between 284 and 312 K. The results are mainly reported in terms of no-load temperature span as a function of the rejection temperature. The 3-layer bed is also tested under load. The longer 6 and 8-layer AMRs are not tested under load conditions due to lifetime concerns resulting from high pressure drop.

5.3.1 FOM regenerator beds and material properties

The regenerator beds in the present work are made of $MnFeP_{1-x}As_x$ FOM in a multilayer configuration. The layered matrices are shown in Fig.30(a) in terms of the layer transition temperatures (*Tc*) as characterized by zero field DSC measurements using a *heating* protocol. The thermal hysteresis, as determined from specific heat measurements, is between 1.1 to 2.7 K for all materials. Fig. 12 is a picture of a sample regenerator ready to be tested.

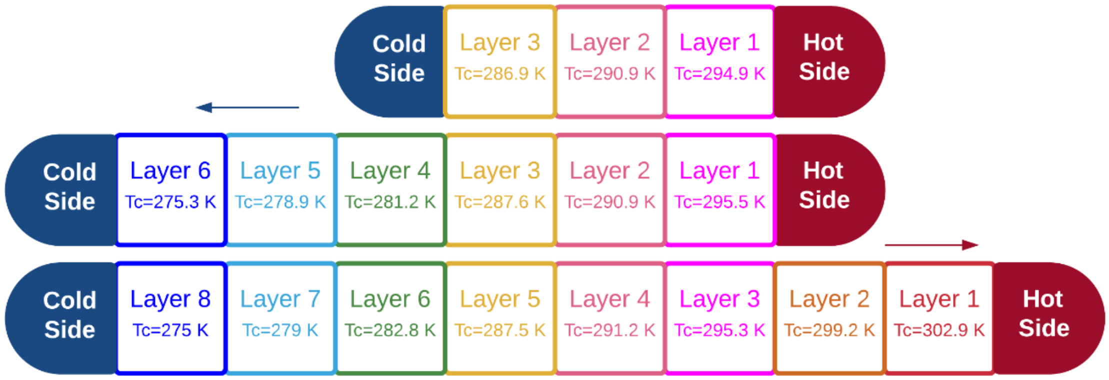

Fig.30 FOM multilayer regenerators: Layer composition for the FOM regenerators, which the reference transition temperature presented is characterized via DSC measurements considering a heating protocol.

The regenerator matrices are made of irregular particulate with an effective diameter range of 300-425 μm. The particulate is coated with a layer of proprietary epoxy creating a monolithic porous structure; the epoxy content is ~ 2 %wt. A sealed cylindrical flow path is created by bonding the monolithic structure inside a G10 tube. All tubes have a 22.2 mm inside diameter (ID) and 24.2 mm outside diameter (OD). The regenerator length, mass, layer thickness and porosity are summarized in Table 6. The three 8-layer beds are constructed in a similar manner where the layer thicknesses are 5, 10, and 15 mm resulting in a short, medium (med) and long regenerator.

Table 6 FOM regenerators structural information. All beds are made of irregular particles (300-425 μm) and are cylindrical with a matrix outer diameter of 22.2 mm.

	Regenerator Composition				
Parameter	**3-layer**	**6-layer**	**8-layer**		
			short	**med**	**long**
Nominal total length [mm]	42	60	40	80	120
Layer thickness [mm]	14	10	5	10	15
Bed mass [g]	57.6	76.5	53.1	108.5	158.0
Porosity [-]	0.53	0.48	0.46	0.45	0.46

The 3-layer bed is designed so that the transition temperature for layer 1 (numbering from warmest to coldest) is ~295 K and layer 3 is ~287 K. The middle layer (2) lies approximately half way between the hot and cold layers with a transition of ~291 K. The 6-layer bed adds additional materials on the cold-side while approximately maintaining the characteristics and distribution of properties for the three warm-side layers. Thus, the transition temperature ranges from ~295 K to ~275 K. Finally, the active range of the 6-layer bed is expanded in an 8-layer regenerator by adding two warmer *Tc'*s and keeping the remaining layers approximately the same. Hence, *Tc's* range from ~303 K to ~275 K for an active range of ~30 K.

Fig. 31 presents the ΔT_{ad} for the materials used in each regenerator. ΔT_{ad} data is from direct cyclic measurements [39,125] for an applied magnetic field variation of 0 to 1.1 T. The direct measurements are performed using *heating* and *cooling* protocols. Isothermal entropy change and specific heat measurements of each sample are unavailable; however, representative data for similar compounds can be found in [5,29,49,57,58].

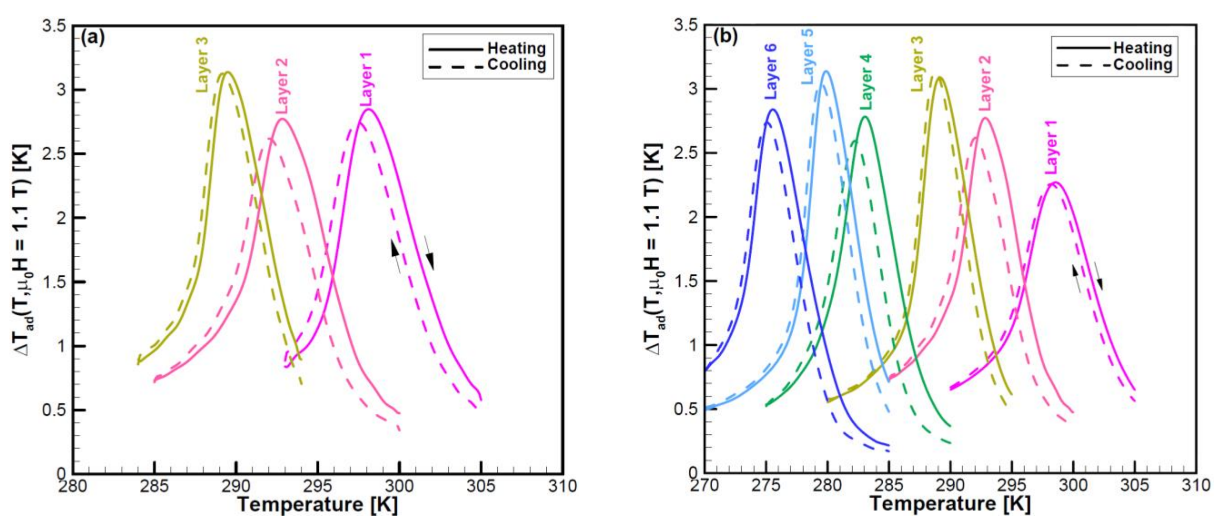

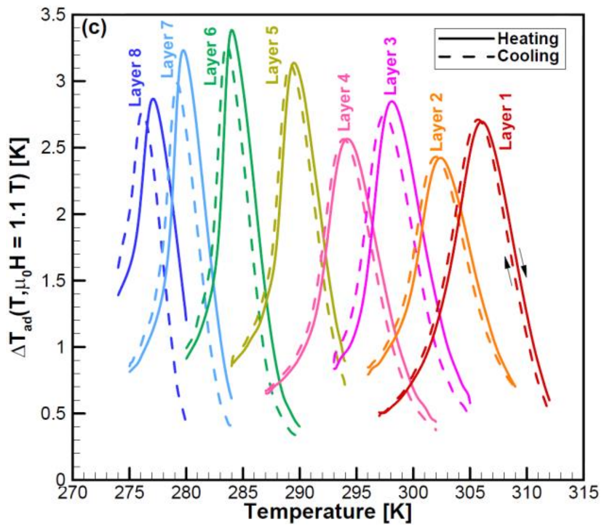

Fig. 31 Direct measured ΔTad as a function of the temperature for the three FOM regenerators: (a) 3-layer; (b) 6-layer; (c) 8-layer. The direct measurements are performed for heating and cooling protocols with a magnetic field variation of 0-1.1 T

5.3.2 Results

Experiments are performed using a custom test apparatus (PM II) built at the University of Victoria [22]. The tests conditions (frequency and displaced volume) vary depending on which regenerator is being tested. Pressure drop is the limiting constraint and impacts maximum frequency and displaced volume. The displaced volume (V_d) ranges from 3.8 to 12.7 cm^3 and the operating frequency (f) is 0.5, 0.7 and 0.8 Hz. The use of a lower frequency (0.5 Hz) was motivated by pressure drop constraints, especially regarding the long 8-layer bed. The rejection temperature (T_H) is varied in a range from 284 to 312 K. All the beds are tested for zero applied-load conditions to characterize the maximum temperature span for a given set of operating conditions. The 3-layer bed is also tested with an applied load of 10, 15 and 20 W. Table 7 summarizes the operating conditions for each regenerator.

Table 7 Operating conditions of each regenerator.

Parameter	**3-layer**	**6-layer**	**8-layer**		
			short	**med**	**long**
T_H [K]	293-300	284-305	302-310	302-312	304-311
V_d [cm^3]	10.4	3.8, 6.3, 7.0	5.1, 6.3, 7.0	7.6, 8.9	10.1, 11.4, 12.7
f [Hz]	0.5, 0.8	0.8	0.8	0.8	0.5-0.7
Load [W]	0, 10, 15, 20	0	0	0	0

5.3.2.1 Three-layers bed

Fig. 32(a) presents the 3-layer bed, zero-load temperature span as a function of warm rejection temperature for f = 0.8 Hz and V_d = 10.4 cm^3. A peak temperature span of 14.4 K at T_H ~ 298 K is found. Fig. 32(b) shows the temperature span as a function of the net cooling capacity for V_d = 10.4 cm^3 and two different operating frequencies with T_H = 298.4 K. The maximum zero-load span is obtained slightly above 298 K, which is near the peak ΔT_{ad} for layer 1 for the conditions shown in Fig. 31. The zero-span cooling capacity is ~20 W for a frequency of 0.5 Hz.

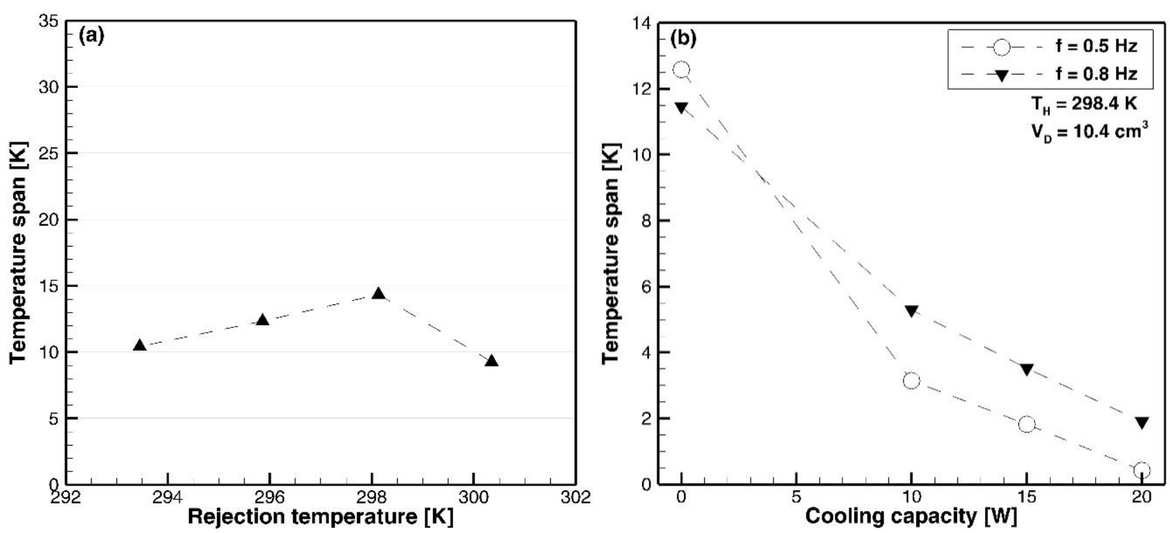

Fig. 32 Three-layer results. (a) No-load temperature span as a function of the rejection temperature for f = 0.8 Hz and Vd = 10.4 cm3; (b) Temperature span as a function of the cooling capacity for Vd = 10.4 cm3, TH = 298.4 K, and f = 0.5 Hz and 0.8 Hz.

5.3.2.2 Six-layers bed

Fig. 33 presents the results of the 6-layer bed for the zero-load temperature span as a function of the rejection temperature for f = 0.8 Hz and three different displaced volumes. The lowest displaced volume presented a peak span of 14.6 K. As the displaced volume (or utilization) increases, the peak span increases; however, continued increase in utilization leads to a lower decreased span. This behaviour is consistent with AMR theory that indicates a trade-off between transport losses and thermal capacity ratio of the fluid and solid [109,111]. A maximum temperature span of 20.4 K and 18.4 K are found for 6.33 cm^3 and 6.95 cm^3, respectively. All the peak values are at T_H ~ 299 K.

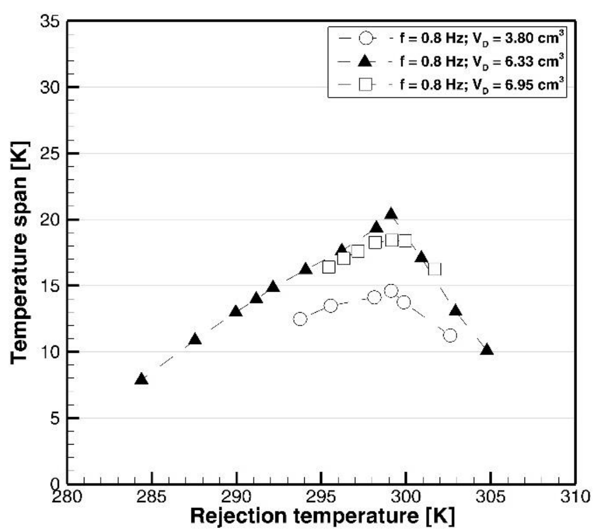

Fig. 33 Six-layer zero-load temperature span as a function of the rejection temperature for f = 0.8 Hz, and Vd = 3.80 cm^3, 6.33 cm^3, and 6.95 cm^3.

5.3.2.3 Eight-layers bed

Fig. 34 show the results for zero-load temperature span as a function of the rejection temperature for the 8-layer beds. Fig. 34(a) is for the short bed where f = 0.8 Hz and three different displaced volumes are used; Fig. 34(b) is for the medium length bed operated at f = 0.8 Hz and two different displaced volumes; Fig. 34(c) shows the long bed with for two different operating frequencies and three displaced volumes. The operating frequency for the long bed is reduced due to pressure drop constraints.

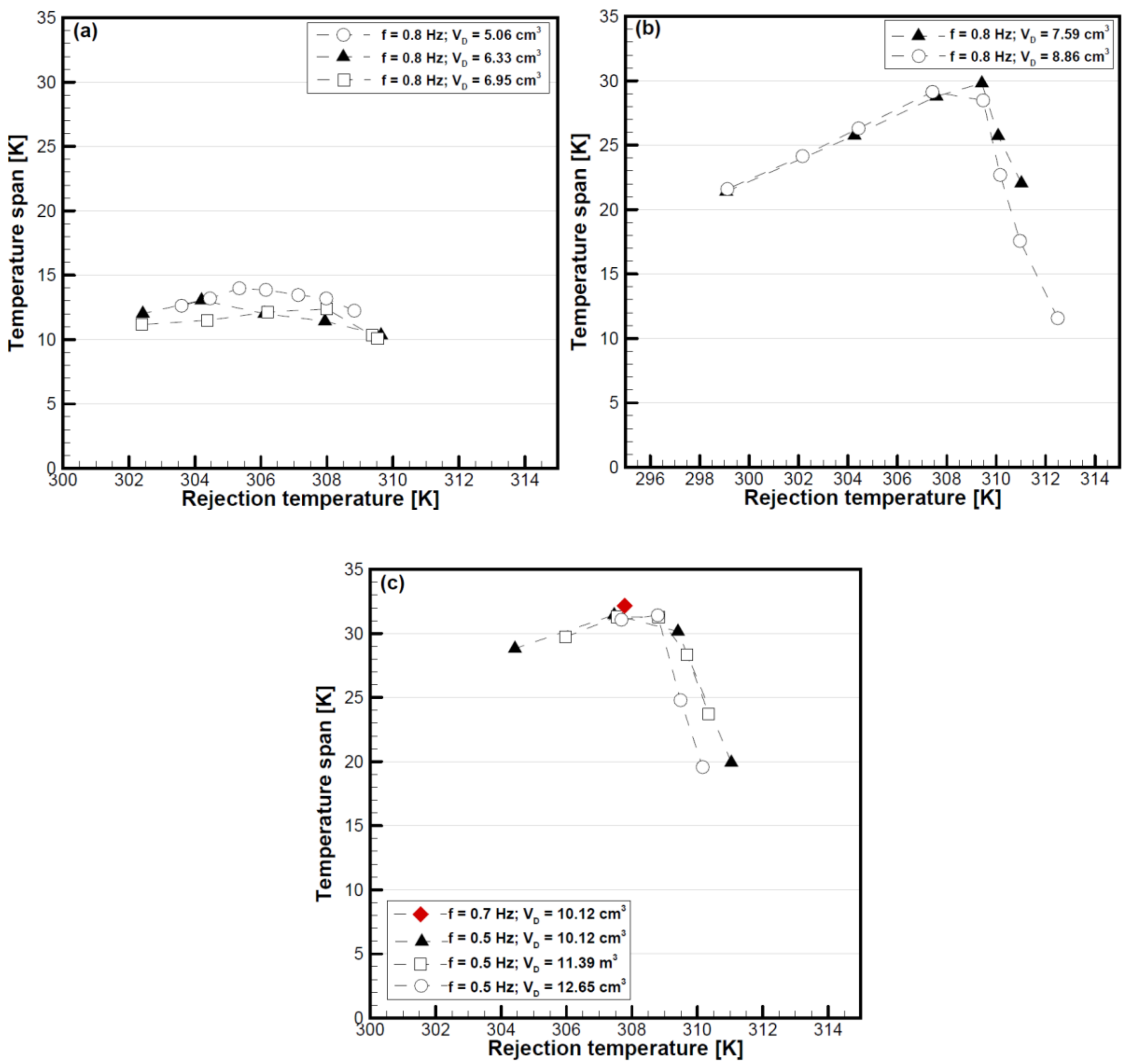

Fig. 34 Zero-load temperature span as a function of the rejection temperature for: (a) short bed - f = 0.8 Hz, and Vd = 5.06 cm3, 6.33 cm3, and 6.95 cm3; (b) medium bed - f = 0.8 Hz, and Vd = 7.59 cm3, and 8.86 cm3; (c) long bed - f = 0.5 and 0.7 Hz, and Vd = 10.12 cm^3, 11.39 cm^3, and 12.65 cm^3.

The results for the short bed (Fig. 34(a)) show varying sensitivity to displaced volume. Generally, the lowest displaced volume results in the largest zero-load span; however, the impact of increasing displaced volume is temperature dependent. A maximum span of 14.0 K at T_H ~

305 K is found. Increasing the bed length more than doubles the maximum span: T_{span} = 29.8 K at T_H ~ 309.5 K is found for the medium bed and T_{span} = 32.0 K at T_H ~ 308.5 K is found for the longest bed. As reported by Arnold et al (2014) [22], a zero-load temperature span of ~32 K is similar to experimental results for a Gd bed characterized in the same apparatus (PM II) under similar operating conditions. As compared to the 6-layer bed, the rejection temperature where the maximum temperature span is observed increases for the 8-layer beds. This is because the two new layers have a higher Tc when compared with the warmest layer of the 6-layer bed, thereby increasing the temperature range of magnetocaloric activity.

5.3.3 Discussion

Fig. 35-Fig. 37 (a-c) present the average hot (■) and cold (●) side temperatures as a function of rejection temperature for all the layered beds. The black bar between the hot and cold points represents the regenerator operating range. In these plots the active temperature range of each layer is also presented. The active temperature range is defined here as the full-width, half-maximum (FWHM) temperature range of the ΔT_{ad} curves in Fig. 31. Given the importance of adiabatic temperature change in AMR cycles, the active range of a layer and the spacing between the active ranges of each layer are expected to influence the regenerator performance. It is important to notice that some properties of the MCM such as thermal conductivity, density and specific heat can vary between different compound layers, which may affect the heat transfer properties of each layer [110,126]. However, these effects are not considered further in the present work due to lack of data.

Fig. 35 shows the data for the 3-layer bed where the maximum span (14.4 K) is found at T_H ~ 298 K. While this maximum span is small compared with the 6 and 8-layer regenerators, it appears that all three layers are active. However, if one compares the regenerator operating range and the active range, the results suggest that the layering is not well distributed. The achieved span appears to be limited because the cold end temperature (●) is far from the active range of layer 3, where the ΔT_{ad} is much smaller than that found in the range of the FWHM ΔT_{ad}. Based on this reasoning, we would expect additional layers on the cold side would increase potential cooling power and span. Another factor which may be limiting the performance at higher rejection temperatures is the spacing between layers 1 and 2. Based on their active ranges, it is apparent that there is a discontinuity between the layers. When considering the layered AMR as a cascade of sub-cycles, gaps between active regions may limit the transport of heat at interfaces between materials.

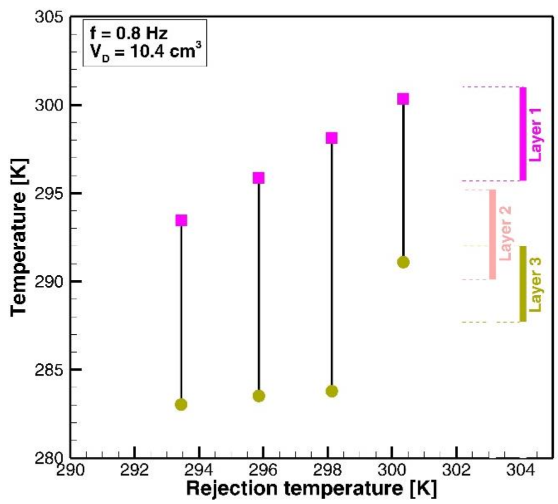

Fig. 35 Regenerator operating temperature range as a function of the rejection temperature for the 3-layer regenerators at a fixed operating condition.

Adding three additional layers with lower transition temperatures, and increasing the bed length, results in a performance improvement. For the 6-layer bed, the maximum temperature span is 20.4 K at T_H ~ 299 K and V_D = 6.33 cm^3. Due to deviations in material properties, the 6-layer bed has a better overlap in active range for the three wamer layers as compared to the 3-layer bed. We also see continuity in the active range of the three coldest layers; however, there is a noticeable gap between layers 3 and 4. Combined, these variations make it difficult to fully explain differences in performance between the 3-layer and 6-layer beds. A fraction of the active range is engaged when the displaced volume is V_D = 3.80 cm^3, but increases significantly when it is increased to 6.3 cm^3. Increasing utilization overcomes heat leaks which can reduce performance at low displaced volumes [22,47,109,111].

Fig. 37 summarizes the measured temperature spans for the 8-layer regenerators. The results for the short regenerator are shown in row (a), the medium length case is in row (b), and the long regenerator is in row (c). For these regenerators, the active range of layers tends to overlap except for layers 5, 6, and 7. The maximum temperature span of the shortest bed (Fig. 37(a)) is less than the 3-layer bed; however, in general, the spans are of similar magnitude. It is important to note that both beds have approximately the same length (~40 mm) but different layer thickness (Table 6.) Thus, comparison between the 3-layer (14 mm/layer) and the short 8-layer (5 mm/layer) beds suggest that the layer thickness is an important constraint when designing an AMR matrix.

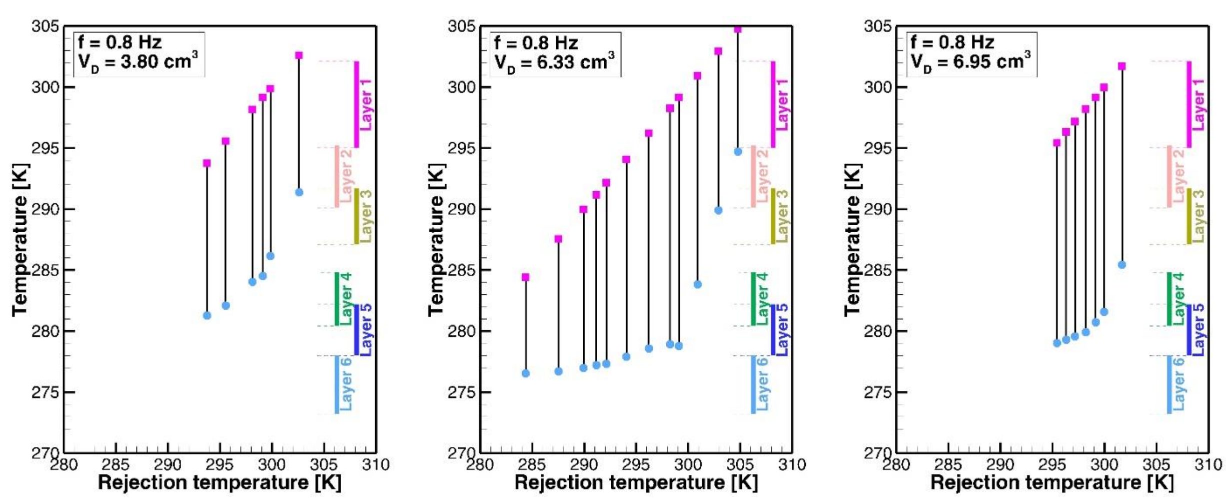

Fig. 36 Six-layer operating temperature range as a function of the rejection temperature for f = 0.8 Hz, and Vd = 3.80 cm^3, 6.33 cm^3, and 6.95 cm^3.

Fig. 37(b) and (c) show the benefit of increasing regenerator mass. Both the 10 mm/layer and 15 mm/layer beds show a significant increase in temperature span compared with the short bed.

And, for the largest spans with T_H ~ 308-309 K, all layers are active. The differences in maximum span between the medium and long bed are small, suggesting that optimum layer thickness is related to the number of layers, the regenerator thermal effectiveness, and pressure drop. A longer bed with a larger thermal mass results in a higher thermal effectiveness which can enable larger temperature span, but efficiency is reduced due to larger pressure drop [127]. Because of pressure drop constraints, the longer matrix is operated at a lower frequency than the medium length regenerator. Lower frequency tends to reduce net cooling capacity, but longer length and increased heat transfer between the solid and the fluid can counteract this and, as result, lead to little difference between the medium and long beds [127].

As seen in Fig. 34, the medium and long beds (Fig. 34 (b) and (c) respectively) are sensitive to the rejection temperature, showing an abrupt reduction in span for temperatures greater than the peak. This is not the case of the shorter bed (Fig. 34 (a)) which has a lower temperature span but is less sensitive to the rejection temperature. This behaviour can be explained by the operating temperatures and the activation of the layers with varying temperature. In Fig. 34(b) and (c) the temperature span is seen to decrease rapidly as the rejection temperature is moved above the active range of the warmest layer. The shorter matrix never operates in a condition where all the layers are activated, and the rejection temperatures are never increased above the active range of the warmest layer. As a result, although the rejection temperature is varied, the coldest layers of the short regenerator tend to remain in a passive condition while the warm side remains active, making the temperature span less sensitive to the rejection temperature. This behaviour is consistent with the sensitivity for FOM materials described in [124].

Some final observations are possible when considering the performance of all of the AMRs presented in Fig. 35-Fig. 37. Below the rejection temperature where the peak span is found, the cold-side temperatures show little sensitivity to the rejection temperature. The total heat load is a function of applied load and any leaks. Thus, for the zero-load cases, the heat load is due to parasitic leaks, which are a function of the cold-side temperature. As T_H increases, the cold side temperatures show little change and, in some cases, remain constant. We can infer that for these cases, the total cooling power produced by the AMR is constant, yet, the operating span varies which indicates more than one stable operating condition is possible for the same cooling power.

After the peak T_H, where there can be a rapid decrease in temperature span, the cold-side temperature is observed to collapse with incremental changes corresponding to the differences between the active ranges of the layers. For example, see Fig. 37(b) and (c) for T_H ~309 - 311 K.

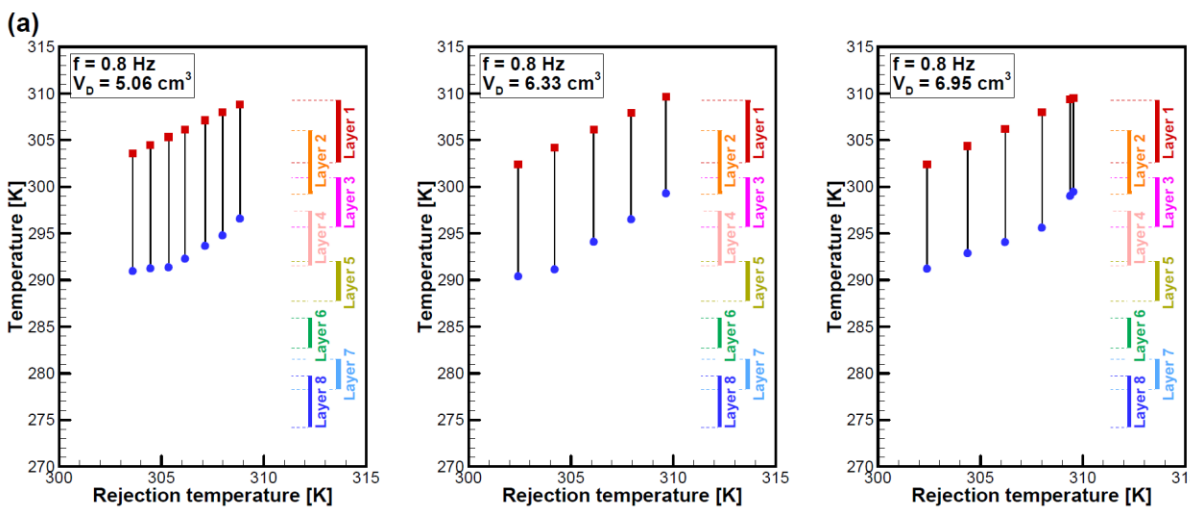

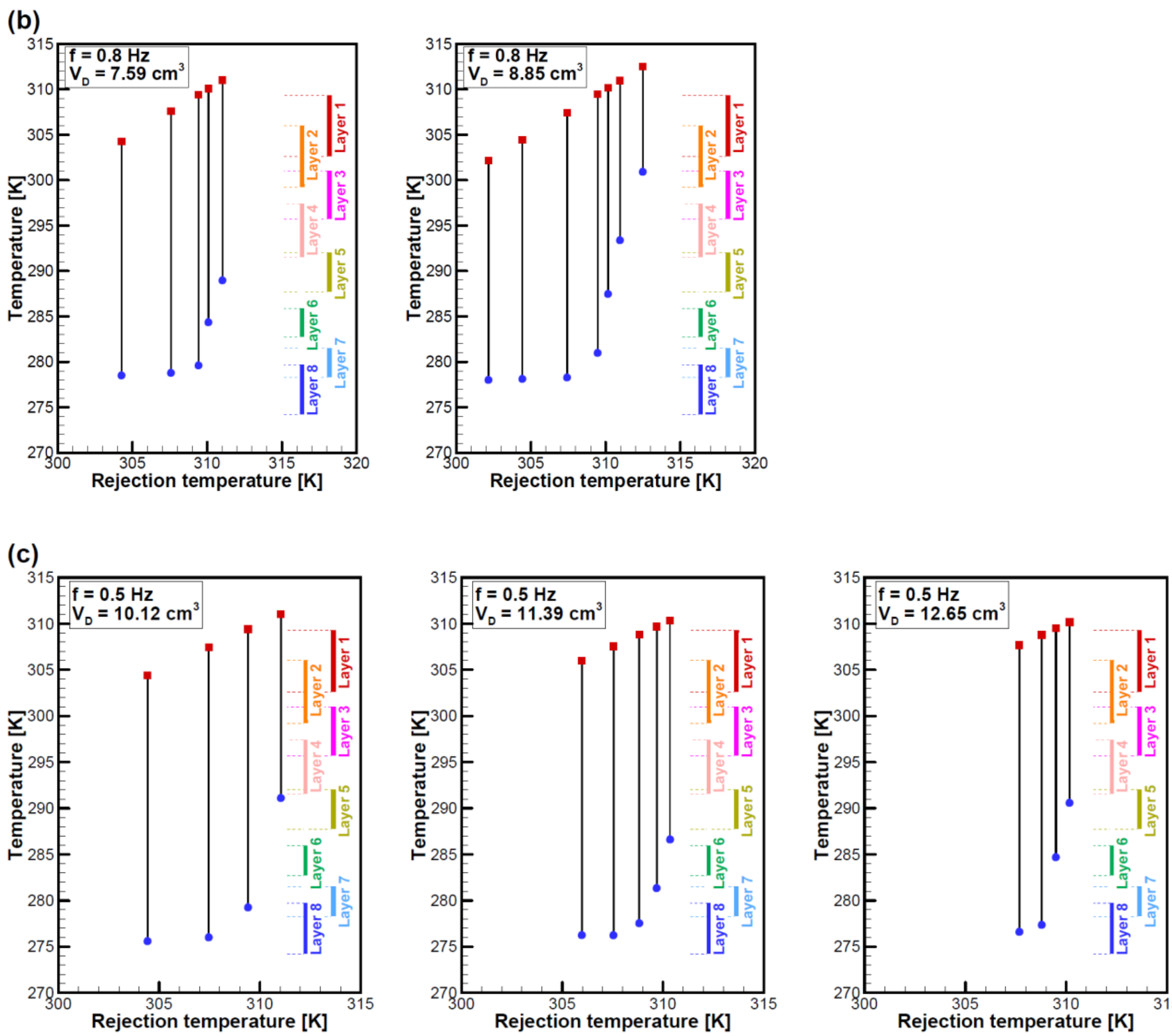

Fig. 37:8-layer results for operating temperature range as a function of rejection temperature for: (a) short bed - f = 0.8 Hz, and Vd = 5.06 cm3, 6.33 cm^3, and 6.95 cm^3; (b) medium bed - f = 0.8 Hz, and Vd = 7.59 cm^3, and 8.86 cm^3; (c) long bed - f = 0.5 Hz a nd V_d = 10.12 cm^3, 11.39 cm^3, and 12.65 cm^3.

5.3.4 Summary

Regenerators composed of $MnFeP_{1-X}As_X$ were experimentally characterized in the PM II device. Performance in terms of no-load temperature span as a function of hot rejection temperature is measured. Results for AMRs composed of three, six and eight layers of $MnFeP_{1-X}As_X$ alloy are presented. A sensitivity analysis is performed with respect to layer thickness and number of layers. Test results confirm the ability of $MnFeP_{1-X}As_X$ to create layered regenerator structures. For the given T_{Curie} separation in the regenerators and set of operating conditions, five millimeter layers are insufficient to produce the necessary three to five degree Kelvin span to allow the cascade to function, while ten millimeter layers are sufficiently long to allow for proper cascade function. The following chapter describes numerical modeling of a single layer FOM AMR where magnetic hysteresis is included.

Chapter 6 Hysteresis model validation

The impacts of material hysteresis on AMR performance are explained using the model described in Chapter 4. The model is validated with no-load and load experimental data for the Gd-based AMR and later compared with experimental data for $MnFeP_{1-x}Si_x$-based AMR. To better understand the hysteresis effects, different scenarios regarding magnetocaloric properties are simulated.

6.1 $MnFeP_{1-x}Si_x$ material properties

Fig. 38 presents the ΔT_{ad} directly measured, for 0-1.1 T magnetic field change, for the $MnFeP_{1-x}Si_x$ alloy tested in Section 5.1. The bespoke device used to characterize the ΔT_{ad} is described by Christiaanse et al [79]. In order to study the irreversibilities associated with this FOM material, *heating* (increasing the rejection temperature) and *cooling* (reducing the rejection temperature) measurements are performed. The solid black line shows a fit curve using a Lorentzian model of specific heat [124].

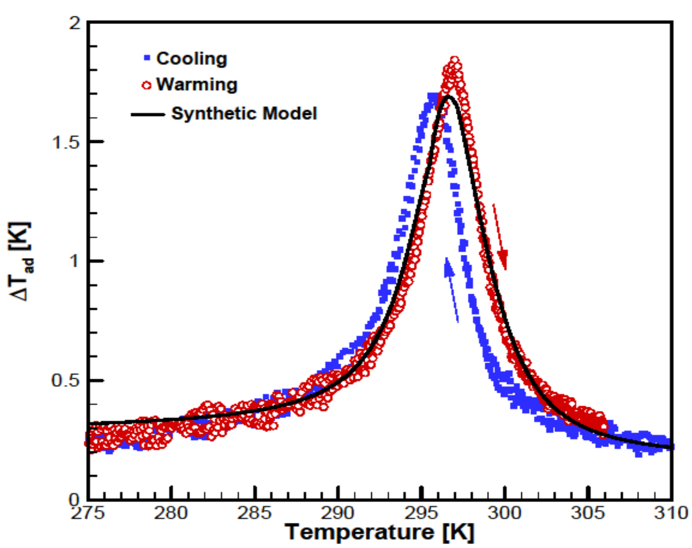

Fig. 38 Direct measured adiabatic temperature change as a function of the temperature, for the $MnFeP_{1-x}Si_x$ AMR are performed for heating and cooling protocols with properties magnetic field variation of 1.1 T.

For numerical simulations, material properties are modeled using the approach described in Niknia et al [124] where specific heat is approximated with an asymmetric Lorentzian curve, and the transition shift due to field is determined by the difference in temperature between the peak specific heats. Integration of specific heat provides entropy curves which are interpolated for ΔT and ΔS_m. The predicted ΔT for an isentropic 0-1.1 T field change is shown by the solid line in Fig. 38 labeled *synthetic model.* The model uses the rectified sinusoidal magnetic field profile for the PM I device [25]. Fig. 39 shows modeled ΔT_{ad} and specific heat using the synthetic model and the fields for PM I.

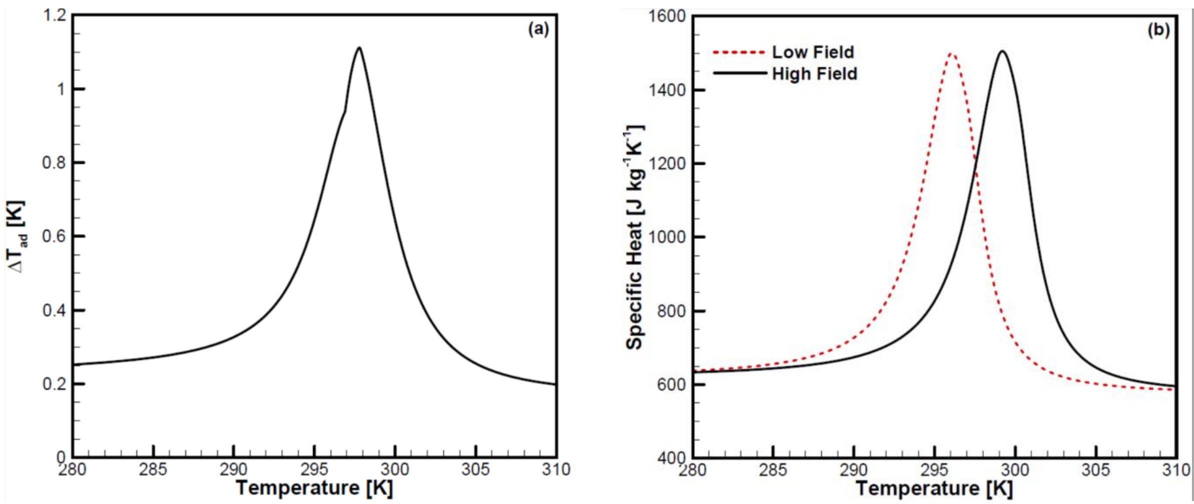

Fig. 39 Simulated a) adiabatic temperature change, b) specific heat of the $MnFeP_{1-x}Si_x$ samples for magnetic field variation of 1.1 T.

6.2 Results

This section compares the experimental and numerical results. Firstly, since Gd is the reference material for magnetic refrigeration, its results are used to validate the model. After the validation the experimental data for $MnFeP_{1-x}Si_x$ FOM are compared with the simulation data considering three different physics: (i) heat leaks; (ii) MCE implementation; and (iii) magnetic hysteresis. Heat leaks account for thermal imperfections of the apparatus. MCE implementation represents the method of determining entropy and temperature changes as shown in Fig. 16.

Cases considering magnetic hysteresis include the entropy generation due to irreversible magnetization, Eqn. 14. Table 8 summarizes all the four simulated cases.

Table 8 Description of the three different cases used to simulate the $MnFeP_{1-x}Si_x$ FOM beds. Y indicates the inclusion of en effect (or not,N).

Properties	Case 1	Case 2	Case 3
Heat leak	Y/N	Y	Y
MCE implementation	HC	HC/Av	HC
Magnetic hysteresis	N	N	Y/N

In Table 8, Y and N stand for yes and no, while *HC* and *Av* stand for *Heating-Cooling* and *Average* MCE implementation. *HC* assumes the state change due to field and temperature is given by the difference between the low field heating and high field cooling data. *Av* uses the average of *heating* and *cooling* isofield data to determine state change.

For all the simulations, the transition temperature (T_{Curie}) for $MnFeP_{1-x}Si_x$ is 295.5 K, the thermal hysteresis for specific heat (ΔT_{hys}) is 1 K, and the specific heat peak ($C_{H,peak}$) is 1800 J/kgK.

6.3 Gd results

The simulated performance curves temperature span as a function of the hot side temperature for different heat inputs for Gd are shown in Fig. 40.The symbols show experimental data while the lines are simulations. Fig. 40(a) is for 1 Hz, 5.09 cm^3 displaced volume and zero applied load (0 W), while Fig. 40 (b) is for 2 Hz, 3.92 cm^3 displaced volume and two heat inputs: 0 W and 10 W. The effects of device heat leaks are included. One can see from the results that the model provides a good representation of experiments for Gd.

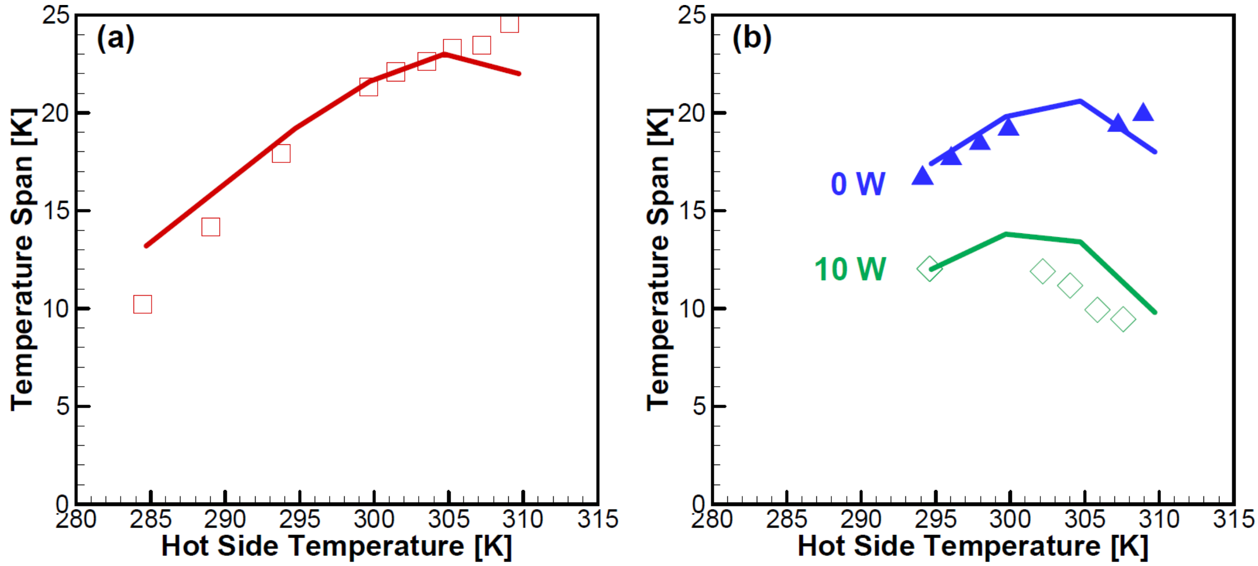

Fig. 40 Comparison between experimental (symbols) and numerical (line) results for Gd-based AMR: (a) f =1 Hz, V_D = 5.09 cm^3 and no-load condition (0 W); (b) f =2 Hz, V_D = 3.92cm^3 and 0 W and 10 W load condition.

6.4 $MnFeP_{1-x}Si_x$ FOM results

6.4.1 Case 1: Effect of heat leaks

Case 1 compares simulation results for the $MnFeP_{1-x}Si_x$ AMR with (Y) and without (N) heat leaks to experimental results (Table 8). In this case, magnetic hysteresis is not included in the model and the *HC* MCE implementation is used. Fig. 41 compares simulated temperature spans to experimental measurements under no-load conditions (Fig. 41(a)); 5 W load condition (Fig. 41 (b)); and 10 W load condition (Fig. 41(c)). Again, symbols represent experimental data and the lines are simulation results: solid lines are with heat leaks (Yes) and dashed lines are without heat leaks (No).

The model predictions follow the same general trend as the experimental data. For 0 W condition (Fig. 41(a)), differences between simulations and measurements are more pronounced at higher T_H values after the peak point where the temperature span for the simulation results are lower than experimental data. General trends are in accordance with the experiments, especially at lower T_H. The differences between simulations with and without heat leaks are small, which can be partially explained by the small temperature spans and operation near room temperature; both factors reduce the effects of unwanted heat interactions.

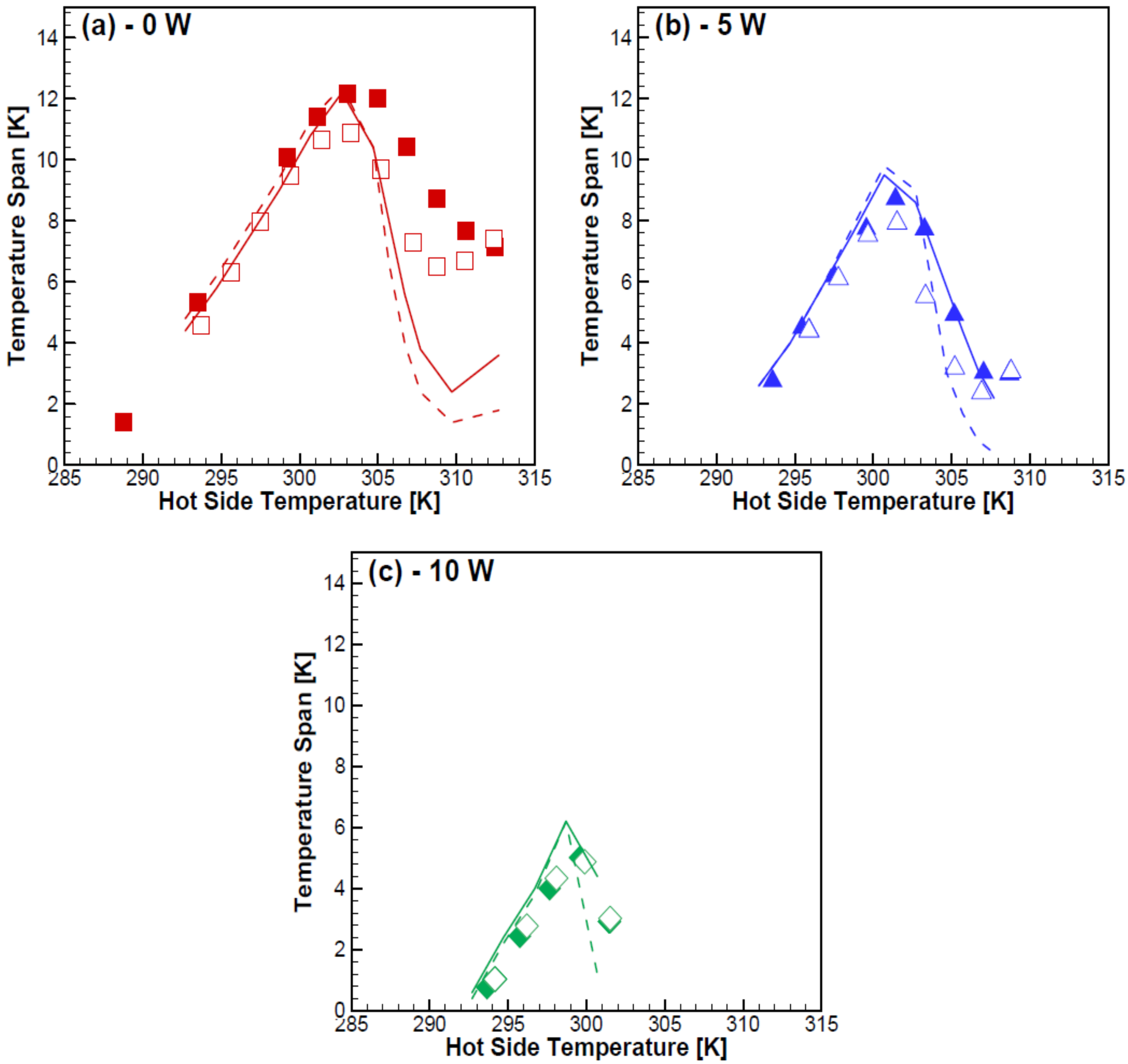

Fig. 41 Comparison between experimental (symbols) and numerical (line) results for $MnFeP_{1-x}Si_x$ FOM. The solid line stands for with heat leaks and the dashed lines without heat leaks. Different loads conditions are used: (a) no-load condition (0 W); (b) 5 W; (c) 10 W.

6.4.2 Case 2: MCE implementation

Case 2 compares the impacts of MCE implementation method: *Heating-Cooling* (*HC*) and Average (*Av*) as in Fig. 16 and Table 8. For these simulations, heat leaks are considered and no magnetic hysteresis implemented. As in the previous section, Fig. 42 (a) is for 0 W; Fig. 42(b) for 5 W, and Fig. 42 (c) for 10 W load condition. Again, symbols stands for the experimental and the lines to simulation results: solid line is *heating-cooling* (*HC*) and dashed line is the average implementation (*Av*).

The general trends presented in Fig. 42 show that the average implementation of MCE tends to result in larger T_{span} of the system. The *Av* implementations for MCE results in a larger ΔT_{ad} than the *HC* approach, reflecting the larger spans predicted by simulations.

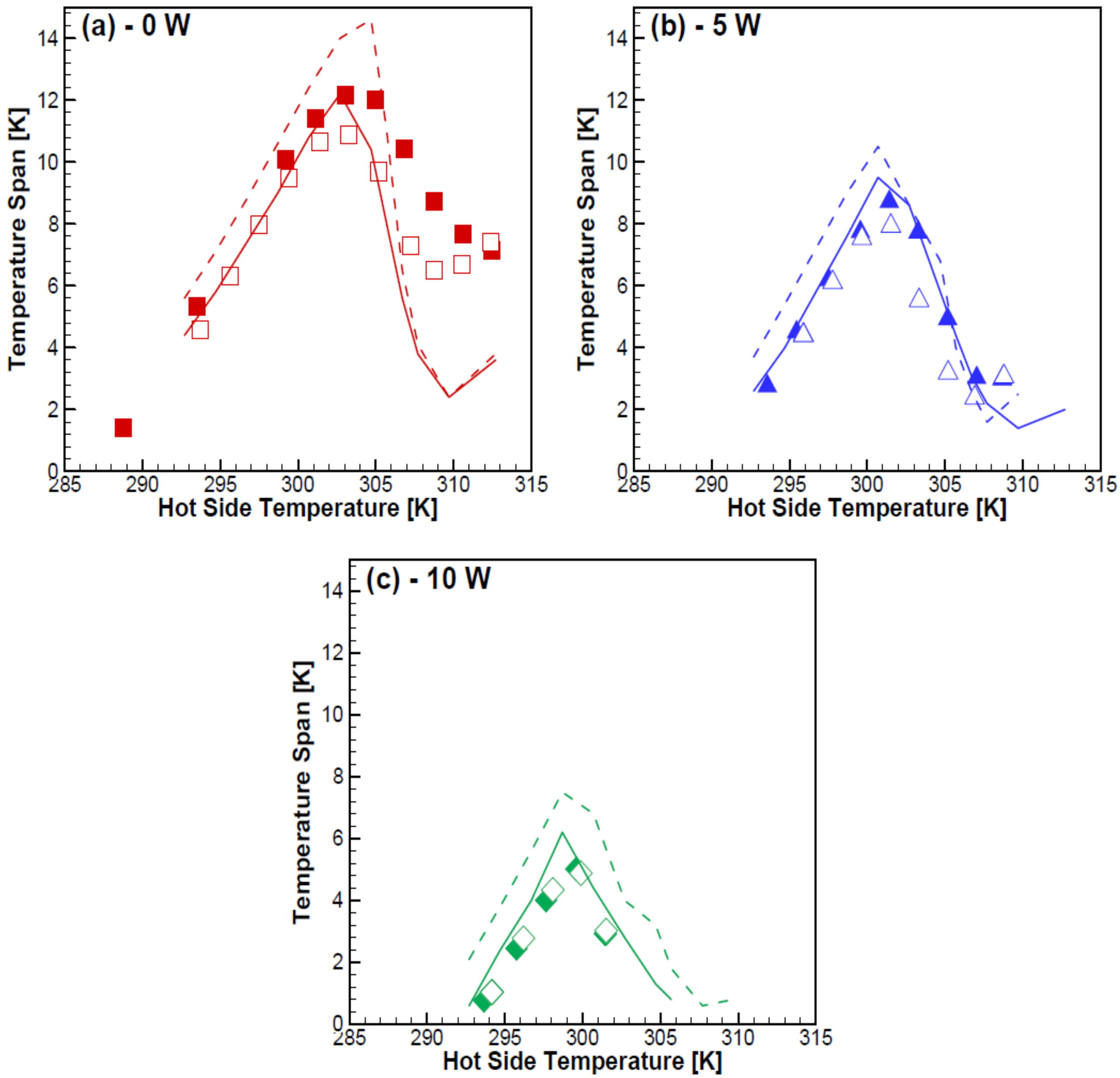

Fig. 42 Comparison between experimental (symbols) and numerical (line) results for $MnFeP_{1-x}Si_x$ FOM. The solid line stands for heating-cooling MCE implementation, and the dashed for the average implementation. Different loads conditions are used: (a) no-load condition (0 W); (b) 5 W; (c) 10 W.

6.4.3 Case 3: Magnetic hysteresis

Case 3 compares the results considering simulations with (Y) and without (N) magnetic hysteresis (Table 8). System heat leaks are included and the heating-cooling (*HC*) implementation for state is used. Fig. 43 shows result in separate plots for 0 W (a), 5 W (b), and 10 W (c). Solid lines are simulation results with magnetic hysteresis, and dashed lines are without magnetic hysteresis.

As can be seen, the AMR temperature span is not significantly impacted by including entropy generation due to magnetic hysteresis. Generally good agreement between experiments and simulations are achieved with or without the magnetic hysteresis term. Any differences between simulations are similar to the uncertainty in the measured data (represented by the size of the markers.)

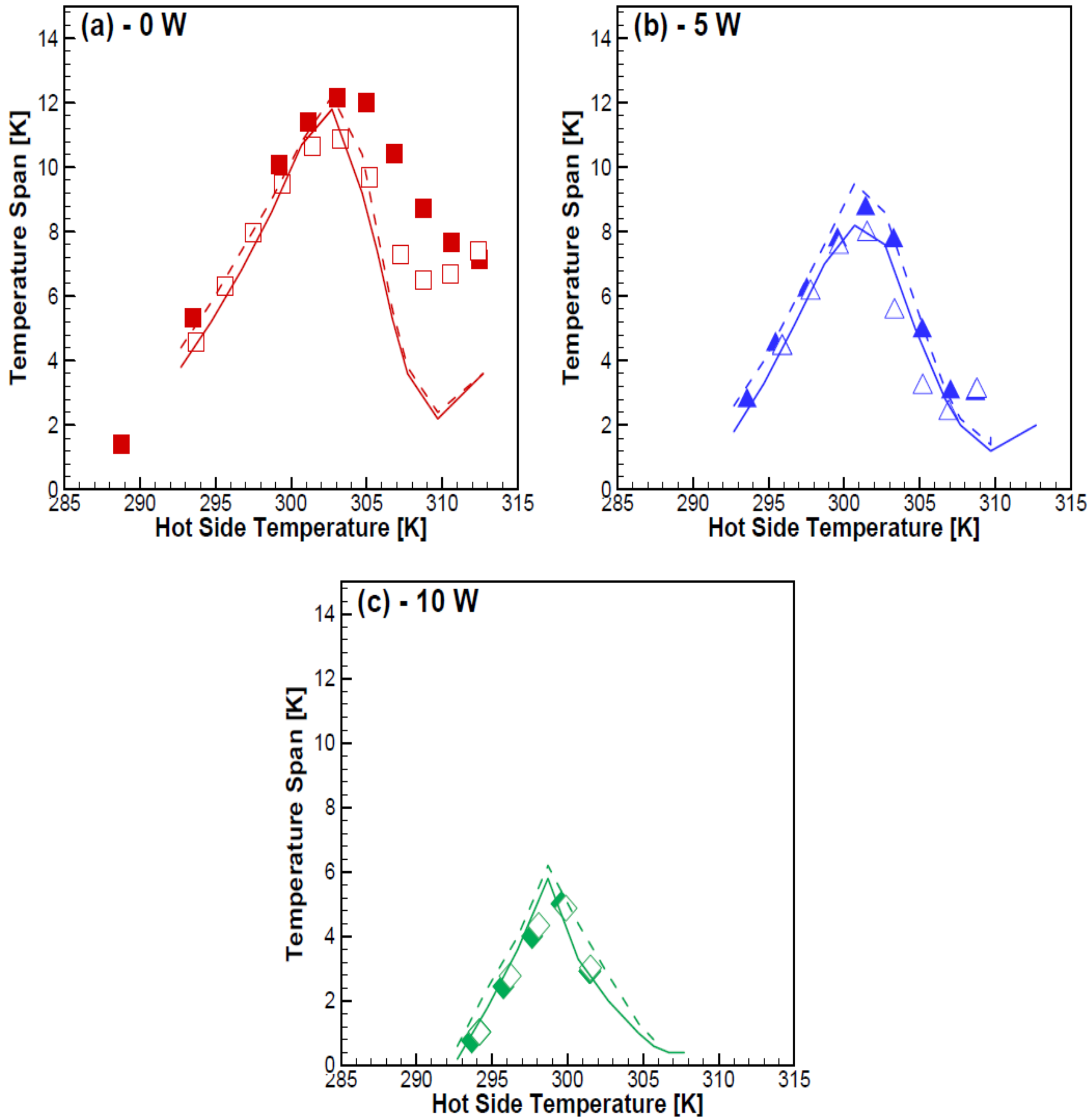

Fig. 43 Comparison between experimental (symbols) and numerical (line) results for MnFeP1-xSix FOM. The solid lines stands for simulations with magnetic hysteresis, and the dashed for simulations without magnetic hysteresis. Different loads conditions are used: (a) no-load condition (0 W); (b) 5 W; (c) 10 W.

6.5 Discussion

The results for Gd and Case 1 for $MnFeP_{1-x}Si_x$ FOM (Fig. 40 and Fig. 41) show the accuracy of the model, especially when the heat leaks are included, as already proposed in previous works [107,109,111]. As expected, heat leaks are more pronounced at higher temperature spans. From these results one can conclude that the model is well reliable and can be used to explore other physical aspects of the MCE implementation and hysteresis.

When comparing the MCE implementation, Case 2 in Fig. 42, for all cases of any heat input condition, better accuracy is found when the MCE is implemented following the *heating-cooling* procedure (see Fig. 16). This implementation means the impact of thermal hysteresis on the AMR performance is captured by the measured ΔT_{ad} data. This was previously observed by Refs. [76,79,128], which observed a better reproduction of the experimental ΔT_{ad} when compared with the calculated low-field heating and high-field cooling MCE of a MCM with thermal hysteresis. Therefore, the results in Fig. 42 corroborate, those authors observation, and demonstrate how thermal hysteresis impacts on an AMR performance in term as of cooling capacity and temperature span.

For Case 3, Fig. 43 presents how the magnetic hysteresis impacts the AMR. As one can see, its impacts, at least for $MnFeP_{1-x}Si_x$ FOM are not as significant as the impacts of thermal hysteresis in Case 2. The magnetic hysteresis slightly reduces the temperature span to all different operating conditions experienced in PM I device. This suggests that the magnetic hysteresis is more important in terms of the material nature than to AMR cooling power.

6.6 Summary

Hystersis predictions from the model were compared to experimental results from two differerant single layer SOM and FOM materials and show good agreement across a wide range of operating parameters. Model results indicate that magnetic hystersis does not significantly effect predicted temperature span and cooling power. It appears that the hystersis effects are captured in the measured ΔT_{ad} data and are sufficient for modeling. Magnetic hysteresis may be important for accurately predicting efficiency, but this is not considered here. The following chapter summarizes the thesis, the main findings and provides recommendations for future work.

Chapter 7 Conclusions

$MnFeP_{1-x}Si_x$ and $MnFeP_{1-x}As_x$ FOM materials with a large MCE have the adverse property of exhibiting hysteresis, which introduces a series of challenges. While FOM materials present some desirable characteristics from the application perspective, the issue of hysteresis and its impacts on AMR performance is one of the critical challenges for the development of the magnetic cooling technology. This thesis provides new information enhancing our understanding of the coupled processes occurring within the AMR. Applying these findings with further analysis will determing the optimal conditions and configurations needed to meet specified cost and performance targets.

7.1 Thermal hysteresis : Single layer Gadolinium and $MnFeP_{1-x}Si_x$

In the present study two different AMR beds are experimentally characterized in the PM I. One test uses regenerators composed of Gd and the second experiments use $MnFeP_{1-x}Si_x$ FOM. The tests are carried out using a fixed displaced volume and frequency, but at different rejection temperatures. Two different process are considered: a *heating* process, where the rejection temperature is increased after steady-state is reached, and a *cooling* process using the reverse protocol. As expected, the Gd bed produced a single temperature span curve as a function of T_H. The $MnFeP_{1-x}Si_x$ AMR, on the other hand, presented two different *heating* and *cooling* performance curves, in which major differences in temperature span are observed when the material is operating above its transition temperature. As a conclusion, the FOM AMRs presented, depending on the T_H range, show that the *cooling* curves underperform the *heating* process. The maximum difference in temperature span was at 0 W and T_H ~ 307 K, where the

T_{span} for the *heating* curve is about 3.5 K higher than the span for the *cooling* curve. One of the possible causes of such a difference are related to the presence of multiple points of equilibrium.

Niknia et al (2018) [123] recently presented the first analysis of MPE in AMRs using an FOM. It is numerically observed that for certain operating conditions, MPE can exist and, as a result, two or more temperature spans can be obtained for the same hot side temperature which is consistent with our experimental findings. Until now, the phenomena of MPEs have not been discussed in the literature. Combined, hysteresis and MPE are two significant features which can impact AMRs composed of FOMs. These results were published in the Journal Applied Physics [123].

7.2 Thermal hystersis : Three multilayer $MnFeP_{1-x}As_x$ FOM regenerators

Layered AMRs composed of materials from the $MnFeP_{1-x}As_x$ family are experimentally characterized for temperature span and cooling power as a function of rejection temperature T_H. Three regenerator configurations are investigated using four different alloys. Two different alloys are used as a cold layer and warm layer in all cases while two other alloys are used as an intermediate layer. The three regenerators are defined by no intermediate layer, an intermediate layer with low ΔT_{ad}, and an intermediate layer with high ΔT_{ad}. Regenerator volumes are fixed for all cases where the layers make up approximately equal fractions. The use of an intermediate layer has a small impact on maximum temperature span; however, performance in terms of exeregetic power increases by approximately 200%. MPE are identified using *heating* and *cooling* experiments. Unlike the finding of Niknia et al. (2018) [123] for a single layer regenerator using first order material, MPEs persist at high applied loads (or small temperature spans). MPE and hysteresis warrant further systematic experimental and numerical study. These results are in review in the Journal Applied Physics [129].

7.3 $MnFeP_{1-x}As_x$ multilayer active magnetic regenerators

The impact of layering on FOM based AMR performance using $MnFeP_{1-X}As_X$ was experimentally investigated for different layer compositions and sizes. The results confirm the ability of $MnFeP_{1-x}As_x$-based multilayer AMR to produce spans much greater than the FWHM of an individual material. A trade-off between the number of layers and the layer thickness is found. The performance in terms of temperature span is dependent upon the appropriate spread between layer properties so that the active range of the composite structure is matched with the active range of individual layers. Increasing the number of layers (reducing the thickness per layer), may lead to a mismatch in the regenerator operating temperature range and the active temperature range of constituent alloys, as is found with an 8-layer regenerator made up of 5 mm per layer. In this case, the mass of material is insufficient to allow the cascade to function across all layers. However, longer 8-layer regenerators enable all layers to be active. Finally, a maximum temperature span of 32 K at a rejection temperature of 308 K is measured with an 8-layer regenerator. This result is similar to a Gd single bed [22] and to a Gd-GdY double layer AMR [47] experimentally characterized in the same apparatus (PM II) under similar operating conditions. These results were published in Journal Physics D: Applied Physics [130].

7.4 Predicting the thermal hysteresis behavior for single-layer $MnFeP_{1-x}Si_x$ AMR

First order magnetocaloric materials are of interest for the creation of heat pumps and refrigerators using active magnetic cycles. These materials tend to have narrow transitions and magnetic and thermal hysteresis. This leads to complexity and modeling challenges for AMR designers. A 1D AMR model accounting for thermal and magnetic hysteresis to simulate AMR performances of SOM and FOM materials needed for the design of magnetic devices is described. The proposed hysteresis model is validated against measured temperature span data for a Gd and material from the $MnFeP_{1-x}Si_x$ family. Simulated results show good agreement with experimental data. Effects of hysteresis and the implementation of material data in the model are captured, and results shown to reduce AMR performance. Further simplifications to the model are possible to simulate multilayer AMRs and are an area for further study.

7.5 Recommendations and future work

From the application perspective, FOMs can be potential candidates for the development and commercialization of magnetic heat pumps. Nonetheless, magnetic and thermal hysteresis and their impacts on AMR performance still require a better understanding. The following future research is recommended.

- The hysteresis impacts on the AMR performance presented in this thesis is of such importance from the point of view of a future application. Additional, systematic, multilayer FOM performance studies are needed to improve AMR devices and to understand the limitations of hysteresis on material suitability.
- The existence of MPEs may be due to both material hysteresis and the sharp transitions seen with FOMs. In practice, MPEs may lead to problems for FOM-based AMR heat pumps where a smaller temperature span may arise depending on the operating history of the system. In multilayered regenerators one of the materials may be limited in span due to an unfavorable thermal equilibrium and thereby limits the performance of the entire cascade. Further study is needed to clarify the impacts of material properties, layering strategies, and device characteristics on MPEs and performance.
- One of the issues with simulating hysteresis in multi-material AMRs is the computational challenge. While detailed hysteresis modeling is possible, a simplified approach is desirable so that design optimization can be performed using readily available numerical

resources. Further simplifications to the model are possible and are areas for further study.

References

[1] W. Goetzler, S. Goffri, S. Jasinski, R. Legett, H. Lisle, A. Marantan, M. Millard, D. Pinault, D. Westphalen, R. Zogg, Energy savings potential and R&D opportunities for commercial refrigeration, US Department of Energy, Energy Efficiency and Renewable Energy Building Technologies Program, 2009.

[2] N. Shah, N. Khanna, N. Karalim, W.Y. Park, Y. Qu and N. Zhou, Opportunities for simultaneous efficiency improvement and refrigerant transition in air conditioning, BerkeleyLab Report LBNL-2001021, 2017. http://escholarship.org/uc/item/2r19r76z.

[3] C. Zimm, A. Jastrab, A. Sternberg, V.K. Pecharsky, K.A. Gschneidner Jr, M. Osborne, et al., Description and performance of a near-room temperature magnetic refrigerator, Adv. Cryog. Eng. 43,1759–1766,1998. doi:10.1007/978-1-4757-9047-4_222.

[4] E. Brück, Developments in magnetocaloric refrigeration, J. Phys. D. Appl. Phys. 38, R381-R391,2005.

[5] E. Brück, O. Tegus, D.T.C. Thanh, K.H.J. Buschow, Magnetocaloric refrigeration near room temperature, J. Magn. Magn. Mater. 310, 2793-2799,2007.

[6] O. Gutfleisch, M.A. Willard, E. Brück, C.H. Chen, S.G. Sankar, J.P. Liu, Magnetic materials and devices for the 21st century: stronger, lighter, and more energy efficient, Adv. Mater 23,821-842,2011.

[7] V. Franco, J.S. Blazquez, B. Ingale, A. Conde, The magnetocaloric effect and magnetic refrigeration near room temperature: materials and models, Annu. Rev. Mater. Res. 42,305-342, 2012.

[8] D. Eriksen, K. Engelbrecht, C.R.H. Bahl, R. Bjørk, K.K. Nielsen, A.R. Insinga, N. Pryds, Design and experimental tests of a rotary active magnetic regenerator prototype, Int. J. Refrig. 58,14-21,2015.

[9] G. V. Brown, Magnetic heat pumping near room temperature, J. Appl. Phys. 47,3673–

3680,1976. doi:10.1063/1.323176.

[10] P.V. Trevizoli; T.V. Christiaanse; P. Govindappa; I. Niknia; R. Teyber; J.R. Barbosa Jr. and A. Rowe, Magnetic heat pumps: an overview of design principles and challenges, Sci. Tech. Built Environ. 22(5), 507-519,2016.

[11] A. Kitanovsky, P. Egolf, Thermodynamics of magnetic refrigeration, International Journal of Refrigeration 29(1):3–21, 2006.

[12] A. Smith, C. Bahl, R. Bjork, K. Engelbrecht, K.K. Nielsen, N. Pryds, Material challenges for high performance magnetocaloric refrigeration devices, Adv. Energy Mater. 2,1288–1318,2012.

[13] BingfengYu, Min Liu, A review of magnetic refrigerator and heat pump prototypes built before the year, International Journal of Refrigeration 33,1029-1060,2010.

[14] Ichiro Takeuchi, Karl Sandeman, Solid-state cooling with caloric materials, Physics Today 68(12), 48,2015. doi: 10.1063/PT.3.3022.

[15] P. Debye, Some observations on magnetization at a low temperature, Annalen Der Physik, 81, pp. 1154-1160, 1926.

[16] W.F. Giauque, A thermodynamic treatment of certain magnetic effects, A proposed method of producing temperatures considerably below 1° absolute, Journal of the American Chemical Society,pp. 1864-1870,1927.

[17] J.A. Barclay,The theory of an active magnetic regenerative refrigerator, in: Proceedings of the Second Biennial Conference on Refrigeration for Cryocooler Sensors and Electronic Systems, 1983, Los Alamos National Laboratory report LA-UR-82-1792, Greenbelt, MD, pp. 1-13,1982.

[18] J.A. Barclay, W.A. Steyert, Active Magnetic Regenerator, U.S. Patent 4,332,135,1982.

[19] V.K. Pecharsky, K.A. Gschneidner, Giant magnetocaloric effect in Gd_5 (Si_2Ge_2), Phys. Rev. Lett. 78, pp. 4494-4497, 1997.

[20] B. Yu, M. Liu, P. W. Egolf, A. Kitanovski, A review of magnetic refrigerator and heat pump prototypes built before the year 2010, Int. J. Refrig. 13,1029-1066,2010.

[21] A. Kitanovski, J. Tusek, U. Tomc, U. Plaznik, M. Ozbolt, A. Poredos, Magnetocaloric Energy Conversion: From Theory to Applications, Springer International Publishing, 2015.

[22] D.S. Arnold, A. Tura, A. Ruebsaat-Trott, A. Rowe, Design improvements of a permanent magnet active magnetic refrigerator, Int. J. Refrig. 37,99–105,2014. doi:10.1016/j.ijrefrig.2013.09.024.

[23] K. Engelbrecht, D. Eriksen, C.R.H. Bahl, R. Bjork, J. Geyti, J.A. Lozano, K.K.Nielsen, F.Saxild, A.Smith, N.Pryds, Experimental results for a novel rotary active magnetic regenerator. Int. J. Refrigeration 1498– 1505, 2012.

[24] P.V Trevizoli, A.T. Nakashima, G.F. Peixer, J.R. Barbosa, Performance assessment of different porous matrix geometries for active magnetic regenerators, Appl. Energy 187, 847–861. 2017.

[25] A. Tura, A. Rowe, Permanent magnet magnetic refrigerator design and experimental characterization, Int. J. Refrig. 34,628–639,2011. doi:10.1016/j.ijrefrig.2010.12.009.

[26] C.R.H. Bahl, T.F. Petersen, N. Pryds, A. Smith, T.F. Petersen, A versatile magnetic refrigeration test device, Review of Scientific Instruments 79 (9), 093906,2008.

[27] P.V. Trevizoli, Development of thermal regenerators for magnetic cooling applications, PhD Thesis, Federal University of Santa Catarina, 2015.

[28] O. Guteisch, T. Gottschall, M. Fries, D. Benke, I. Radulov, K. P. Skokov, H. Wende, M. Gruner, M. Acet, P. Entel, M. Farle, Mastering hysteresis in magnetocaloric materials, Phil. Trans. R. Soc. A 374,20150308,2016.

[29] O. Tegus, E. Bruck, K.H.J. Buschow, F.R. de Boer, Transition metal based magnetic refrigerants for room temperature applications, Nature 415,150-152, 2002.

[30] J. Tusek, A. Kitanovski, U. Tomc, C. Favero, A. Poredos, Experimental comparison of multi-layered La–Fe–Co–Si and single-layered gd active magnetic regenerators for use in a room-temperature magnetic refrigerator, Int. J. Refrig. 37,117–126,2014.

[31] K.Engelbrecht and C.R.H.Bahl, Evaluating the effect of magnetocaloric properties on magnetic refrigeration performance, J Appl Phys 108:123918, 2010.

[32] Andrej et al, Magnetocaloric Energy Conversion, Springer International Publishing, Switzerland, 2015.

[33] M.A. Richard, A. Rowe, R. Chahine, Magnetic refrigeration: single and multimaterial active magnetic regenerator experiments, J. Appl. Phys. 95, 2146–2150,2004.

[34] C. Zimm, A. Boeder, J. Chell, A. Sternberg, A. Fujita, S. Fujieda, K. Fukamichi, Design and performance of a permanent-magnet rotary refrigerator, Int. J. Refrig. 29, 1302–1306,2006.

[35] A. Rowe, A. Tura, Experimental investigation of a three-material layered active magnetic regenerator, Int. J. Refrig. 29,1286–1293,2006.

[36] S. Jacobs, J. Auringer, A. Boeder, J. Chell, L. Komorowski, J. Leonard, S. Russek, C. Zimm, The performance of a large-scale rotary magnetic refrigerator, Int. J. Refrig. 37,84–91,2014.

[37] C.R.H. Bahl, K. Navickaitė, H. Neves Bez, T. Lei, K. Engelbrecht, R. Bjørk, K. Li, Z. Li, J. Shen, W. Dai, J. Jia, Y. Wu, Y. Long, F. Hu, B. Shen, Operational test of bonded magnetocaloric plates, Int. J. Refrig. 76, 245–251, 2017.

[38] Bez, H. Neves, K. Navickaitė, T. Lei, K. Engelbrecht, A. Barcza, C.R.H. Bahl, Epoxy-bonded $La(Fe,Mn,Si)_{13}H_z$ as a multi layered active magnetic regenerator, 2016.doi:10.18462/iir.thermag.2016.0147.

[39] V. Pecharsky, K. Gschneidner, A. Pecharsky, A. Tishin, Thermodynamics of the magnetocaloric effect, Physical Review B, 64(14), 144406/1-13, 2001.

[40] L. Tocado, E. Palacios, and R. Burriel, Adiabatic measurement of the giant magnetocaloric effect in mnas, Journal of Thermal Analysis and Calorimetry, 84(1), 213-217, 2006.

[41] E. Palacios, G.F. Wang, R. Burriel, V. Provenzano, R.D. Shull, Direct measurement of the magnetocaloric effect in $Gd_5Si_2Ge_{1.9}Ga_{0.1}$, Journal of Physics: Conference Series, 200(9),092011, 2010.

[42] R. Teyber, P. Trevizoli, T. V. Christiaanse, P. Govindappa, I. Niknia, and A. Rowe, Semi-analytic AMR element model, Applied Thermal Engineering,128,1022-1029, 2018.

[43] K. Engelbrecht, C.R. H. Bahl, and K. K. Nielsen, Experimental results for a magnetic refrigerator using three different types of magnetocaloric material regenerators, International Journal of Refrigeration, 30(4), 1132-1140,2011.

[44] T. Lei, K.K. Nielsen, K. Engelbrecht, C.R.H. Bahl, H.N. Bez, C.T.Veje, Sensitivity study of multi-layer active magnetic regenerators using first order magnetocaloric material $La(Fe,Mn,Si)_{13}H_{y}$, J. Appl. Phys. 118 014903, 2015.

[45] J. Tusek, A. Kitanovsky, S. Zupan, I. Prebil, A. Poredos, A comprehensive experimental analysis of gadolinium active magnetic regenerators, Appl. Therm. Eng. 53,57-66,2013.

[46] C. Aprea, A. Greco, A. Maiorino, C. Masselli, The energy performances of a rotary permanent magnet magnetic refrigerator, Int. J. Refrig. 61,1-11,2016.

[47] R. Teyber, P. V. Trevizoli, T. V. Christiaanse, P. Govindappa, I. Niknia, A. Rowe, Performance evaluation of two-layer active magnetic regenerators with second-order magnetocaloric materials, Appl. Therm. Eng. 106,405-414,2016.

[48] K.A. Gschineidner Jr., V.K. Pecharsky, Magnetocaloric materials, Ann. Rev. Mater. Sci. 30,387-429,2000.

[49] N.H. Dung, Z.Q. Ou, L. Caron, L. Zhang, D.T.C. Thanh, G.A. de Wijs, R.A. de Groot, K.H.J. Buschow, E. Brück., Mixed magnetism for refrigeration and energy conversion, Adv. Energy Mater. 1,1215-1219,2011.

[50] B. Yu, M. Liu, P.W. Egolf, A. Kitanovski, A review of magnetic refrigerator and heat pump prototypes built before the year 2010, Int. J. Refrig. 13,1029–1066,2010.

[51] J.W. Cable, E.O. Wollan, Neutron diffraction study of the magnetic behavior of Gadolinium, Phys. Rev. 165 733, 1968.

[52] S.Y. Dan'kov, A.M. Tishin, V.K. Pecharsky, K.A. Gschneidner Jr, Magnetic phase transitions and the magnetothermal properties of gadolinium, Phys. Rev. B 57 3478, 1998.

[53] J. Lyubina, Recent advances in the microstructure design of materials for near room temperature magnetic cooling, J. Appl. Phys. 109 07A902, 2011.

[54] S.M. Benford, G.V.Brown, T-S diagram for Gadolinium near the Curie temperature, J.Appl.Phys, Vol.52, No 3, 2110-2112, 1981.

[55] S.V. Taskaev, V.D. Buchelnikov, A.P. Pellenen, M.D. Kuz'min, K.P. Skokov, D.Y. Karpenkov, D.S. Bataev, O. Gutfleisch, Influence of thermal treatment on magnetocaloric properties of Gd cold rolled ribbons, J. Appl. Phys. 113 17A933, 2013.

[56] S. Fujieda, Y. Hasegawa, A. Fujita, and K. Fukamichi, Thermal transport properties of magnetic refrigerants $La(Fe_xSi_{1-}x)_{13}$ and their hydrides, $Gd_5Si_2Ge_2$ and MnAs, Journal of Applied Physics 95, 2429,2004.

[57] E. Brück, O. Tegus, L. Zhang, X. W. Li, F. R. de Boer, and K. H. J. Buschow, Magnetic refrigeration near room temperature with Fe_2P-based compounds, J. Alloys Compd. 383(1–2), 32–36,2004.

[58] O. Tegus, E. Bruck, X.W. Li, L. Zhang, W. Dagula, F.R. de Boer, K.H.J. Buschow, Tuning of the magnetocaloric effect in MnFe(P,As) by substitution of elements, J. Magn. Magn. Mater. 272-279 (3), 2389-2390,2003.

[59] L. von moos, K.K. Nielsen, K. Engelbrecht, C.R.H Bahl, Experimental investigation of the effect of thermal hysteresis in first order material MnFe(P,As) applied in an AMR device, Int. J. Refrig. 37,303-306,2014.

[60] T.D. Brown, I. Karaman, P.J. Shamberger, Impact of cycle-hysteresis interaction on the performance of giant magnetocaloric effect refrigerants, Mater. Res. Express 3,074001,2016.

[61] K.A. Gschneidner, V.K. Pecharsky, A.O. Pecharsky, C.B Zimm, Recent developments in magnetic refrigeration, Rare Earths 98,vol 315–3, pp 69–76, 1999.

[62] A.O. Pecharsky, K.A. Gschneidner, V.K.Pecharsky, The gaint magnetocaloric effect of optimally prepared $Gd_5Si_2Ge_2$, J. Appl. Phys. 93,4722–4728,2003.

[63] K.A. Gschneidner, V.K. Pecharsky, E. Bruck, H.G.M. Duijn, E.M. Levin, Comment on direct measurement of the gaint adiabatic temperature change in $Gd_5Si_2Ge_2$, Phys. Rev. Lett. 85,4190,2000.

[64] A. Fujita, S. Fujieda, Y.Hasegawa and K. Fukamichi, "Itinerant-electron metamagnetic transition and large magnetocaloric effect in $La(Fe_xSi_{1-x})_{13}$ compounds and their hybrids, Phys. Rev. B. 67,104416,2003.

[65] H.Wada, and T.Asano, "Effect of heat treatment on gaint magneocaloric properties of $MnAs_{1-x}Sb_x$, J. Magn. Magn. Mater. 290,703–705,2005.

[66] H. Wada H, C. Funaba, T. Asano, M.Ilyn and A.M.Tishin, Recent progress of magnetocaloric effect of $MnAs_{1-x}Sb_x$, Sci. Tech. Froid C. R., 2005–4, 37–46, 2005.

[67] Y. Long, Z. Y. Zhang, D. Wen, G. H. Wu, R. C. Ye, Y. Q. Chang, F. R. Wan, Phase transition process and magnetocaloric effects in the Heusler alloys NiMnGa with concurrence of magnetic and structural phase transition, Journal Appl. Phys. 98,033515,2005.

[68] E. Bruck, M. Ilyn, A.M. Tishin, O.Tegus, Magnetocaloric effects in $MnFeP_{1-x}As_x$ based compounds, J. Magn. Magn. Mater. 290,8–13,2005.

[69] D. Asten, $MnFeP_{1-x}As_x$ material data, personal communication, 2014.

[70] François Guillou, Giacomo Porcari , Hargen Yibole , Niels van Dijk , Ekkes Brück, Taming the first-order transition in giant magnetocaloric materials, Adv. Mater. 26, pp.2671–2675 2014.

[71] E.Bruck, M.Ilyn, A.M.Tishin, O.Tegus, Magnetocaloric effects in $MnFeP_{1-x}As_x$ based compounds, J. Magn.Magn.Mater. pp.8290-291, 2005.

[72] N. H. Dung, Z. Q. Ou, L. Caron, L. Zhang, D. T. C. Thanh, G. A. De Wijs, R. A. De Groot, K. H. J. Buschow, E. Brück, Mixed magnetism for refrigeration and energy conversion, Adv. Energy Mater.1,1215,2011.

[73] D. T. Cam Thanh, E. Brück, N. T. Trung, J. C. P. Klaasse, K. H. J. Buschow, Z. Q. Ou, O. Tegus, L. Caron, Structure, magnetism, and magnetocaloric properties of $MnFeP_{1-x}Si_x$ compounds J. Appl. Phys.103, 07B318,2008.

[74] N. H. Dung, Moment Formation and Giant Magnetocaloric Effects in Hexagonal Mn-Fe-P-Si Compounds, Technical University of Delft, 2012.

[75] V. Provenzano, A. J. Shapiro, R. D. Shull, Reduction of hysteresis losses in the magnetic refrigerant Gd5Ge2Si2 by the addition of iron, Nature 429,853-857,2004.

[76] K. Engelbrecht, K. K. Nielsen, C. R. H. Bahl, C. P. Carroll, D. van Asten, Material properties and modeling characteristics for MnFeP1-xAsx materials for application in magnetic refrigeration, J. Appl. Phys. 113,173510,2013.

[77] W. Brey, G. Nellis, S. Klein, Thermodynamic modeling of magnetic hysteresis in amrr cycles, Int. J. Refrig. 47,85-97,2014.

[78] F. Guillou, H. Yibole, G. Porcari, L. Zhang, N. H. van Dijk, E. Bruck, Magnetocaloric effect, cyclability and coefficient of refrigerant performance in the MnFe(P,Si,B) system, J. Appl. Phys. 116,063903,2014.

[79] T. V. Christiaanse, O. Campbell, P. V. Trevizoli, S. Misra, D. van Asten, L. Zhang, P. Govindappa, I. Niknia, R. Teyber, A. Rowe, A concise approach for building the S-T

diagram for Mn-Fe-P-Si hysteretic magnetocaloric material, J. Phys. D: Appl. Phys, 50,365001,2017.

[80] V.Basso, G. Bertotti, M.Lobue, C. Sasso, Theortical approach to the magnetocaloric effect with hysteresis, J. Magn.Magn.Mater. 290-290(part 1), pp.654-657, 2005.

[81] V. Basso, C. P. Sasso, G. Bertotti, M. LoBue, Effect of material hysteresis in magnetic refrigeration cycles, Int. J. Refrig. 29,1358-1365,2006.

[82] A.Kitanonovski, P.Egolf, Application of magnetic refrigeration and its assessment, J. Magn. Magn.Mater, 321(7), 777-781, 2009.

[83] T. Lei, K. Engelbrecht, K. K. Nielsen et al., Study of multi-layer active magnetic regenerators using magnetocaloric materials with first and second order phase transition, J. Phys. D: Appl. Phys 49, 345001,2016.

[84] C. Aprea, A. Greco, A. Maiorino, A numerical analysis of an active magnetic regenerative refrigerant system with a multi-layer regenerator, Energy Convers. Manage. 52,97–107,2011.

[85] T. Burdyny, A. Rowe, Simplified modeling of active magnetic regenerators, Int. J. Refrig. 36,932–40,2013.

[86] C.M. Hsieh, Y.C. Su, C.H. Lee, P.H. Cheng, K.C. Leou, Modeling of graded active magnetic regenerator for room temperature, energy-efficient refrigeration, IEEE Trans. Magn. 50,1–4,2014.

[87] Z.C. Xu, G.X. Lin, J.C. Chen, A GdxHo1x-based composite and its performance characteristics in a regenerative Ericsson refrigeration cycle, J. Alloys Compd. 639,520–525,2015.

[88] Y. You, S. Yu, Y. Tian, X. Luo, S. Huang, A numerical study on the unsteady heat transfer in active regenerator with multi-layer refrigerants of rotary magnetic refrigerator near room temperature, Int. J. Refrig. 65,238–249, 2016.

[89] B. Monfared, B. Palm, Optimization of layered regenerator of a magnetic refrigeration device, Int. J. Refrig. 57,103–111, 2015.

[90] J. Cararo, J. Lozano, P. Trevizoli, R. Teyber, A. Rowe, J. Barbosa J, Optimization of Active Magnetic Regneerators with Two and Three Layeres of Gd and Gd-Alloys, 2016. doi.org/10.18462/iir. thermag.2016.0126.

[91] S. Jacobs,Modeling and optimal design of a multilayer active magnetic refrigeration system 3rd IIF-IIR Int. Conf. on Magnetic Refrigeration at Room Temperature (Iowa).,pp. 267–273,2009.

[92] M.S. Kamran, H. Ali, M. Farhan, Y.B. Tang, Y.G. Chen, H.S. Wang, Performance optimization of room temperature magnetic refrigerator with layered/ multi-material microchannel regenerators, Int. J. Refrig. 68,94–106,2016.

[93] G. Green, J. Chafe, J. Stevens, J. Humphrey, A Gadolinium terbium active regenerator, Advances in Cryogenic Engineering (Advances in Cryogenic Engineering vol 35) ed R W Fast (Berlin: Springer),pp. 1165–1174,1990.

[94] A. Rowe, A. Tura, J. Dikeos, R. Chahine, Near room temperature magnetic refrigeration, Proc. The Int. Green Energy Conf. (Ontario, Canada: Waterloo), 2005.

[95] T. Okamura, K. Yamada, N. Hirano, S. Nagaya, Performance of a room-temperature rotary magnetic refrigerator, Int. J. Refrig. 29,1327–1331,2006.

[96] A. Rowe, A. Tura, Active magnetic regenerator performance enhancement using passive magnetic materials, J. Magn. Magn. Mater. 320,1357–1363,2008.

[97] D. Arnold, A. Tura, A. Rowe, Experimental analysis of a two-material active magnetic regenerator, Int. J. Refrig. 34,178–191, 2011.

[98] A.T. Saito, T. Kobayashi, S. Kaji, J. Li, H. Nakagome, Environmentally friendly magnetic refrigeration technology using ferromagnetic Gd alloys, Int. J. Environ. Sci. Dev. 7,316–320,2016.

[99] C.R.H. Bahl, D. Velazquez, K.K. Nielsen, K. Engelbrecht, K.B Andersen, R. Bulatova, N. Pryds, High performance magnetocaloric perovskites for magnetic refrigeration, Appl. Phys. Lett. 100,121905,2012.

[100] Y. Chiba, O. Sari, A. Sma, C. Mahmed, P. Nikkola, Experimental study of a multilayer active magnetic regenerator refrigerator-demonstrator, Progress in Clean Energy vol 1, ed I Dincer et al (Berlin: Springer),pp. 225–233,2015.

[101] B. Pulko et al, Epoxy-bonded La–Fe–Co–Si magnetocaloric plates, J. Magn. Magn. Mater. 375,65–73,2015.

[102] K. Navickait, H.N. Bez, T. Lei, A. Barcza, H. Vieyra, C.R.H. Bahl, K. Engelbrecht, Experimental and numerical comparison of multi-layered la(fe, si, mn)13Hy active magnetic regenerators, Int. J. Refrig. 86,322–330,2018.

[103] M. Balli, O. Sari, L. Zamni, C. Mahmed, J. Forchelet,Implementation of La(Fe, Co)13-xSix materials in magnetic refrigerators: practical aspects, Mater. Sci. Eng. B 177,629–634, 2012.

[104] J. Cheng, G. Liu, J. Huang, C. Liu, P. Jin, H. Yan, Refrigeration effect of $La(FeCoSi)_{13}B_{0.25}$ compounds and gadolinium metal in reciprocating magnetic refrigerator, J. Rare Earths 31,1163–1167,2013.

[105] N. Hirano, Y. Miyazaki, S. Bae, H. Takata, T. Kawanami, F. Xiao, T. Okamura, H. Wada, Development of room temperature magnetic heat pump technologies as a national project, in Japan. 6th IIF-IIR Int. Conf. on Magnetic Refrigeration, 6th Int. Conf. on Magnetic Refrigeration Proc.2014.

[106] U. Legait, F. Guillou, A. Kedous -Lebouc, V. Hardy, M. Almanza, An experimental comparison of four magnetocaloric regenerators using three different materials, Int. J. Refrig. 37,147–155,2014.

[107] I. Niknia, O. Campbell, T.V. Christiaanse, P. Govindappa, R. Teyber, P.V. Trevizoli, A. Rowe, Impacts of configuration losses on active magnetic regenerator device performance, Appl. Thermal Eng. 106,601-612,2016.

[108] M. Kaviany, Principles of Heat Transfer in Porous Media, 2nd Edition, Springer, 1995.

[109] K. K. Nielsen, J. Tusek, K. Engelbrecht, S. Schopfer, A. Kitanovski, C. R. H. Bahl, A. Smith, N. Pryds, A. Poredos, Review on numerical modeling of active magnetic regenerators for room temperature applications, Int. J. Refrig. 34,603-616,2011.

[110] K. Engelbrecht, A numerical model of an active magnetic regenerator refrigerator with experimental validation, Ph.D. thesis, University of Winsconsin-Madison , 2008.

[111] P. V. Trevizoli, A. T. Nakashima, J. R. Barbosa Jr., Performance evaluation of an active magnetic regenerator for cooling applications – Part II: Mathematical modeling and thermal losses, Int. J. Refrig. 72,206-217,2016.

[112] I. F. MacDonald, M. S. El-Sayed, K. Mow, F. A. Dullien, Flow through porous media Ergun equation revisited, Ind. Eng. Chem. Fund. 18,199-208,1979.

[113] D. L. Koch, J. F. Brady, Dispersion in fixed beds, J. Fluid Mech. 154, 399-427,1985.

[114] G. R. Hadley, Thermal conductivity of packed metal powder, Int. J. Heat Mass Tran. 29 ,909-920,1986.

[115] N. Wakao, S. Kaguei, Heat and mass transfer in packed beds, Gordon and Breach Science, New York, 1982.

[116] A. Morrish, The Physical Principles of Magnetism, John Wiley & Sons, Inc., 1965.

[117] A. R. Dinesen, Magnetocaloric and magnetoresistive properties of $La_{0.67}Ca_{0.33-x}Sr_xMnO_3$, Ph.D. thesis, Technical University of Denmark, 2004.

[118] P. V. Trevizoli, J. R. Barbosa, Jr., A. Tura, D. Arnold, A. Rowe, Modeling of thermo-magnetic phenomena in active magnetocaloric regenerators, J. Therm. Sci. Eng. Appl. 6 031016,2014.

[119] P. V. Trevizoli, J. A. Lozano, G. F. Peixer, J. R. Barbosa, Jr., Design of nested Halbach cylinder arrays for magnetic refrigeration applications, J. Magn. Magn. Mater. 395,109-122,2015.

[120] K. K. Nielsen, A. Smith, C. R. H. Bahl, L. Olsen, The influence of demagnetizing effects on the performance of active magnetic regenerators, J. Appl. Phys. 112,094905,2012.

[121] P. V. Trevizoli, J. R. Barbosa, Jr., P. A. de Oliveira, F. C. Canesin, R. T. S. Ferreira, Assessment of demagnetization phenomena in the performance of an active magnetic regenerator, Int. J. Refrig. 35,1043-1054,2012.

[122] T. Burdyny, A. Ruebsaat-Trott, A. Rowe, Performance modelling of AMR refrigerators, Int. J. Refrig. 37,51-62,2014.

[123] I. Niknia, P. V. Trevizioli, T. V. Christianse, P. Govindappa, R. Teyber, A. Rowe, Multiple points of equilibrium for active magnetic regenerators using first order material, J. Appl. Phys,123,204901-907,2018.

[124] I. Niknia, P. V. Trevizioli, T. V. Christianse, P. Govindappa, R. Teyber, A. Rowe, Material screening metrics and optimal performance of an active magnetic regenerator, J. Appl. Phys. 121,064902,2017.

[125] A.M. Tishin, Y.I, Shpichkin, The magnetocaloric effect and its application, Ins. Phy. Publ., Bristol, 2003.

[126] K. K. Nielsen and K. Engelbrecht, The influence of the solid thermal conductivity on active magnetic regenerators. J. Phys. D: Appl. Phys 45,145001, 2012.

[127] P.V. Trevizoli, G.F. Peixer, J.R. Barbosa Jr., Thermal-hydraulic evaluation of oscillating-flow regenerators using water: experimental analysis of packed beds of spheres, Int. J. Heat and Mass Transfer 99,918-930,2016.

[128] L. von Moss, C. R. H. Bahl, K. K. Nielsen, K. Engelbrecht, The influence of hysteresis on the determination of the magnetocaloric effect in $gd_5si_2ge_2$, J. Appl. Phys. 48,025005,2015.

[129] P. Govindappa, P. V. Trevizioli, I. Niknia, T. V. Christianse, , R. Teyber, A. Rowe, Multiple points of equilibrium for active magnetic regenerators using first order material, review, J. Appl. Phys.

[130] P. Govindappa , P. V. Trevizol , O. Campbell, I. Niknia, T. V. Christiaanse, R. Teyber, S. Misra, M A Schwind,D. van Asten, L. Zhang, A. Rowe, Experimental investigation of $MnFeP_{1-x}As_x$ multilayer active magnetic regenerators, J. Phys. D: Appl. Phys, 50,315001,2017.